DIGITALCOMMONS
@WAYNESTATE

Wayne State University

Wayne State University Theses

1-1-2015

Methodology For Performing Whole Body Pmhs Underbody Blast Impact Testing, And The Corresponding Response Of The Hybrid Iii Dummy And The Finite Element Dummy Model Under Similar Loading Condition

Karthik Somasundaram
Wayne State University,

Follow this and additional works at: https://digitalcommons.wayne.edu/oa_theses

Part of the Biomechanics Commons

Recommended Citation
Somasundaram, Karthik, "Methodology For Performing Whole Body Pmhs Underbody Blast Impact Testing, And The Corresponding Response Of The Hybrid Iii Dummy And The Finite Element Dummy Model Under Similar Loading Condition" (2015). *Wayne State University Theses*. 535.
https://digitalcommons.wayne.edu/oa_theses/535

This Open Access Thesis is brought to you for free and open access by DigitalCommons@WayneState. It has been accepted for inclusion in Wayne State University Theses by an authorized administrator of DigitalCommons@WayneState.

Methodology for Performing Whole Body PMHS Underbody Blast Impact Testing, and the Corresponding Response of the Hybrid III Dummy and the Finite Element Dummy Model under similar Loading Condition

By

Karthik Somasudaram

THESIS

Submitted to the Graduate School

Of Wayne State University,

Detroit, Michigan

In partial fulfillment of the requirements

For the degree of

MASTER OF SCIENCE

2016

MAJOR: BIOMEDICAL ENGINEERING
(Impact Biomechanics)

Approved By:

____

Advisor Date

©COPYRIGHT BY

KARTHIK SOMASUNDARAM

2016

All Rights Reserved

ACKNOWLEDGEMENTS

This study was funded by contract #N00024-13-D-6400, U.S. Army Research, Development and Engineering Command. Additional support was awarded by DOD, Army Research Office, National Defense Science and Engineering Graduate (NDSEG) Fellowship, 32 CFE 168a and Supporting Universities.

I would like to take this opportunity to thank all those people who have made an immense contribution towards the completion of my master's thesis at Wayne State University.

I feel fortunate and thankful to have Dr.Cavanaugh as my advisor, for his valuable support, guidance and time throughout my thesis and research work. Moreover, his endless patience and encouragement have propelled towards accomplishing my thesis. I am grateful to Dr. Cavanaugh to show confidence in me and giving me the opportunity to conduct a collaborative study with other laboratories.

I would also like to thank my committee members, Dr. Paul Begeman and Dr. Albert King, for providing their valuable motivation and direction towards completion of my thesis.

Further, I would like to express my sincere gratitude towards Mr. Don Sherman and Mr. Jason Greb for their guidance and the Sport & Ballistics group of the Biomedical Engineering Department at Wayne State University for assisting me in research work. I extend my gratitude to the Advance Human Modeling lab, especially to Mr. Anil Kalra, who helped me to understand the FEM concept and assisted me in running simulations.

Further Dr. Feng Zhu's expertise in FEA was essential to the completion of the simulation studies. I appreciate Dr. Cavanaugh's spine laboratory group for their timely assistance in this research and thesis completion work. I am very grateful to Dr. Srinivasu Kallakuri for motivating and encouraging me throughout my graduate study at Wayne State University.

I appreciate the effort put by Darlene Pennington-Johnson and Loretta Ann Sabo, Office of Research Compliance, for providing the necessary permission and license from the State Department to work with the sensor in this project. Special thanks go to radiologist Dr.Kochkodan for examining CT scan data, Dr.Schmidt for conducting autopsy evaluations, and the orthopedic residenct for assisting with the spine instrumentation.

Last I express my thanks to family members, my Mom, Dad, grandfather and all of my friends, for their unconditional love and support during the duration of my master's thesis.

TABLE OF CONTENTS

LIST OF FIGURES

LIST OF TABLES

CHAPTER 1

INTRODUCTION

Since World War I, the use of tanks as well as armored and infantry vehicles have increased. They better protect the occupants from enemies' fire and provide feasibility to maneuver through rough terrain. Possley et al. (2012) analyzed the probability of injuries sustained by mounted and dismounted soldiers during the Iraq war (2001-2009). The authors selected 1,890 spinal trauma causalities for their investigation. They reported that 26% of mounted soldiers sustained spinal fractures whereas; the remaining injuries were contributed by dismounted soldiers. This indicates that a maneuver with an infantry vehicle in a live theater is safer compared to foot movement. The efficiency of the tank was improved by adding armor and advanced weapons. As a tactical measure, improvised explosive devices (IED), anti-tank (AT) and anti-vehicular (AV) landmine weapons were developed. These mines and IEDs are usually buried in a vehicle's pathway and are detonated by sensing the vibration or the mass of the vehicle (Schneck, 1998). The explosion of the improvised explosive (IED) device has been reported to damage the integrity of the vehicle. IED detonation has contributed to significant loss to the military, both in terms of cost and human resources (Bird, 2001; Owens et al., 2007; Wang et al., 2001; Zouris et al., 2006). Bird (2001) reported that the percentage loss increased from 22% in World War II to 60% in the Somalia war. IEDs/landmines, the future warfare weapon produces severe damage to both the vehicle and its occupants. Radonic et al. point out in their article that mines exploded ¼ of the German tanks during the Russian-German war (Radonic et al., 2004). The advancement of armor used in infantry vehicles has led to the development of more lethal IEDs. These modernized weapons designed to maximize the energy along the occupant -Z axis is directed from toe to head (2014 SAE standard). Therefore, the vehicle becomes immobilized leading the detonation energy to concentrate along the Z axis (Mckay, 2010; Schneck, 1998). IED blast energy disintegrates the structure of the vehicle and is capable of producing high vertical acceleration. In the Rhodesian war (1972-1980) about 1409 vehicles were detonated by landmines, resulting in 632 deaths and 4410 injuries (Bird, 2001). Alvarez reported that of the 608 live theater causalities, 456 were caused by wound in action, while the remaining was due to killed in action (Alvarez, 2011). The author adds to say that in both sets fractures caused the most casualties, accounting for 53% compared to the causalities due to internal organ and concussion injuries. The US military is more concerned about the safety of the occupant than for the structural integrity of the vehicle. Hence, they are working closely with vehicle designer to device some strategies to mitigate these injuries. IED detonations under the vehicle produce two vertical impulses, one at the feet and another at the buttocks of the occupant. Several lower extremity UBB impact studies have been performed in recent years (Bir et al., 2008; Mckay, 2010; Schueler et al., 1995; Van der Horst et al., 2005). These experiments and live fire studies have provided a better understanding about lower leg injury mechanisms. Further biomechanical study is required to understand the mechanism of injury and tolerance to skeletal structure exposed to UBB. Next, during a UBB event along with seat acceleration, the load from the tibia is predicted to transfer to the lower vertebral column. Hence, the spine and the pelvis are more vulnerable to this kind of impact. Automotive crashes have never yielded such a complex injury pattern; however, free fall trauma, parachute jumping and pilot seat ejection events give some insight into understanding IED associated vertical deceleration injury mechanism. The peak acceleration of a pilot seat ejection event's falls in the range of 140 to 160 m/s^2 (Miller and Morelli, 1993). A helicopter vertical load generates peak acceleration in the range of 320 to 400 m/s^2 (Jackson et al., 2004) whereas the peak acceleration in a UBB blast is determined to be

980m/s^2 (Wang et al., 2001). Unlike the events mentioned above, a UBB impact produces high kinetic energy over a couple of milliseconds predominately along the principal Z axis, making it unique in producing complex vertical deceleration injuries.

1.1 Aim of the study

The current study provides a detailed overview of the methodology for performing underbody blast impact testing in a laboratory environment. In addition, Hybrid III dummy response to vertical loading conditions caused by UBB impacts was investigated. Furthermore, Livermore Software Technology Corporation (LSTC) finite element model was updated and then validated against the Hybrid III test data. The following are the specific areas this study seeks to clarify.

- A brief overview of orthopedic injuries due to an underbody blast (UBB) event
- Literature review of the lower spine and pelvis injuries among soldiers in modern warfare subjected to IED detonation as well as a brief summary of UBB associated orthopedic injury conducted under laboratory set up
- An overview of the spine and pelvis anatomy and bone mineral density measurement
- A detailed description of the cadaver testing methodology and data processing techniques implemented for simulated underbody blast impact test in the WIAMan project at Wayne State University.
- A report on the mechanical responses and the injuries produced from two postmoterm human surrogate (PMHS) tests for 4 m/s; 10 ms at the seat and 6 m/s; 5 ms at the floor.

- Develop and validate a finite element Hybrid III dummy in response to two simulated vertical loading conditions.

1.2 Epidemiology of blast-related skeletal injuries

The statistical analysis of soldier casualties reports that IED explosions, suicides, and roadside bombings have accounted for 60% loss of human life in Iraq and 50% in Afghanistan (Wilson, 2006). Landmine and IED explosions contribute to these losses and becoming a threat to military operations as well as human life. Different warfare statistics shown in Figure 1-1 highlight the percentage of USA military loss due to landmines in past combat operations (Bird, 2001). Owens et al. (2007) in their paper presented statistics about the contribution of modern warfare weapons to injuries during operations in Iraq (Operation Iraqi Freedom) and Afghanistan (Operation Enduring Freedom). The representative data are presented in bar chart format as shown in Figure 1-2. It can be inferred from the graph that IEDs alone contributed 36% of extremity injuries, while gunshots and grenades had accounted for 16% each.

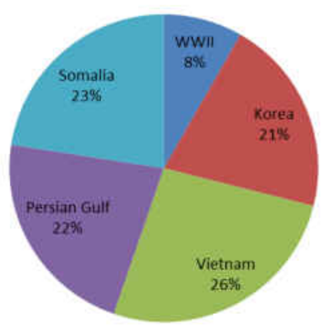

Figure 1-1: Pie chart highlights the percentage of USA military loss due to landmine explosions in past warfare (Bird, 2001).

In addition to traumas to extremities, soft tissue injuries were reported among casualties. The soft tissue injuries related to IED explosions accounted for 53%, while associated fracture was 26%.

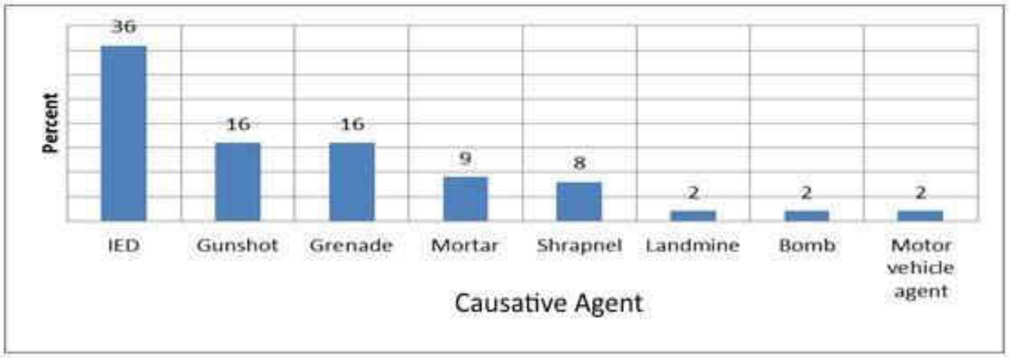

Figure 1-2: Contribution of different causative agents towards extremities injuries caused during OIF & OEF (Owens et al., 2007).

Zouris et al.(2006) in their paper on combat casualties reported that landmines were the main causative agent for extremity injuries in Operation Iraqi Freedom (OIF). The authors considered 279 US Marines and soldier personnel deployed in the field for their study. Of the total reported casualties, landmines alone produced 79% of the injuries to the lower extremities whereas IEDs mainly contributed to upper extremity trauma, accounting for 36%. Table 1-1 presents a brief overview of the contribution of modern weapon's to different orthopedic injuries. Therefore, it could be concluded that lower extremities are vulnerable to landmine explosion and upper extremities to IED explosive. The injuries sustained by the soldiers due to the landmines and IED explosions prevented them from performing an immediate action (Mckay, 2010).

Table 1-1: Injury location for wounded personnel due to different causative agents during OIF-I (Zouris et al., 2006).

Region (%)	IED	Landmine	Mortar	RPG	Shrapnel	Small Arms	Total
Back	0	0	3.3	2.5	1.7	1.2	1.5
Lower extremities	28.2	78.8	33.3	25.9	29.3	31.7	34.4
Upper extremities	35.9	12.1	36.7	33.3	27.6	42.7	33.1
Pelvis	2.6	0	6.7	2.5	1.7	2.4	2.5
others	33.3	9.1	20	35.8	39.7	22	28.5
Total	100	100	100	100	100	100	100

Other than injuries to the extremities, the spine is the second most vulnerable body region to experience high blast load under vertical loading. Schoenfeld et al. (2012) published a detailed review of combat-related spine injuries observed in 20th century Korean, Vietnam, and Gulf wars. The spine trauma accounted for only 1% of total combat causalities (Schoenfeld et al., 2012b). With the increase in the use of IEDs in recent wars, the probability of spine injuries has increased. The compressive load for the tibia was found to be much higher compared to the load experienced by the spine and the neck region (TR-HFM-090, 2007), shown in Figure 1-3. Next, the lumbar spine is reported to experience compressive vertical thrust of 4-5 kN.

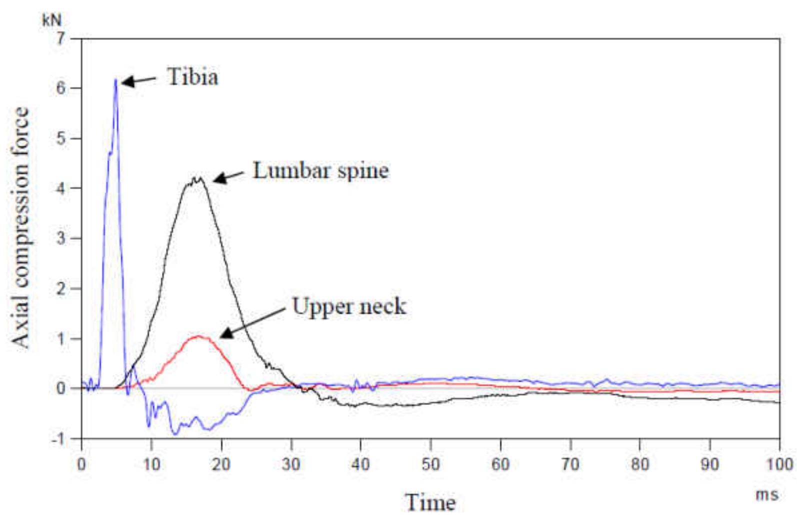

Figure 1-3: Axial compressive force measured in the tibia, lumbar spine and upper neck for a vertical load caused by underbelly blast impact (TR-HFM-090, 2007).

In addition, to the vertical thrust through the seat pan, a considerable magnitude of mechanical load is transferred to the pelvis and the torso from the lower extremities due to floor intrusion. Figure 1-4 shows the +Gz vertical load transmission pathway through the body. Even though the lower extremities receive maximum compression force, the severity of the injury is high in the pelvis and the lower spine regions. The pelvis is home to many vital organs. The intervertebral and the sacroiliac joints are one of the most complex articulations of the body. Unlike the lower extremity bones, the pelvic innominate bones lacks soft tissue covering; hence, the lower spine receives a major portion of the seat load through the pelvic girdle. The complex morphology of the lumbar spine and the pelvis make this region of the body more vulnerable to UBB kinds of impact.

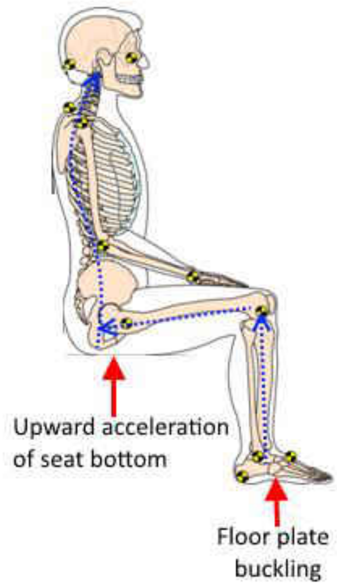

Figure 1-4: Pictorial representation of the load transmission paths subjected to vertical load under a UBB event (Ramasamy et al., 2009).

Comstock et al. (2011) in their investigation of Canadian warfare injury data states that the thoracolumbar spine region is more prone to field related spinal injuries. With reference to combat associated spinal trauma database, the authors reported that IEDs alone contributed about 57% of combat-related injuries followed by non-IEDs (23%) and blunt trauma related injuries (20%) in the live theater. Moreover, out of 372 injured soldiers from the Afghanistan war, 8% sustained at least one spine fracture. Further, 22 of 29 sustained a spinal injury due to an IED explosion. Among this spinal trauma, seven of them sustained stable fractures, nine unstable fractures, and six cases were unknown. Lumbar fracture was the most common battlefield spine injury.

In another study, Ragel et al. (2009) reviewed the spinal injuries of the soldiers deployed in the Afghan war. They reported that among the spinal injuries sustained by mounted soldiers due to IED explosions, 38% of the fractures were noted in the thoracolumbar region alone. In addition, three soldiers sustained multiple vertebral injuries which included chance and burst fractures. These injuries were analyzed to occur when the spine, particularly the thoracolumbar region, undergoes hyperflexion compression. The authors pointed out that this behavior of the spine was found to be similar to the chance fracture mechanism sustained by fighter pilots during the ejection phase. The authors also mention that in an automotive accident the probability of chance and thoracolumbar fracture is less than 0.15% and 2.5%, respectively, while in UBB impact, the incidence of these fractures is 1.82% and 42% respectively.

Warfield-related pelvic trauma due to penetrating injury is fatal compared to blunt injuries. Bailey and Stinner et al. (2011) conducted an investigation on pelvic fracture and the related injuries sustained by soldiers, who either died from those wounds or were killed in action during operations in Iraq and Afghanistan. They selected 91 pelvis injury fatalities; of those 63 were mounted and 18 dismounted at the time of injury. Out of these total causalities, 66% of the injuries were grouped as penetrating injuries, whereas 34% were blunt injuries. Figure 1-5 shows that blast explosion is the major cause of pelvis fracture accounting for 74% of the total, whereas gunshot wounds and motor vehicle collisions were 15% and 4.5%, respectively (Bailey et al., 2011).

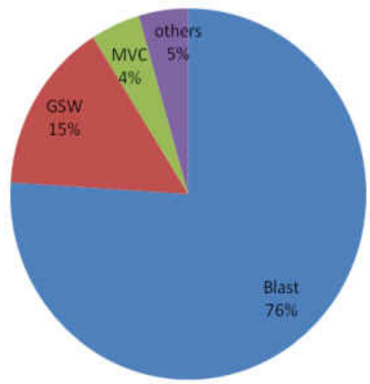

Figure 1-5: Pie chart of the percentage of pelvic injury caused by different weapons (Bailey et al., 2011).

Schoenfeld et al. (2012a) summarized the spinal injury sustained by soldiers deployed in Operation Iraq Freedom. They found that in the 15 month war, approximately 29 soldiers suffered from combat-related spinal trauma, accounting for 7.4% of the total combat casualties. Further, the blast mechanism produced 65% of the blunt trauma to the spine. 21% of those spine traumas were classified as closed fractures, whereas 7% were open fractures. Most of these combat-related spinal injuries were witnessed in the lumbar and cervical regions. The authors added that 7.4% of spinal trauma casualties in Operation Iraq Freedom (OIF) warfare were noted to be the highest in American warfare history, as shown in Figure 1-6. Other than load-bearing functionality, the lumbar region makes the upper torso flexible, bending forward, backward and sideward. Compare to the stiff thoracic spine, the lumbar spine is mobile, making the thoracolumbar junction more prone to fracture (Possley et al., 2012).

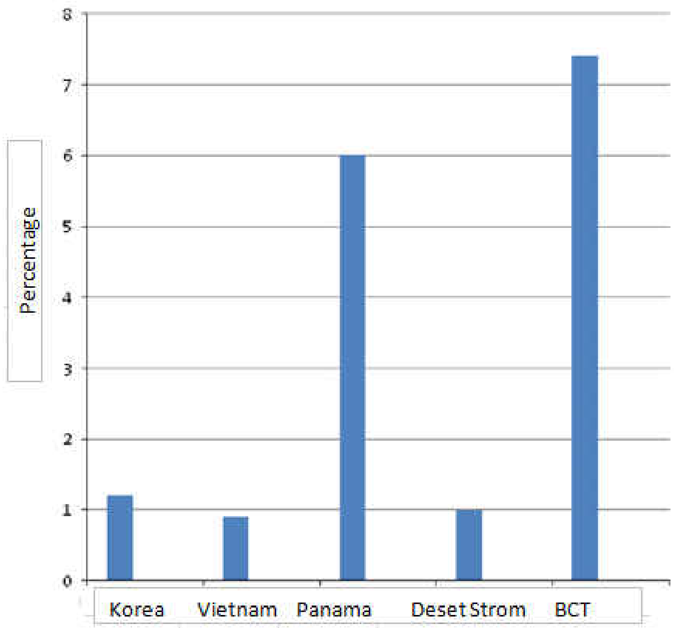

Figure 1-6: Bar chart of the percentage of spine trauma in warfare injuries. *BCT- Brigade combat team deployed in OIF (Schoenfeld et al., 2012a).

1.3 Positioning of the occupant

The orientation of the occupants in an armored vehicle differs based on the duties assigned to them. Most infantry vehicles consist of a driver, a commander, gunner, and passengers. Except for the gunner, all other occupants' feet rest directly on the floorboard and are in a seated posture. However, the gunner during a combat operation stands on an elevated platform; during a non-combat operation, he might sit on the seat. Based on the design of the vehicle, the seat arrangements of the occupants inside the vehicle differ in front or side facing. Also, the restraining and seat system differs from vehicle to vehicle. Figure 1-4 presents the flow of energy through the body during an underbody blast event. The orientation of the occupant during an impact plays a significant role in vertical load transfer through the body. However, for double site impacts such as those in UBB impact the high kinetic energy is transferred through both the feet and the buttocks. The pelvis tilt, the angle between the thigh and trunk, and the orientation of the sacrum with respect to the seat bottom are the primary parameters influencing the pattern of injury (Harrison et al., 1999). Schoberth and Hegemann (1962) examined the effect of the orientation of the pelvis on the body's center on gravity shift. The representative orientation of the pelvis and the corresponding shift in the center of gravity are tabulated in Table 1-2 and shown in Figure 1-7. The authors stated that for a normal sitting posture, the angle at the hip, knee and ankle joints is (90-90-90). The ischial tuberosity is the point of support for a normal sitting posture accompanied by the posterior pelvis tilt. They further reported that most people prefer to sit in a relaxed state by tilting the pelvis more posteriorly. In this position, the lumbar spine tends to be straight or slight in convex with respect to the seat back. Moreover, the center of gravity of body mass while sitting is noted to shift dorsally from ischial tuberosity to the ischial lesser arch with an increase in the posterior tilt. Another important sitting position parameter is the thigh-trunk angle, which also plays a significant role in producing injury to the occupant exposed to UBB impact. Keegan and Omaha, (1953) studied the effect of the thigh-trunk angle during pelvic tilt and corresponding lumbar spine curvature, as shown in Figure 1-8. They pointed out that with the decrease in the thigh-trunk angle, the pelvis tilts posteriorly accompanied by the kyphosis of the mobile lumbar spine. The posture with the torso-femur angle at 90 degrees represents the sitting position of the occupant in a vehicle. During an underbody blast event, the lower spine and upper leg flex towards each other, reducing the torso-femur angle. Reduction in the angle is accompanied by posterior pelvic tilt, leading to more stress on the thoracolumbar spine (KEEGAN and Omaha, 1953).

Table 1-2: The orientation of the pelvis, corresponding CG and body weight transferred with respect to sitting posture (Schoberth and Hegemann, 1962).

Sitting posture	Orientation of pelvis	Center of gravity location	Body weight transferred
Anterior (A, B)	• Forward rotation of the pelvis. • Flexing spine without much rotation of pelvis	In front of the ischial tuberosity	Feet transmit more than 25%
Middle (C)	• Neutral or normal position	Above ischial tuberosity	Feet transmit 25%
Posterior (D)	• Extension rotation of the pelvis. • Kyphosis of the spine	Above/behind ischial tuberosity	Feet transmit less than 25%

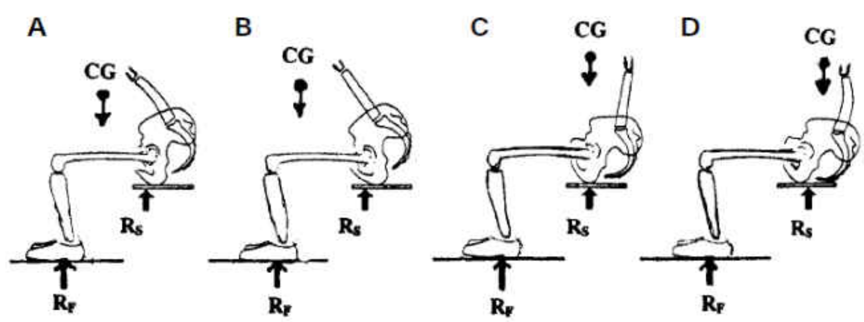

Figure 1-7: Shift in the body's center of gravity based on occupants sitting posture (Schoberth and Hegemann, 1962).

During an underbody blast, the occupant experiences two separate +Gz accelerations (Figure 1-4) (Ramasamy et al., 2009). The first input is at the feet of the occupant due to the intrusion of the floor-plate. The second input is at the occupant's buttocks due to the vehicle's upward acceleration. The feet acceleration precedes the seat acceleration by a few milliseconds. Sacral and pelvic injuries are mostly due to seat acceleration. This combination of short duration high-rate loading can results in complex injury patterns.

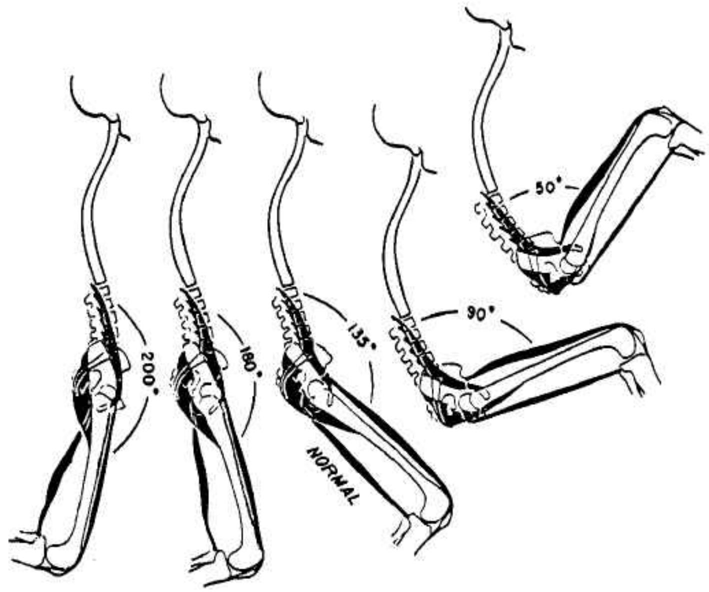

Figure 1-8: Effect of the thigh-torso angle on pelvic tilt (KEEGAN and Omaha, 1953).

CHAPTER 2

THEATER INJURY CASE STUDY AND BLAST BIOMECHANICS

The increased use of landmines/ IEDs by insurgents in Iraq and Afghanistan confirms that these are the signature weapon of the future battlefield (Owens et al., 2007; Ramasamy et al., 2009). Blast events due to landmine explosion have caused major losses to the US military in terms of both human and wealth resource. Injuries related to IED explosions are entirely different and mores server compared to other modern weaponry (Bailey et al., 2011; Owens et al., 2007; Zouris et al., 2006). Although the duration of mines/IED explosion events occurs in a few milliseconds, the kinetic energy generated by the detonation is significant enough to disintegrate the vehicle (Wang et al., 2001). Simultaneously, occupants of the vehicle experience severe orthopedic and soft tissue injuries. The injury mechanisms due to blast impact could well be understood by reviewing IED associated injury case studies of soldiers subjected to underbody blast impact and examining the basic concept of the physics behind the blast event.

1.4 Case study from literature

There are only a few live theater IED-associated spinal and pelvic trauma case studies in the literature. Soldiers returning with tertiary blast injuries from the recent battlefield are very complex to operate it back to normal state. No such injury pattern has ever been reported among the civilian population.

One such multiple and complex military trauma due to an IED was seen at Walter Reed Military Hospital. Kang et al. (2012a) illustrated a classic example of a comminuted Zone III sacral fracture along with a bilateral sacroiliac joint rupture and three transverse process fractures sustained by an on-duty soldier exposed to an IED explosion. Moreover, the solider also received associated injuries that included a bilateral trans-tibial amputation, a left acetabular fracture, multiple rib fractures and organ injuries.

In another case study witnessed at the same hospital reported that an active soldier exposed to similar environmental conditions sustained a stable Zone II fracture at S1/S2 (Cody et al., 2012). The associated injuries included a left L5 transverse process fracture and a facet fracture with L5/S1 retrolisthesis.

A similar IED induced trauma active solider was received at the University of Health Science, Maryland. He sustained L5 and L4 burst and compression fractures, respectively, along with a posterior ligament ruptures (Kang et al., 2012b). The associated injuries included trans-femoral amputation and facial fractures.

To understand the biomechanical response and the mechanism invovled in these live theater injuries, cadaver testing under a controlled environment has been performed. Bailey and Christopher et al. performed PMHS testing under a laboratory setup using a sled system (Bailey et al., 2013). They examined the pelvis and lower extremity mechanical response when exposed to UBB loading conditions. Five whole-body cadavers were subjected to impactor velocity ranging from 7.5m/s to 14m/s over a 3 millisecond interval. The corresponding pelvis and tibia threshold was measured to be 300g and 600 g respectively. The surrogates sustained a combination of pelvis, spine, and lower leg injuries. The authors also determined the Hybrid III dummy response under similar loading conditions. They found that both the loading rate and pelvis jerk to be higher in the dummy compared to cadaver testing. Further they reported the inexactitudes of the automotive dummies in replicating cadaver response under UBB conditions.

1.5 Effect of blast event on a vehicle and its occupant

Triggered IEDs and landmines irrespective of their state (liquid, solid or gaseous) undergo a quick chemical reaction, producing a pressurized gaseous product. This compressed gas expands rapidly in the surrounding area, and its volume increases to about 10^5 times the atmosphere volume. Therefore, gas molecules are accelerated, leading to the formation of a shock wave which then propagates at a velocity of 1,000 m/s (Stuhmiller et al., 1991). For Trinitrotoluene composed IEDs, detonation velocity was determined to be 7,000 m/s (Schardin, 1950). The resulting wave pattern disturbs the state of the surrounding gas molecules. In turn, temperature rises in the range of 2000 to 6000 C. The density and pressure of the blast wave produces a distorted region (Ramasamy et al., 2011). The static or shock wave followed by a rapid motion of gas molecules produces blast wind. Human or animal tissue exposed to or lying in this environment will yield serious blast injuries.

The complexity of the detonation waveform and the energy liberated from the explosion determines the intensity of the wound caused. Underbody blast events and IED/ landmine explosion procedures follow three major phases (Ramasamy et al., 2011). First, the blast wave produced due to the detonation interacts with the soil. Second, the highly compressed shock wave fractures the surface of the soil, liberating the gas molecules which further hit the base of the vehicle. The incident wave is reflected from the vehicle base toward the center of the explosive. Hence, the reflected wave multiplies with the incident wave, generating a highly compressed region between the soil surface and the base of the vehicle.

Third, these pressurized gas molecules and soil eject due to the gas expansion during detonation interact with the vehicle floor instigating local deformation and fracture of the floorboard. This ruptured base of the vehicle allows the pressurized shock wave to penetrate the occupant compartment resulting in injuries to the lower extremities in the first phase. In the second phase, the whole vehicle is accelerated vertically, producing injuries to the upper leg, pelvis, and spine.

Based on the landmine/IED explosion linked causality database from war in Iraq and Afghanistan, blast-related injuries are classified into four main categories: primary, secondary, tertiary and quaternary (Ramasamy et al., 2009). These will be explained below.

The initial shockwave after detonation rapidly increases the surrounding pressure. The injury produced under such an atmosphere is termed as a primary blast injury (Ramasamy et al., 2009). The blast wave does not accelerate the body. However, the sudden change in pressure causes serious injuries to hollow organs such as the GI tract and lungs. The primary blast wave is also observed to produce mild traumatic brain injury (mTBI) (Taber et al., 2006; Warden, 2006; Warden et al., 2009). The exact mechanism involved in mild TBI is yet to be investigated. The severity of the injury depends on the distance of the body from the explosive site and also the amount of explosive used for detonation (Kang et al., 2012c).

Secondary injuries occur due to the accelerated explosive or nearby compartment fragments. The pressurized detonation product transfers the energy and momentum to the vehicle body that in turns accelerates the debris. Based on the kinetic energy of the wreckage and its material property, injury severity varies. Lower extremity fractures are the most common trauma observed in secondary blast injuries.

Both the local and global effects resulting from the explosion yield tertiary injury. The highly pressurized shock wave and accelerated soil debris accelerate the vehicle. The accelerated occupant compartment causes the occupant to collide with the interior surface, and occupants thrown from the seat, resulting in significant injuries to the upper legs, pelvis, and spine (Ramasamy et al., 2009). Most of these injuries are related to the long bones and vertebral body fractures. Head and facial injuries are other common wounds seen in such an impact (DePalma et al., 2005; Xydakis et al., 2005). The magnitude of the explosive and the mass of the vehicle determines the vertical acceleration of the vehicle in the air (Kang et al., 2012c). After reaching a certain height, the vehicle drops down due to the action of gravity. The load due to gravity also acts upon the passenger in the vehicle. However, this load is insignificant compared to the vertical thrust (Mckay, 2010). Local deformation of the floorboard produces serious injuries and fracture to the lower extremities. Most UBB-associated trauma could be classified as tertiary blast injuries. Injuries due to thermal burns and the aftermath of detonation together constitute quaternary injuries.

CHAPTER 3

ANATOMY AND BONE MINERAL DENSITY

During the tertiary phase of an underbody blast event, the blast overpressure and the blast wind accelerate the vehicle and its passengers above the ground. Due to the intrusion of the floor plate, the lower extremity region such as the ankle bones, tibia, femur, and patella are loaded with the high vertical load. Followed by floor deformation, the seat is translated vertically upward resulting in pelvis and lower spine injuries. The increase in area/volume and the load carrying capacity of the lumbar vertebrae saves the superior spinal segments from injury under higher vertical acceleration (Yoganandan et al., 2013). To understand the orthopedic injury mechanism of different regions, the anatomy of the chief bones must be analyzed.

1.6 Spine

The vertebral column of a human, which lies medially to the posterior part of the trunk, is one of the most complex musculoskeletal structures. It runs all the way from the base of the skull to the pelvic girdle. Its primary function is to protect the spinal cord and support the head, neck, upper extremities and trunk. It also transfers the load from the trunk to the pelvis. There are in total 33 vertebrate: 7 cervical, 12 thoracic, 5 lumbar, 5 sacral, 4 coccyx. The first 24 are well defined and articulate with successive vertebrae, and the remaining 9 are fused to form the posterior frame of the pelvic girdle (Gray et al., 1973). This bony spinal column forms two curvatures, namely kyphotic (thoracic and sacral curve) and lordosis (cervical and lumbar), as shown in Figure 3-2. These curves help with balancing the body weight and walking. In addition, the 22 fibrocartilage discs between adjacent vertebrae form synovial joints, which allow the movement of the spine in all three anatomical planes and act as a shock absorber. No such disk is found between the skull and C1 or between C1 and C2. The vertebral disks along with the abdomen and back muscles stabilize the spinal column, while the anterior and posterior muscles of the spine provide the force required for the flexion and extension movements of the trunk, respectively (Moore et al., 2006). These muscles work in unison as well and provide the rotational ability to the spine. The vertebral column is the main channel for transferring the load from caudal to cranial and vice-versa (Gray et al., 1973). Therefore, the load experienced by the lower extremities, pelvic or head ultimately leads to an indirect impact on the vertebral column.

Thoracic and lumbar vertebral fractures are common, under a UBB-induced spinal trauma (Comstock et al., 2011; Possley et al., 2012; Ragel et al., 2009). The thoracic vertebrae make up the central part and occupy a larger portion of the spinal column (Netter, 2010). These vertebrae have long and almost horizontal spinous processes. Furthermore, the facet is more vertical and oriented in the coronal plane. Also, the body diameter increases from T1 to T12, with the T1 centrum resembling the cervical vertebrae body and T12 as L1, respectively. In high +Gz acceleration, T12 is prone to stress/ compression related injury. Of all the 33 vertebrae, the lumbar are the largest bones of the spine (Gray et al., 1973). In addition, these vertebraes have a flat superior, and inferior end plates, which make them to bear the load applied along the axis. Moreover, with the curved and vertical facets, the lumbar vertebrae have the ability to withstand the shear load. Unlike, the thoracic vertebrae, the lumbar do not have a prominent spinous process. The transverse and spinous processes of the lumbar vertebrae function like a lever, enhancing the function of the muscles attached to them (Bogduk, 2005). Figure 3-1 shows a pictorial image of lumbar and thoracic vertebral body.

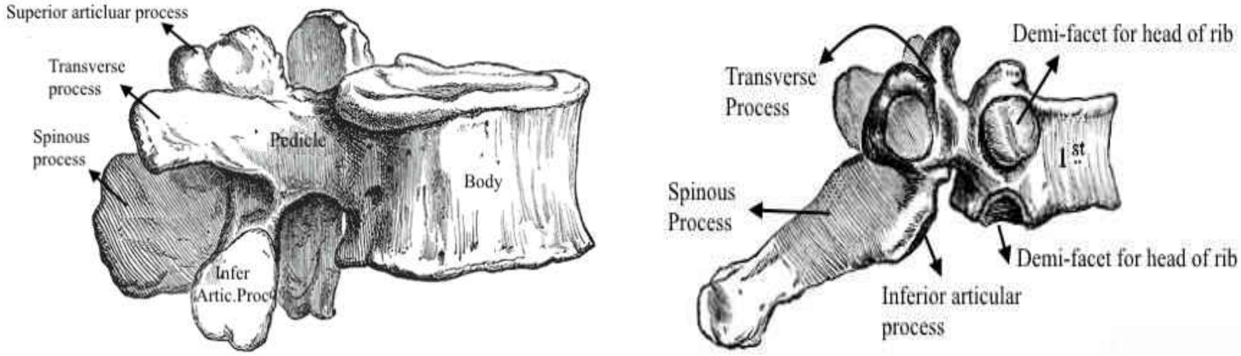

Figure 0-1: A pictorial comparison between the lumbar and thoracic vertebral bodies (Gray et al., 1973).

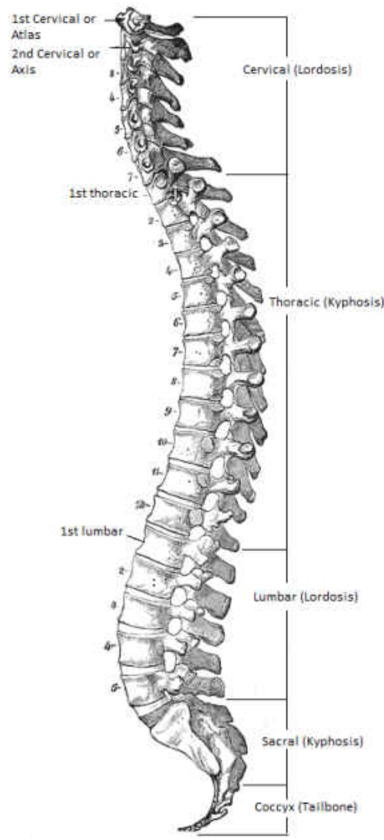

Figure 0-2: Anatomy of the Spine (Gray et al., 1973).

1.7 Pelvis

Each of the two innominate hemi-pelvis bones consist of three sub-bones: the ilium, ischium and pubis. Each fuses at the acetabulum, forming the anterior and lateral walls of the pelvic girdle whereas, the fused sacral and coccyx vertebrae form the posterior part of the girdle (Gray et al., 1973). The sacrum is a wedge between the hip bones which is attached to the ilium bone of the hip by interosseous ligament, forming the sacroiliac (SI) joint (Netter, 2010). This connection of the sacrum to the innominate bones along with the symphysis of the pubic bone provides a ring appearance to the pelvic girdle. The pelvic ring transmits the load from the vertebral column towards the lower extremities and vice versa (Moore et al., 2006). In addition, the upper body weight converges to the femoral neck through the sacroiliac joint. A high-energy impact such as UBB event disrupts the pelvic bone as well as abdominal organs. An anterior anatomical view of pelvic girdle is presented graphically in Figure 3-3.

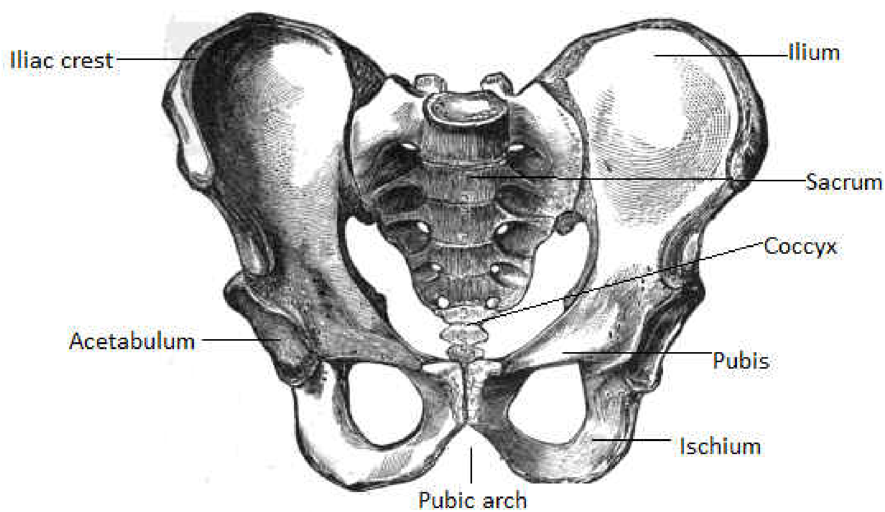

Figure 0-3: Anatomy of the Pelvis (Gray et al., 1973).

1.7.1 Sacrum

In a UBB scenario, mounted occupants experience two separate vertical accelerations. One is at the feet due to floor plate intrusion, and the other is at the pelvis due to seat pan acceleration. The sacrococcygeal segment of the spine comes in direct contact with seat pan. High +Gz seat acceleration contributes to severe pelvic and sacral fracture. The Sacrum articulates with the fifth lumbar vertebrae cranially whereas its apex articulates with the coccyx (Gray et al., 1973). In addition, it forms the sacroiliac joint with the hip bones, which are held together by a sacral-iliac ligament. Five fused curved sacral vertebrae project forward, resulting in the sacrovertebral angle with the last lumbar vertebrae (Netter, 2010). As the central region is curved and directed backward, this increases the capacity of the pelvic cavity. The size of the sacral vertebrae decreases from top to bottom. Each ridge shown in Figure 3-5 ends in a sacral foramina, through which the sacral nerve pass (Gray et al., 1973). These lateral foramina are a source of stress concentration, and a vertical fracture could result through these foramina.

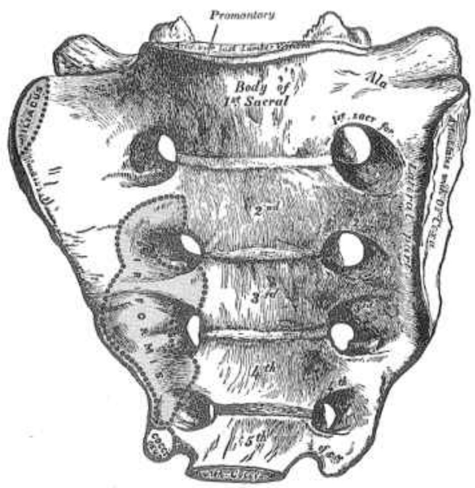

Figure 0-4: Sacrum frontal view (Gray et al., 1973).

Furthermore, the posterior surface of the sacrum is narrower and more convex then the anterior portion. It consists of incomplete spinous processes and laminae. Other than the SI ligament, sacrotuberous and sacrospinous ligaments play an essential role in locomotion and maintaining the stability of the pelvis (Moore et al., 2006). The sacrospinous ligament resists external rotation of the ischium, while the sacrotuberous ligament resists vertical loads by pushing the pelvis down with respect to the sacrum. This action of the ligament results in serious injuries to both the pelvis and sacrum during vertical seat pan acceleration, such as in an IED detonation. In UBB events, both vertical and transverse sacral fractures have been observed to be common among mounted soldier (Cody et al., 2012; Kang et al., 2012a).

1.8 Ligaments of spine and pelvis

The pelvis lacks soft tissue. Hence, it is deprived of inherent stability. The ligament and muscles of the spine and pelvis are essential parameters for pelvic stability. The pubic rami and symphysis joint together act as a strut and prevents the pelvis from collapsing anteriorly, while the SI complex provides the stability to the posterior structure (Gray et al., 1973). Analyzing the pelvic injury mechanism requires careful assessment of both the magnitude and direction of the load as well as the orientation of the pelvis at the time of impact. To some extent individual upper body mass plays an important role in defining the severity of the injury. The femoral neck receives the torso weight through the SI complex (Gray et al., 1973). Therefore, a larger body mass would destabilize the hip joint resulting in lower back and limb pain. Table 3-2 presents the ligaments involved in stabilizing pelvic structural integrity. Most of the connecting and pelvic floor ligaments work as one group to maintain pelvic ring structure stability. The posterior ligaments of the spine and the pelvis together form a tension band that resists the deforming forces (Tile et al., 2003), while the SI, iliolumbar and the sacrospinous ligament resist the transverse rotational force and the vertical ligaments running along the pelvis resist the shearing force in the longitudinal direction.

Table 0-1: A brief summary of pelvis-floor ligament anatomical location and physiological function. (These ligaments have been hypothesized to play a critical role in pelvis fracture mechanism under, a UBB type environment) (Gray et al., 1973; Tile et al., 2003).

Ligament	Anatomical location	Function
Iliolumbar (IL)	Transverse process of L5 to iliac crest	Strength the lumbar-sacral joint.
Interosseous Sacroiliac	lateral surface of the ilium to the lateral surface of the sacrum	Resist abduction of SI joint. Resist anterior displacement of the sacrum.
Anterior Sacroiliacs (ASI)	Anterior aspect of sacrum to ilium	Resist external rotation and shearing force
Posterior Sacroiliacs (PSI)	Posterior superior iliac spine (PSIS) to lateral surface of sacrum	tension band of pelvic ring and stabilize the posterior pelvis
Sacrospinous	Connects the lateral edge of the sacrum to ischial spine	Resist external rotation force
Sacrotuberous	Connects the sacrum to ischial tuberosity	Resist shearing rotary force.
Pubic Symphysis	Joins the lateral aspect pubic bone	Along the pubic rami, it acts as a strut and maintains the pelvis stability anteriorly.

1.9 Femur

The femur is the longest and strongest cylindrical bone in the body, shown in Figure 3-4. It joins as well as transfers the load from the pelvic girdle to the lower leg. The globular head articulates with the acetabulum to form a ball and socket joint (Huelke, 1986). In addition, a flat pyramidal portion of the bone termed as the femoral neck forms a 125 degree angle with the shaft. Furthermore, the shaft runs down to form medial and lateral condyles that articulate with the tibia condyle to form the knee joint. A large group of muscles called the quadriceps femora anchors to the lateral and anterior region of the femur (Netter, 2010). These muscles act as an extensor for the knee joint and stabilize the patella bone in position. This muscle is essential for walking, running and squatting.

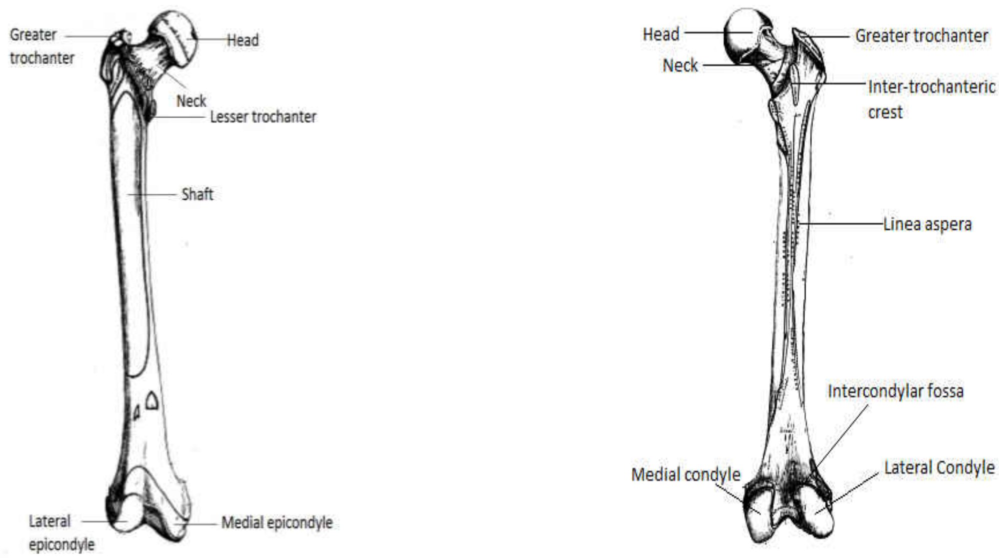

Figure 0-5: Anterior and posterior view of the femur (Gray et al., 1973).

1.10 Bone mineral density(BMD)

The severity of a fracture depends on both the amount of load experienced by the skeleton structure due to impact and the bone strength of the occupants involved (Melton et al., 1997). Although soldiers have good physique and undergo similar training, the bone mineral content of each differs. The BMD differs based on gender, age, race, and ethnicity. From beginning of the civil war the contribution of black Americans in the war field has been significant, as shown in Figure 3-6 (Segal and Segal, 2004). Later due to a large number of immigrants, people of different races and ethnicities came forward to join the US military. Table 3-2 shows active duty service officers based on their rank, race, and ethnicity. The authors state that all four US military branches consist of people from different backgrounds (Segal and Segal, 2004). Futher, the posting of these personnel is determined purely by their performance and skill and not on their race. The US military consists of one of the most diverse populations in the world (Segal and Segal, 2004).

Bone is made up of minerals, principally calcium hydroxyapatite, embedded in type 1 collagen and a specialized protein that makes up the bone matrix (Cummings et al., 2002). Mineral content is measured using bone densitometry. Calcium is capable of absorbing more radiation compared to other minerals. The higher the mineral content, the darker the image will be, indicating a larger amount of calcium content at the particular point of the bone.

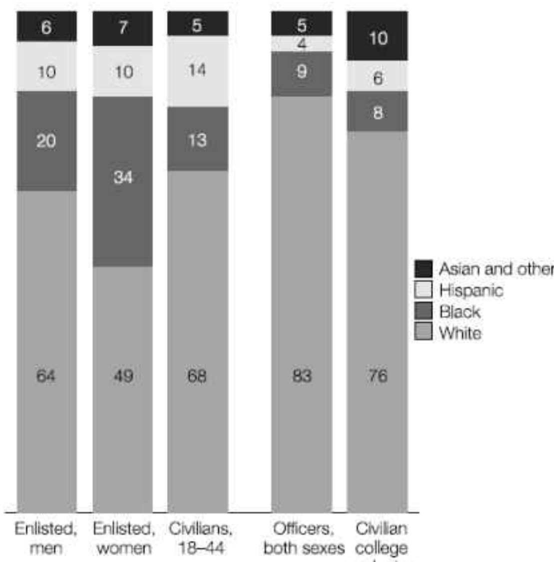

Figure 0-6: Active duty military and civilians by race and ethnicity, 2002 (Segal and Segal, 2004).

Table 0-2: Active –service duty officers by rank, service and race/ethnicity (Segal and Segal, 2004).

Rank	Army			Navy			Marines			Air Force		
	White	Black	Hispanic	White	Black	Hispanic	White	Black	Hispanic	White	Black	Hispanic
All the officers (%100)	100	100	100	100	100	100	100	100	100	100	100	100
Company grade	57	61	71	58	69	73	62	71	79	57	63	64
Field grade	42	39	29	42	30	27	37	29	20	43	37	36
General	1	--	--	--	--	--	--	--	--	--	--	--

Bone mineral density (BMD) is defined as the ratio of bone mineral content to the area of the bone that is being analyzed (Cummings et al., 2002). Clinical bone densitometry results are defined in terms of T-scores and Z-scores. The standard deviation (SD) obtained by comparing patients' densitometry with the BMD of young, healthy adults is termed as the T-score (NIH, 2012). In contrast, if the patient mineral content is compared to the BMD of the same age group, the obtained SD value is termed as the z-score. An SD below -2.0 indicates the BMD of the occupant is low compared to the general population. A Z-score measurement sometimes could be misleading since the SD value is predicted based on comparison with the same age group (NIH, 2012). Table 3-8 shows the World Health Organization's proposed T-scores and Z-scores.

Table 0-3: World Health Organization's definitions based on Bone Density Levels (T-score) (NIH, 2012).

According to World Health Organization	
Level	Definition
Normal	Bone density is within 1 SD (+1 or −1) of the young adult mean.
Low bone mass (osteopenia)	Bone density is between 1 and 2.5 SD below the young adult mean (−1 to −2.5 SD).
Osteoporosis	Bone density is 2.5 SD or more below the young adult mean (−2.5 SD or lower).
Severe (established) osteoporosis	Bone density is more than 2.5 SD below the young adult mean, and there have been one or more osteoporotic fractures.

Table 0-4: Osteoporosis attribution probability by fracture type, race/ethnicity and age (Melton et al., 1997).

		45-64 years		65-84 years		≥ 84 years	
	Site	Median attribution, probability (range)	Validity rank	Median attribution, probability (range)	Validity rank	Median attribution, probability (range)	Validity rank
White population	Hip	0.60 (0.10-0.70)	2.2	0.80(0.60-0.95)	1.8	0.85(0.80-0.95)	1.7
	Spine	0.70 (0.50-0.90)	2.2	0.90(0.50-0.95)	1.8	0.90(0.60-0.95)	1.8
	Forearm	0.40 (0.05-0.50)	2.5	0.45(0.15-0.60)	2.3	0.45(0.30-0.60)	2.2
	Other sites	0.15 (0.05-0.30)	2.7	0.30(0.20-0.40)	2.7	0.45(0.30-0.50)	2.7
Black population	Hip	0.30(0.05-0.65)	2.8	0.65(0.10-0.85)	2.3	0.75(0.25-0.90)	2.3
	Spine	0.55(0.30-0.40)	3	0.75(0.30-0.90)	2.5	0.85(0.30-0.95)	2.3
	Forearm	0.20(0.05-0.40)	2.7	0.30(0.10-0.50)	2.8	0.35(0.20-0.50)	2.8
	Other sites	0.15(0.05-0.20)	3.5	0.15(0.05-0.30)	3.5	0.25(0.15-0.40)	3.5
Other Race population	Hip	0.55(0.10-0.65)	3.2	0.75(0.15-0.90)	3	0.85(0.30-0.95)	3
	Spine	0.60(0.30-0.80)	3.2	0.75(0.40-0.90)	3	0.85(0.50-0.95)	3
	Forearm	0.30(0.30-0.55)	3	0.35(0.15-0.50)	3	0.40(0.30-0.50)	3
	Other sites	0.15(0.10-0.30)	3.3	0.20(0.10-0.40)	3.3	0.30(0.20-0.50)	3.3

The age, gender, race and ethnicity of the patient are essential for defining the bone mineral density of the occupant. Based on the standard deviation value the World Health Organization has defined a certain range for predicting the occurrence of osteoporosis and osteopenia, as presented in Table 3-4. It represents the variation in the standard deviation of different races and ethnicity groups that determines the probability for osteoporosis leading to bone fracture (Melton et al., 1997). Furthermore, the fracture rate is higher in Caucasian men than black men, whereas the other groups lie between these ranges. In addition, age is also an important parameter for determining the mineral content of bone. For example, consider a data from Table 3-4, the probability of hip bone fracture for 45 years old white man lies in the range of 0.10 to 0.70, while it increases to 0.60 to 0.95 for 65-year-old man of the same race. Moreover, when the same parameter was considered for black men of age 45, the chance of getting a hip fracture was noted to be low (0.05-0.65). Authors mentions that white and asian groups are prone to fracture since their bone mass is comparatively less dense than for black men (Melton et al., 1997). Therefore, based on race and ethnicity the reference value for determining a patient's T-score and Z-score will differ. Gender consideration is also an important parameter in determining bone mineral content. However, for an UBB event study, male gender is considered since most of the mounted soldiers in an army tank are male. Hence, the bone mineral density value for female the gender is not taken into consideration for this study. In an UBB impact, high loads are experienced by the bone leading to a fracture. Unlike the magnitude of the load and duration of the event, bone mineral density or bone strength plays a minimal role in understanding the injury and biomechanical response of the occupant. However, mineral density measurement is one of the important criteria in the specimen selection procedure. In the current study, it is used as a tool to reject a specimen with osteoporosis and osteopenia conditions prior to acquiring a body from a vendor. All the cadaveric BMD were measured using the Dual X-ray Absorptiometry technique.

CHAPTER 4

CADAVER TESTING AND DATA PROCESSING METHODS

UBB-associated casualties have recently increased due to the wars in Iraq and Afghanistan. Such complex injury patterns are rarely seen among civilians in car crashes. Researchers and the military are performing collaborative studies with armored vehicle manufacturers to mitigate these injuries (Bailey et al., 2015; Bosch et al., 2014; Kargus et al., 2008). However, automotive dummies have not yet been developed for evaluating occupant response subjected to vertical loading conditions. In addition, the currently available biomechanical response data are not suitable for designing a new biofidelic dummy. Therefore, to obtain the characteristic whole body response from UBB impact conditions, the military is funding cadaver testing under a controlled environment. Whole body post mortem human subject (PMHS) testing under laboratory conditions will provide a better understanding of the mechanical response of the body subjected to vertical load and will possibly explain combat-linked injuries due to IED/landmine explosions. Finally, the biomechanical response colliders developed from cadaver testing could be implemented in dummy design for future studies and live fire testing.

The current study thesis on investigating the biomechanical response and corresponding injuries sustained by the test subject for given UBB loading condition and also on the development of the methodology for this testing. Using the modified Wayne Horizontal Acceleration Mechanism (WHAM) III sled system, two whole body specimens were subjected to simulated UBB impact loading conditions under a controlled laboratory set up. A detailed overview of the sled system is discussed in the following section.

1.11 Horizontal sled system

The WHAM III sled deck measures 4 x 2 m and is capable of producing deceleration pulse controlled by a hydraulic decelerating mechanism. A set of two parallel rails were mounted to the sled deck. A vertical rigid seat was reclined (rotated along the global Y axis) so that the seat back was parallel to sled deck and rails. Linear roller bearings were attached to the rear aspect of the seat fixture and it was positioned onto the rails and coupled to the rails with retention brackets. The roller bearings and the retention bracket assemblies illustrated in Figure 4-1 allowed the rigid seat to move freely on the rails during the impact event.

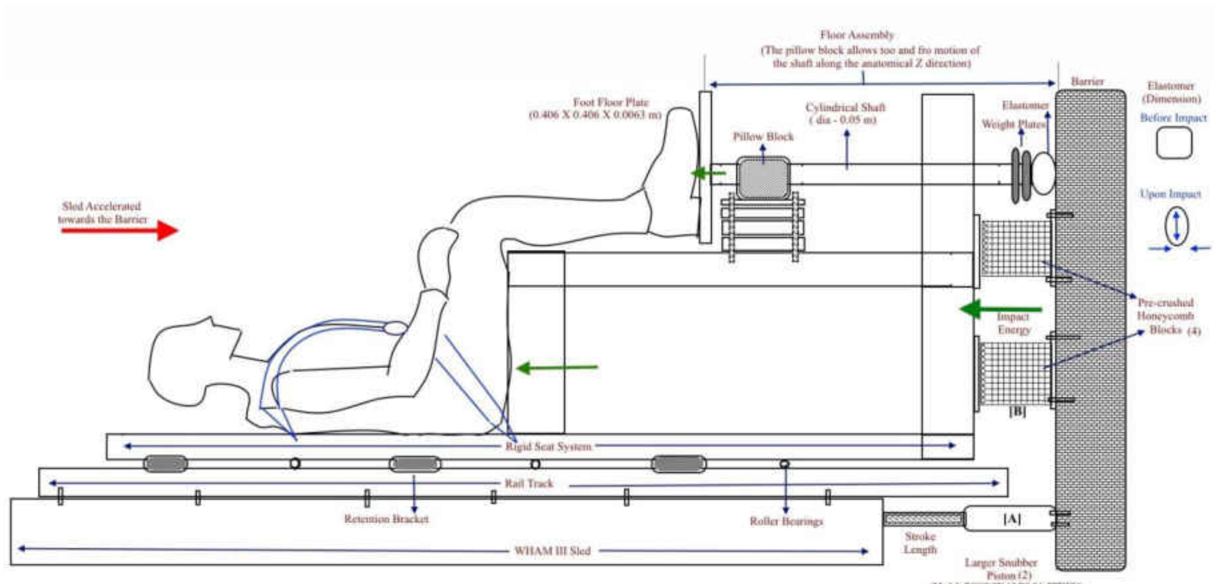

Figure 0-1: A lateral view of the horizontal sled system with the occupant positioned on the seat with a 5-point belt.

A movable foot floor assembly capable of producing independent foot floor pulse consists of a 0.406 m by 0.406 m by 0.0063 m floor plate, a linear bearing system, a 0.05 m diameter cylindrical shaft, and an elastomer. The cylindrical shaft was rigidly connected to the floor plate on the occupant end (Figure 4-1). The linear bearing system was mounted to the seat fixture and it was designed to constrain the motion of the shaft to move along the anatomical Z direction only. On the barrier end, the cylindrical shaft was connected to an elastomer to allow impact to the rigid barrier independent of the seat motion (Figures 4-1 and 4-2). Before the test, the movable floor system was adjusted along the anatomical X axis so that the line joining the centers of the occupant's feet was orthogonal to and at the level of the cylindrical shaft. The sled was accelerated to a target velocity before the external force was released for the last 9.75 m of travel. Two large capacity snubber pistons (model RCOS 3X 12 BS 04 Efdyn Inc., OK) which were mounted to the barrier (Figure 4-2) were used to decelerate the WHAM III sled while allowing the seat system to continue the forward motion. Four pre-crushed aluminum honeycomb blocks which were attached to the barrier (Figures 4-1 and 4-2) were used to arrest the seat motion, while allowing the foot floor- shaft-elastomer assembly to impact the barrier directly. The total cross-sectional area and crush strength of the pre-crushed aluminum honeycomb blocks determined the deceleration pulse length. By controlling these two parameters, the crash pulse of the seat can be adjusted.

At the foot floor plate, the elastomer attached to the cylindrical shaft first deforms upon impact and then returns the stored energy and pushes the floor plate towards the occupant's feet. The stiffness of the elastomer attached to the cylindrical shaft determined the floor pulse magnitude, while the time to peak velocity for the floor pulse was adjusted by adding the weight plates to the barrier end of the shaft. Based on the weight added, the energy absorbed by the plates delays the time to peak for the floor pulse. During the test preparation phase effort were made to avoid any gap between the elastomer and the barrier, and between the seat and the pre-crushed honey comb blocks. This was carried out in order to achieve same time of arrival for both the seat and floor pulse.

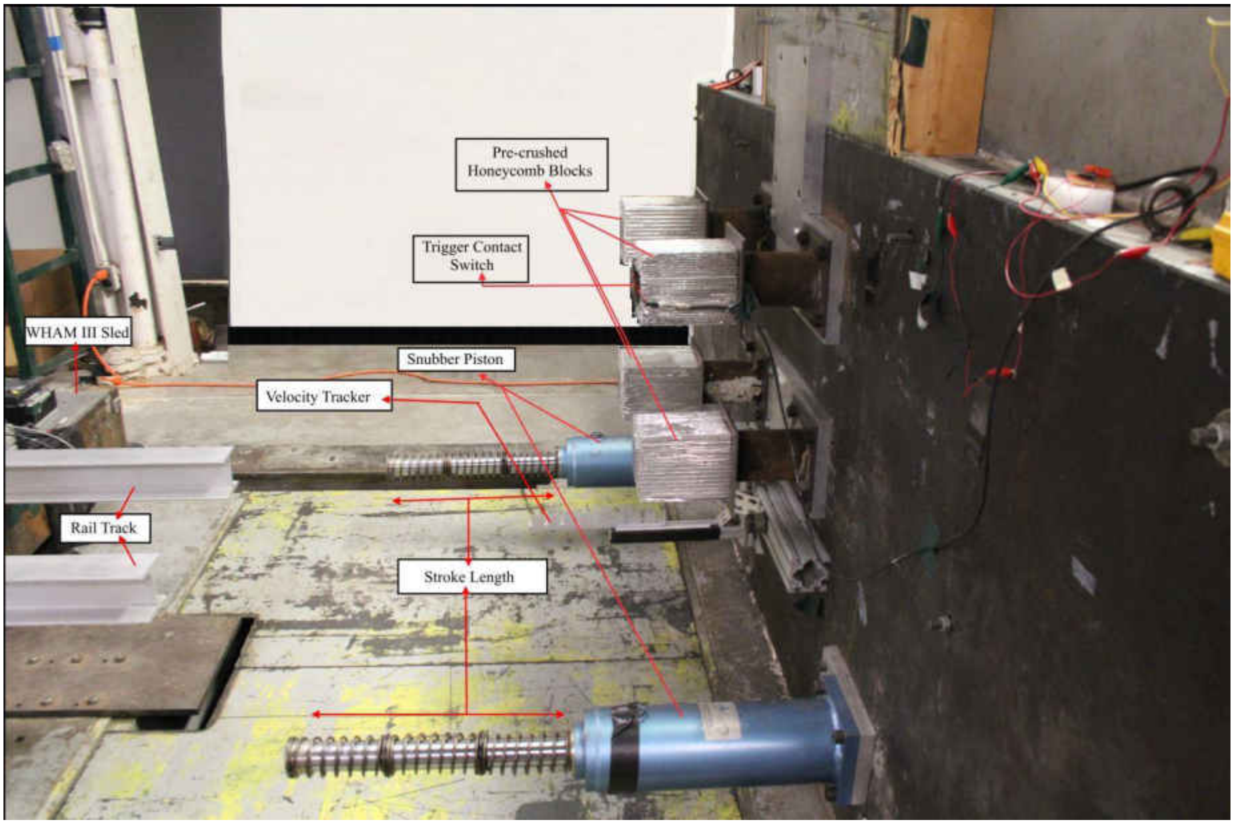

Figure 0-2: Two large capacity snubbers mounted to the barrier to slow down the WHAM III. Four pre-crushed aluminum honeycomb blocks attached to the rigid barrier to produce short duration seat acceleration.

1.12 Data acquisition and camera setup

A slice Pro (Diversified Technical Systems, Inc., CA) data acquisition system was used for each test to record 98 channels of data, including eleven 6DX blocks, strain gauges, contact switches, seatbelt load cells, fixture velocity, and floor and seat accelerations. The mounting locations of these 98 channels are listed in Appendix B. All the channels were sampled at the rate of 500,000 samples per second with a 100 kHz anti-aliasing, multiple low pass Butterworth filter. The event was recorded using two NAC GX-1 cameras (NAC Image Technology, CA) each with a 24 mm Nikon lens. One camera recorded the lateral view of the event, while the other camera recorded an overhead (frontal) view. The lateral view camera was positioned 1.57 m from the right side edge of the seat. The overhead camera was mounted 1.77 m from the top of the floor plate. Each camera recorded at 2000 frames per second, with the image resolution set to 1280 X 1024 pixels and exposure time set to 5 microseconds.

For each test, both DAS and cameras were triggered using a switch attached to one of the pre-crushed aluminum honeycomb blocks mounted to the barrier. During the event, the seat made contact with the honeycomb block and sent a trigger signal to the cameras and Slice Pro data acquisition system. An IRIG Synchronized Time Code Generator Unit (Model GS-101, Orca Technologies, CA) was used to send a synchronization signal to the cameras. This unit uses a stable external time code for reference. In addition, a visible flash was captured on the video and used to determine time zero to synchronize the video and sensor data.

1.13 Loading Condition

Using the horizontal sled system, two whole body PMHS tests were conducted to define the orthopedic response within the body to UBB loading. Both specimens were tested under the same conditions: seat at 4 m/s at 10ms time to peak (TTP) with floor at 6 m/s at 5ms TTP. The seat and the floor were equipped with a 7270 accelerometer. The peak velocity and time to peak were the input variables. The seat and floor velocity were obtained by integrating the 7270 seat and floor accelerometers, respectively, while time to peak and peak velocity were measured using the TICE method reported by (Spink, 2014). The corresponding peak acceleration, peak velocity and time to peak for each specimen are shown in Table 4-1. In addition to the 7270 accelerometers, the seat and the floor acceleration were determined using a low frequency foam insulator accelerometer (Endevco 2262). The representative acceleration and the integrate velocity curves are shown in Figure 4-3. The floor pulse in Test 4 procced the seat pulse by 0.96 ms. The potential reason could be the sled setup during the test preparation phase. The sled setup relative to barrier is explained in the section 4.1. Both the tests were completed with a rigid seat and 90° angle at the ankle, knee and hip.

Table 0-1: PMHS impact test measured input parameters.

Input variables	WSU-003/OSU 6908	WSU-004/LMD 14-00355
Peak Floor Velocity (m/s)	6.29	6.13
Time of Peak (ms)	6.24	6.87
Time of arrival (ms)	0.80	1.76
Time to Peak (ms)	5.44	5.11
Peak Seat Velocity (m/s)	4.72	4.47
Time of Peak (ms)	13.17	11.59
Time of arrival (ms)	1.58	1.80
Time to Peak (ms)	11.59	9.79
Peak Seat Acceleration (g)	129	139
Peak Floor Acceleration (g)	230	264

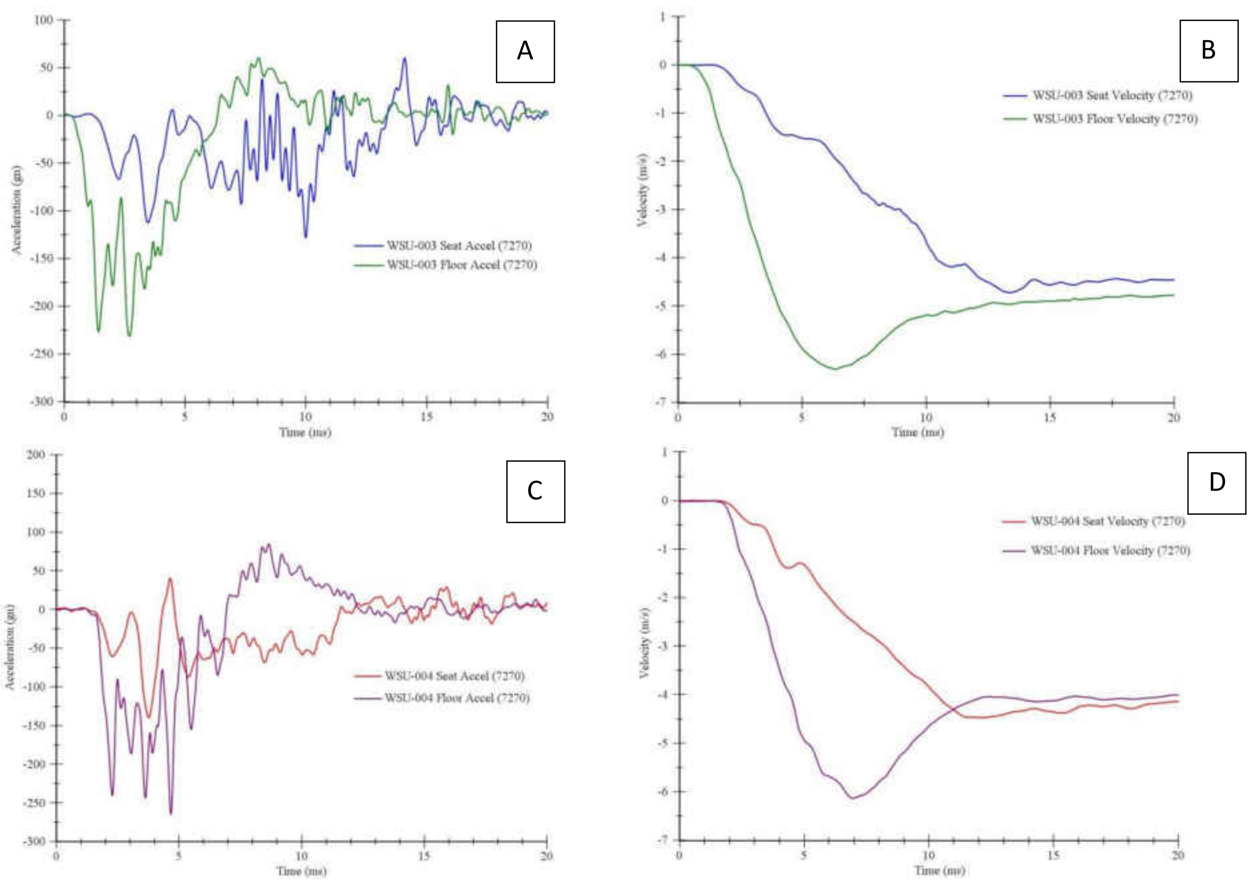

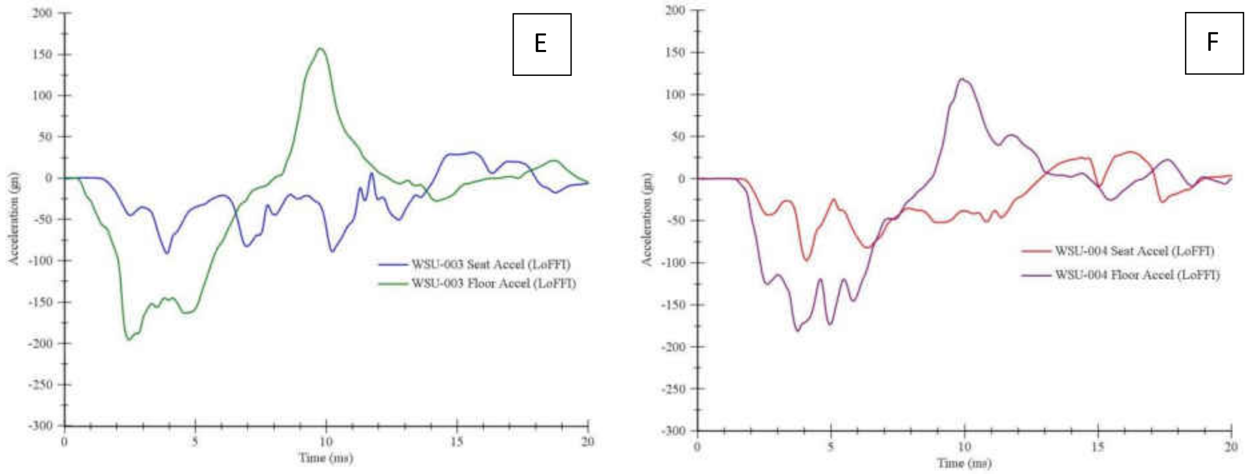

Figure 0-3: Structure acceleration and corresponding velocity curves are shown in sequence (A: WSU-003 Acceleration (7270 accelerometer), B: WSU-003 Velocity, C: WSU-004 Acceleration (7270 accelerometer), D: Test WSU-004 Velocity, E: WSU-003 Acceleration (LoFFI accelerometer) and F: WSU-004 Acceleration (LoFFI accelerometer)).

1.14 PMHS preparation

Two un-embalmed PMHS specimens were used for these tests. Table 4-2 represents each cadaver's age/stature and mass, bone mineral density, and previous injuries. A detailed overview of cadaver preparation, instrumentation procedure, pre-test sled preparation, and data processing and analysis are discussed in the following sections.

Table 0-2: Specimen matrix

PMHS ID	**Bio-parameter**	**BMD measurement**				**Comments**
		Region	BMD (g/cm^2)	T Score	Z score	
WSU-003 OSU 6908	Height - 177 cm Weight-67.5Kg Age- 74	AP Spine	1.36	0.9	-	Diffuse arthritic findings with bridging osteophytes at C4/C5 and C6/C7
		Whole Body	1.191	-0.4	0.7	
WSU-004 LMD 14-00355	Height - 177 cm Weight-77.29Kg Age- 69	AP Spine	1.099	0.1	0.9	Old left nasal bone fracture. 12 cm cavitary mass in the left hemi-thorax

1.14.1 Specimen characteristics

Both the cadavers were male with a body mass of 67.5 kg and 77.29 kg respectively for the two specimens (Table 4-2). Before acquiring the specimens, a bone mineral density check was performed. For both tests, BMD was measured using Dual-energy X-ray Absorptiometry (DXA). The lumbar spine (L2-L4) was the primary region of interest. In addition to the lumbar spine scan, a whole body DXA scan was performed for the OSU specimen. The World Health Organization's defines bone mineral density with T-score between +1 and -1 as normal while between -1 to -2.5 as osteopenia and further below -2.5 as osteoporosis. The specimen matrix in Table 4-2 shows that the T score and Z score for both specimens were within the normal range. The Spine mineral density for OSU specimen was determined to be 1.36 g/cm^2, while for LMD specimen had a spine mineral density of 1.099 g/cm^2. However, the individual lumbar spine segment BMD measurement for the OSU specimen predicted the presence of osteopenia at the L1 vertebral body with a T-score of -1.4.

After a detailed evaluation of each test subject's bone mineral content, the specimens were shipped to the testing facility by the vendor. The frozen specimens were then thawed about 24 – 36 hours before preparation. The PMHS weight and detailed anthropometry measurements were noted (the summarized measurements are available in Appendix A). Based on the measured foot length and breadth, combat desert boots of appropriate sizes were ordered. Next, the specimens were taken to Oakwood Hospital (Taylor, MI) for the pre-test computed tomography (CT) scan. All the scans were performed using an axial CT scanner with a slice thickness of 0.625 mm and a plane resolution of 512 X 512 pixels. CT images were measured in Hounsfield units. The pre-test images of the test subjects were used to determine local bone dimension and segmental masses. A second set of CT scans was taken after the instrumentation at the same hospital. Post-instrumentation CT images provided the location of the mounts and 6DX blocks in the body. After the testing, the subjects were again scanned to visualize any post-impact injuires. Table 4-3 summarizes the rationale for performing the CT scan.

Table 0-3: Rationale for performing CT scans.

CT scan	Type	Analysis
Pre-Instrumentation Scan	Before Instrumentation	To screen for any pre-existing fracture or surgery condition
Post-Instrumentation Scan	After Instrumentation	To check the alignment of the Transducer and mounts with the desired anatomical orientation
Post-Test Scan	Post Impact Test	To analyze, possible injury due to impact

1.14.2 Instrumentation

PMHS and ATDs have been routinely equipped with accelerometers, load cells, and strain gauges to measure the response to impact loading conditions. Similar instruments were implemented for blast condition loading. Sensors with a larger dynamic range are required to handle the harsh loading conditions. Each specimen was instrumented with the DTS 6 axis degree freedom block.

Acceleration, angular velocity, and strain data were an integral part of evaluating an occupant's biomechanical response. Acceleration and angular rate were measured using DTS 6DX-Pro sensors, while Vishay's uniaxial (C2A-06-062LW-350) strain gauges were used to determine fracture timing. Table 4-4 represents the instrumentation matrix used for cadaver testing (Detail channel assignment is shown in Appendix B). Instrumentation protocol by (Pintar et al., 2013) was referred to for mounting the motion blocks and strain gauges to the test specimen.

Table 0-4: Cadaver impact test instrumentation matrix.

Sensor Type	Manufacturer	Model	Number
Linear Accelerometer	Endevco	7270	6
Six DOF Block	DTS	6DX PRO	11
Strain Gauge	Vishay/MM	C2A-06-062LW-350	12
Foot Contact Switch	__	__	1
Seat Belt Load Cell	Denton	1910	4
LoFFI Accelerometer	Endevco	2262	2

1.14.2.1 6DX transducer mounting technique

The DTS 6-degrees of freedom block features three linear accelerometers and three angular rate sensors. The transducers were mounted to 11 regions that were expected to receive a high frequency impact signal. These regions included the right and left tibiae and femurs, the sacrum spine (S1), the thoracic spine (T1, T5, T8, and T12), the sternum and the head. In addition to the 6 DX blocks, an Endevco 7270 accelerometer was mounted on the medial surface of the calcaneus bone of each foot. Due to the uneven surface on the skeleton structure, it was not feasible to mount the sensor directly to a defined anatomical landmark. Therefore, separate aluminum mounts were fabricated for each region to match the contour of the bony surface. The 6DX block was bolted to each mount, respectively. The corresponding sensor mounting location and the dimension of the mount are summarized in Table 4-5 for each bony region.

The preliminary procedure for all the instrumentation was the same. First, the desired anatomical location for each region was marked with a black marker on the skin. The anatomical locations are listed in Table 4-5. Second, the soft tissue was dissected using a scalpel blade to expose the bone. Next, the region based aluminum mounts were taken and fixed to the bone. The mounting technique for each region is discussed separately as follows.

For the head and sternum, a 19mm X 19mm X 4.5mm aluminum plate was screwed into a flat surface of the cortical bone. Figure 4-4 A shows the mount used at the interface between the bone and the sensor for the head and sternum. For the lower extremity, a 20mm X 20mm X 25mm aluminum mount was attached to the long bones using hose clamps. Compared to the femur mount, the inner surface of the tibia was elliptical as shown in Figure 4-4 B. The rationale for an elliptical design was to match the anterior contour of the tibia bone, which has a prominent surface compared to a femur bone. After instrumenting the mounts, the 6DX block sensor was attached. Care was taken to position the transducer in the desired direction. The 2014 SAE J211 standard coordinate system was referenced for defining the axis direction for each 6DX block. It is difficult to locate the vertebral body by palpation. Thus, x-rays were used as a guide to find the desired location of the pedicle of the vertebra.

Table 0-5: A summary of the anatomical landmark and steel mount installation technique for each body region, respectively.

	Head (L_F)	Sternum	Lower extremity	Spine(L_F) /Pelvis
Anatomical Location	30mm above (mid-coronal plane X the Frankfort plane)	Midpoint of the line (superior sternum notch - xiphoid process)	Distal Tibia- Range (0.20L to 0.30L from the lateral epicondyle) Distal Femur- Range (0.15L to 0.25L from the medial malleolus)	Thoracic spine (T1, T5, T8, T12) Posterior aspect of the neural arch Pelvis – Posterior aspect of S1
Mount Dimension	(19 X 19 X 4.5 mm) square aluminum plate	(19 X 19 X 4.5 mm) square aluminum plate	(20 X 20 X 25 mm) aluminum block. The mounting surface of the block matched the contour of the bone.	aluminum mounts of different depths were fabricated to accommodate the desired spinous process
Installation Technique	Screwed to the skull bone	Screwed to the cortical bone	The Worm-drive/hose clamp method was used to secure the mount in position	Each mount has two guide holes for screws

Note: ‘L’ - total length of the specified bone; ‘L_F’ – mount installed on the left side.

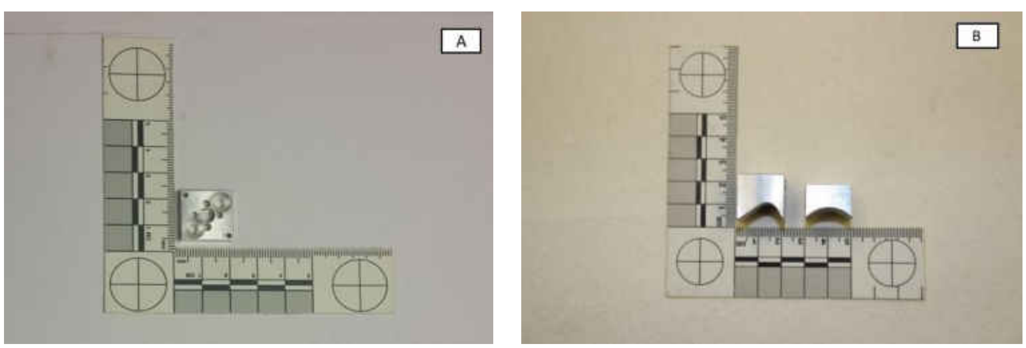

Figure 0-4: The head and sternum steel plate [A], and the tibia and femur mounts [B], respectively.

In the current study, the spine biomechanical response was measured using the 6DOF mounted to four thoracic vertebra (T1, T5, T8, T12), while the pelvic response was obtained from the 6DOF instrumented at S1. The complex morphology of the spine and the pelvic region made it difficult to determine the exact pedicle location of the vertebrae. Hence, an orthopaedic resident from the Wayne State School of Medicine provided assistance. First, with the help of digital x-ray imaging, the approximate pedicle location of the desired spine was marked with the help of a trochanter needle. Second, soft tissue was dissected exposing the desired spinous process. Spine instrumentation was installed so that it fit over the spinous process as closely as possible, with the screw tip in the pedicle of the vertebral body. Pedicle anatomy variation between the thoracic spine as well as the spine deformity makes it difficult for pedicle screw instrumentation (Chung et al., 2008; Kim et al., 2004; Zeiller et al., 2005). The free hand technique reported by Mattei et al. was referenced to determine the pedicle location for thoracic and sacrum spine instrumentation (Mattei et al., 2009). Table 4-6 shows the sagittal and transverse angle measurement to locate the thoracic spine pedicle.

Table 0-6: Transverse and sagittal angle the thoracic spine pedicle angle measurement.

Spine	Sagittal angle (Cranial-caudal)	Transverse (medial-lateral)
T1	-14°	22°
T5	-11°	13°
T8	-6°	9°
T12	4°	14°

Once the pedicle location was determined, the spine mounts were installed. A variety of spine mounts with different depths were fabricated to accommodate spinous process variation, as shown in Figure 4-5 A. After installing the spine mounts, a 19 X 19 X 4.5 mm plate was bolted to its left lateral side. For the sacrum, the plate was attached to the top of the sacrum. Next, the 6DX sensor was mounted to the plate. Figure 4-5 B, C, D shows the top and lateral view of the spine mount assembly.

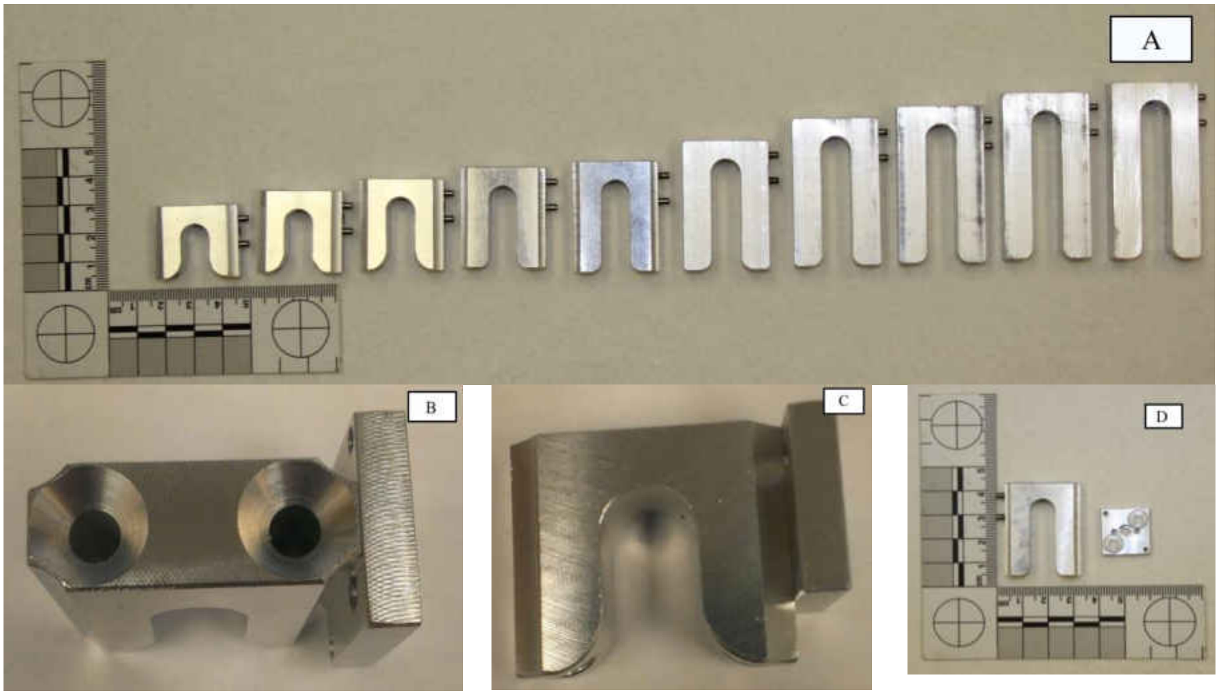

Figure 0-5: The spine mounts fabricated with different depths [A] and Individual spine mount assembly [B, C, and D].

The sacral instrumentation technique was the same as the spine. Due to the lack of a prominent sacrum spinous process, the mount was modified so that the plate was attached to the spine mount on the top instead of on the lateral aspect of the mount (Figures 4-6 A and B). After installing the sensor, the skin along the spinal column was sutured back into position. Figure 4-7 shows the 6DX block mounted to the right distal femur and T5 spine, respectively.

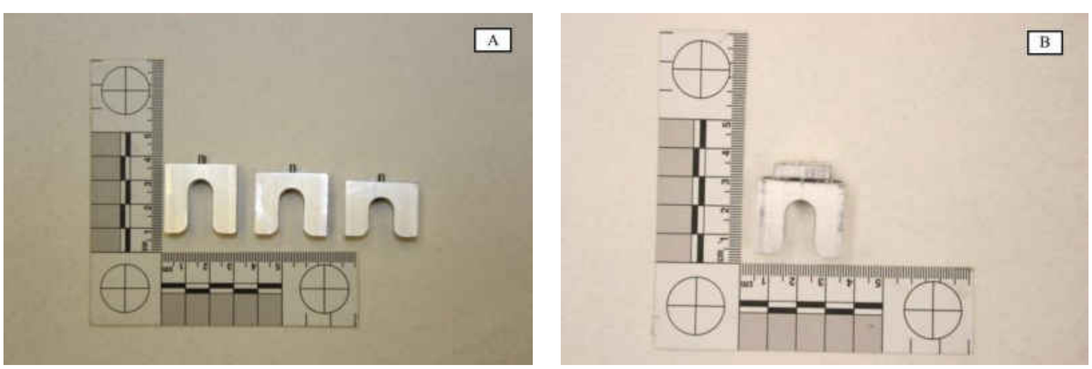

Figure 0-6: Sacrum mounts fabricated with different depth [A]. The Individual sacrum mount assembly [B].

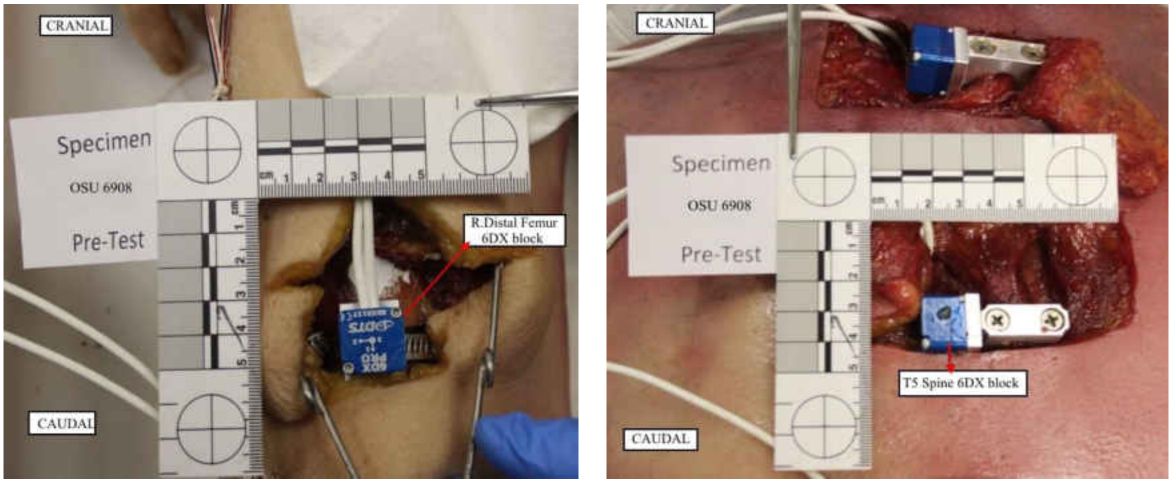

Figure 0-7: A 6DX sensor mounted at the right distal femur [A] and T5 vertebra [B], respectively.

1.14.2.2 Strain gauge installation procedure

A total of twelve uniaxial Vishay (C2A-06-062LW-350) strain gauges were used for each test. A strain gauge was glued to each lower extremity (distal and proximal tibia, distal femur and calcaneus) anterior superior iliac spine and superior pubic rami. The uniaxial gauges were orientated in the direction of the transmission of the primary load. A standard protocol was developed for installing the strain gauges. First, the desired anatomical landmark was marked on the specimen. Next, the soft tissue was dissected to expose the bone surface, and the periosteum of the bone was scraped off using a spinal curette or scalpel blade. Effort was made to maintain the integrity of the bone. Further, the bone surface was rubbed with an acetone-soaked gauze pad to remove any tissue affixed to the bone. Next, the bone was brushed with a Micro-Measurements 200 Catalyst-C solution. After 2 mins, two to three drops of Micro-Measurements M-Bond 200 Adhesive were applied to the same location and spread to a thin layer using a cotton swab. After 3 to 5 mins, the surface was made rough using a scalpel blade. Once the bone was prepared, a strain gauge was taken and its bottom surface was brushed with a catalyst solution. Again, one to two drops of adhesive were applied to the same bony location that was prepared. Next, the strain gauge was placed on the prepared bone and held with gentle pressure for 5 to 10 mins. Finally, the gauge orientation and adhesion were inspected, and a thin layer of Micro-Measurements M-Coat D acrylic coating was applied on the glued strain gauge. After 10 to 15 mins, the region was sutured. Figure 4-8 A-C shows the proximal tibia strain gauge installation procedure. After installing the 6DX block and strain gauge, the cables were relieved of strain using sutures and zip ties. The cables on the left and right sides of the body were bundled together. These cables were then plugged into the Slice-Pro modules, respectively. Each cable was labelled with an appropriate anatomical landmark on both ends. After a sensor functionality check, the specimen was prepared for the pre-test CT scan.

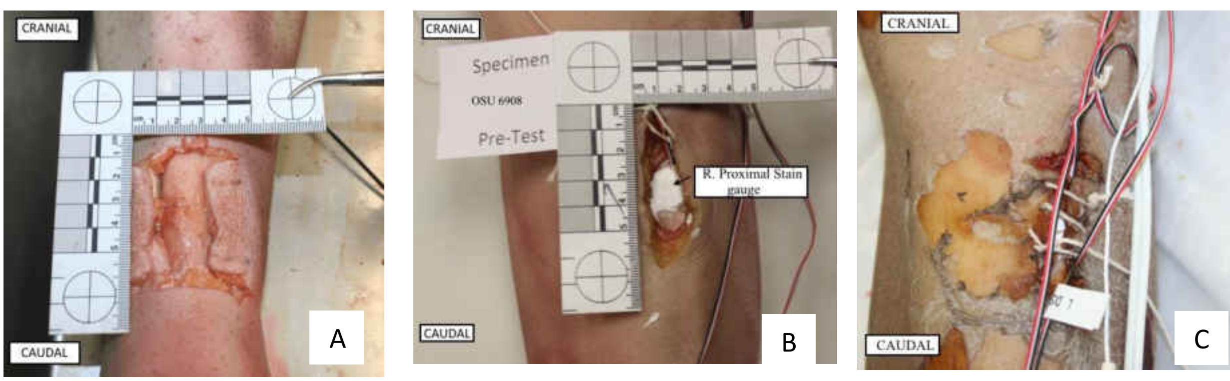

Figure 0-8: Strain gauge installation sequence.

1.15 Specimen positioning

After installing all the transducers, the PMHS was donned with a blue Lycra bodysuit. All of the instrumentation procedures were carried out before the test date. On the day of the experiment, a post-instrumentation CT scan was performed followed by the positioning of the specimen on the WSU horizontal sled. Before positioning, PMHS feet were donned with a properly- sized pair of lightweight desert combat boots, and the laces were tightened in a sequence from the foot to the ankle. Using a fish scale axial tension of 50N and then 100N was applied while tying the boot laces. Further, the back and the bottom of the boot heel were tapped with polymer mallet in order to remove any gap between the PMHS heel and the boot's interior. Each specimen was positioned initially using a 5-point seatbelt system on the horizontal sled, with the torso resting on the seatback, the buttocks touching the seat bottom and the feet against the footplate. The goal of the vertical impact testing under a laboratory setup is to mimic a live theater underbody blast event and to examine the seated occupant injuries under such an explosion. Hence, the test subjects were positioned to replicate the seated soldier postures. Orientation of the pelvis, spine and lower extremity relative to the seating posture is an essential parameter to be considered for accuracy and precise characterization of injury (J Ruppa, 2013). A Portable Romer Arm (Hexagon Metrology Inc., CA) (a coordinate measurement machine CMM), was used to measure the position and to adjust the pelvis angle. C7 was then adjusted with respect to the anterior superior iliac spine (ASIS) midpoint, the orientation of the tragion and infraorbital positions were set with respect to each other and C7. In addition, the lower legs were oriented parallel to the seat back with the sole of the boots against the floor plate, respectively. A positioning script was written in PC-DMIS software (Hexagon Manufacturing Intelligence, RI) to measure and report key anatomical locations and positions.

1.15.1 Positioning Protocol

After the initial positioning of the specimen on the horizontal sled system, the portable Romer Arm was mounted to the sled. The three-dimensional coordinates of the seat and key PMHS landmarks were captured by using a 6mm contact probe attached to the CMM system. A brief overview of the positioning steps follows. All the procedures here are reported with respect to the horizontal sled system.

1. Three points were taken on the seat bottom. Four points each on the seat back and four points on right side of the seat edge were captured. Based on these coordinate points, the PC-DMIS script generated a three axis orthogonal system.
2. Anterior superior iliac spine (L/R) and pubic symphysis coordinate points were recorded. Due to the thick layer of soft tissue in the lower abdomen area, it was difficult to palpate these regions. Hence, during 6DX block installation, three radial steel hemispheres each on the right and left ASIS and the pubic symphysis were glued, respectively. A plane was defined by those three points which delineates the pelvic angle. Positioning documentation requires that the pelvic angle should be $46^0 \pm 5$ relative to the seat bottom. The script determines the angle between the pelvis and the seat bottom plane. If the angle is out of tolerance, then the specimen pelvis needs to rotate relative to the seat to bring the angle within the defined limits. For most specimens, the correct pelvis position was achieved by rotating the pelvis forward via foam blocks underneath it.
3. The C7 spinous process coordinate point was measured. With respect to the ASIS midpoint, C7 should be 90 ± 10 mm rearward to the midpoint of the line joining the right and left ASIS points. If the measurement is out of tolerance, the torso of the subject needs to be adjusted. This was typically accomplished using two foam wedges, each one below the right and left shoulder blades.
4. The feet were rested on the footplate and an effort was made to position the soles of the boots flat against the surface of the floor. Due to the horizontal sled system, the boots were not in contact with the foot plate. Hence, initially until final position of the specimen is achieved, the toes of the boots were taped with masking tape against the foot plate. Before the sled was accelerated, a small cut was made in the tape so that upon

impact the foot was allowed to move freely relative to the floorplate. Also, an effort was made to keep a distance of 295 ± 10 mm between the lateral boot heels. Next, the lower legs were shifted up and down in anatomical X direction to get the line joining the lateral femoral epicondyle and the lateral malleolus in parallel with seat (± 2° tolerance). Further, the knees were adjusted to get the patella in the same sagittal plane as the midpoint between the lateral and medial malleolus landmarks.

5. Using the Romer arm, the left and the right acromion landmarks were positioned within a 20mm tolerance limit in both X and Z direction (global coordinate system). While adjusting the shoulder, care was taken to keep C7 position within the tolerance range.
6. Keeping the head in the centerline of the subject sitting posture, tragion landmark coordinate points both left and right, were measured. As per the protocol, the tragion point should be 85 ± 10 mm above C7 (z-axis). Next, with respect to the tragion points, the head was rotated along the y-axis to position the infraorbital points within 10 ± 5mm above (z-axis) the tragion points.
7. The final step includes recording the anatomical landmarks and motion target markers for the elbow, the ulna, and the seat belt coordinate points in 3D space. Although the positioning document specifies how to measure T1, T4, T5, T12 and L3 spinous process landmarks, due to the horizontal sled system these anatomical locations were not accessible.

The relevant coordinate points measured for WSU-003 and WSU-004 tests, respectively are shown in Appendix A. Figure 4-9 represents the pelvis angle measured for tests 003 and 004, respectively. Care was taken to keep the angle between the torso- thigh, thigh-lower leg and lower leg foot at 90°. After recording all the vital landmark points, the shoulder and lap seat belts were tightened using a fish scale and a vice grip with an axial tension of 100N.

Next, multiple target marks were applied to the specimen for 2D kinematics analysis. These markers were glued to 9 anatomical locations as per the protocol reported by (J Ruppa, 2013). The list of anatomical locations are shown in Table 4-7, and its 2D displacement was tracked frame by frame from Time zero to 650 ms using TEMA motion tracking software. In addition, markers were also applied to the greater trochanter, nasion, mental protuberance, and lateral ulnar head process, respectively, for general kinematic analysis. After capturing the relevant coordinate points, the effort was made to maintain the final position of the specimen relative to the sled. Both the arms were taped using masking tape against the torso. Likewise, the legs position was maintained by a masking tape around both the knee, so that the legs do not fall latterly. Figure 4-10 A shows the final position of the test- 004 specimen.

Table 0-7: Anatomical locations for motion target markers (J Ruppa, 2013).

Anatomical region	Target marker location
Lower extremity	Lateral malleolus, Boot (heel and toe), Lateral epicondyle, Patella
Head	Infra-orbital notch, tragion
Shoulder	Acromion, proximal humerus

Figure 0-9: Pelvis angle measured by the Romer arm for Tests 3 and 4, respectively.

1.16 Pre-test sled preparation

Once the final position of the test subject was achieved, a portable x-ray unit was used to record the final position of the PHMS skeleton on the sled. Figure 4-10 (B - D) shows the lateral x-ray image taken of the subject on the sled prior to impact. The x-rays were used to make sure that the angle at the knee and ankle joint were 90°. In addition, a lateral x-ray image of the lower torso region provided a preliminary overview of the sacrum orientation relative to the seat back and seat bottom, respectively. After x-rays, the sled preparation procedure is completed.

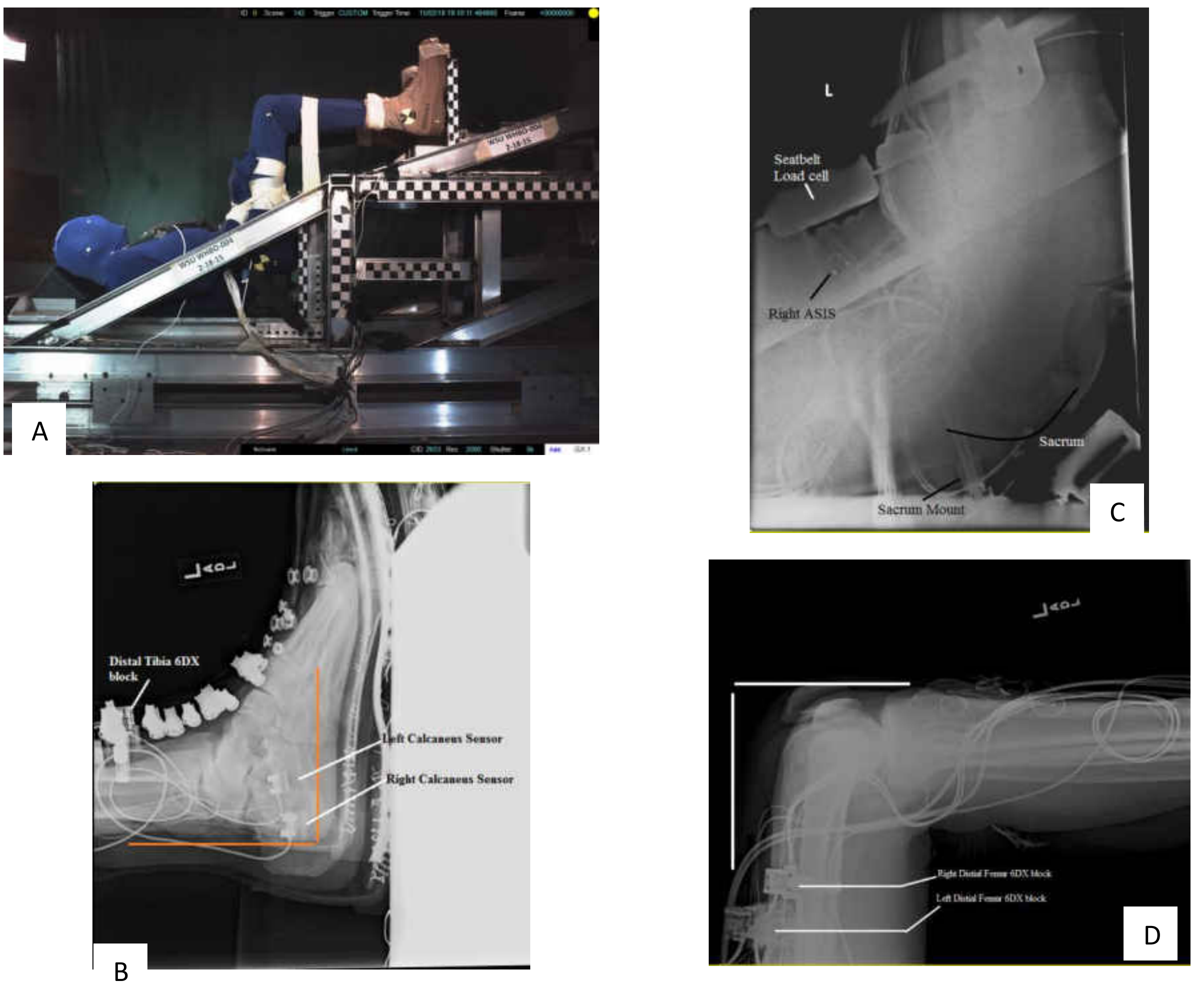

Figure 0-10: A- Final specimen position for test 4 loading conditions prior to impact. B- The contact between the foot/boot and boot/floor plate, respectively. C- The buttock contact with the seat bottom. Also, the tail end of the sacrum is observed in the same image. D- The knee angle between the femur and tibia. Along with the angle verification, the orientation of the 6DX block on anatomical landmarks could also be examined using lateral X-ray images.

First, all the cables were taped down to the WHAM III sled and the sensors were connected to the Slice Pro module. While taping down the cables, care was taken to provide enough slack so that during the impact event, the horizontal seat could move freely on the rail without causing any damage to the cables. Sensor functionality and offset were also rechecked.

Next, the whole WHAM III sled along with the specimen was pushed 78 feet away from the barrier. The specimen position, seat contacts, such as the buttock/seat bottom, feet/floor pan, and head/setback distance, were all captured with a digital camera for documentation purposes. Next, a small cut using a scissors was made in the masking tape attached between the boot and footplate. A Similar cut was made on the masking tape attached between the knees, and between the arm and torso. This cuts allowed the arms and legs to move freely upon impact relative to the sled. Once the specimen and the sled were ready for the impact, the hydraulic pneumatic system was pressurized to 21 psi, which corresponded to 4m/s seat loading conditions. Depending upon the loading condition, the pressure level was changed. Before the impact, the sled track was cleared, and all the doors leading to the sled area were locked. Once the sled is ready for the impact, the event button the slice pro module was turned on. Hence, the data recording starts at this point and in total the module records the data for duration of 45 seconds. Finally, the sled and the specimen were accelerated towards the barrier.

1.17 Post-impact procedure

Following the impact, the specimen's position on the sled post-test was photographed for documentation purposes. Next, the video and the raw sensor data recorded by the cameras and the Slice-Pro were, respectively, downloaded. The video was downloaded in (.MCF) format, while the 6DX raw data was in (.TVS) format. As mentioned in the previous section 4.6 the slice pro module record the data for duration of 45 seconds. However the actual event starts after 17th seconds. This initial 17 seconds is taken by the sled to reach the barrier.

After uploading all the raw data to the local server, the PMHS was transferred to the cooler. The sled system and the impact area were sanitized. On the following day, the specimen was de-instrumented. During this procedure, the skeleton, especially the parts that were instrumented, was palpated for signs of fracture. The PMHS was then taken for a post-impact CT scan with the instrumentation mounts still attached. CT parameters were the same as the pre-test CT scans. After the CT all the mounts were removed from the specimen and sanitized. During this procedure, the strain gauges were inspected thoroughly for any delamination. Next, the test subject was prepared for a post-impact autopsy. Prior to autopsy, a board certified radiologist analyzed the post-test CT scans for any signs of impact trauma using the CT findings as a guide an autopsy was conducted by a board certified pathologist to confirm the radiologist's findings and also to inspect for any injuries which were not apparent through the CT review.

1.18 Data processing

98 channels of data were collected for each test. Post impact sensor and video raw data were collected in delimited ASCII format (.TSV file) and (.MCF file) format, respectively. Each numerical data was assigned with header information that includes the channel specification. The data processing included four stages: Converted, Processed, Calculated and Scaled. The Converted staging included the engineering unit assignment, offset removal, polarity check and trimming the numerical data. In Processed staging, filters were applied and the target markers' 2D displacements were traced using TEMA motion tracking software. The calculated staging included the transformation of acceleration and angular rate signals to align with an anatomical

coordinate system related to the bone on which the 6DX block was mounted. Furthermore, the feet motion at the ankle and the resulting acceleration and angular rate data were calculated. Finally, the Scaled staging was concerned primarily with scaling the acceleration, as well as the motion data of the knee and shoulder, respectively. The numerical channels considered and the techniques applied for processing data in each stage are described in detail in the following sections.

1.18.1 Converted Staging

The raw (.TSV) format sensor numerical data files were exported to Python Feedparser 5.2.1. It is an object-oriented programming language which includes high- level data structure modules (Sanner, 1999). Further, the syntax used in Python are simple and yet powerful. The interpreter compiles the program automatically to a platform independent byte code (Van Rossum, 2007). The written script in Python was used for offset removal, numerical data trimming and a polarity check. The limit for trimming the data was referenced from (Pintar et al., 2013). Ten milliseconds before Time zero was considered as the start of the range, while the end range was determined by a head angular velocity signal. The head angular rate signal took a longer time to return to baseline compared to other sensor signals. The time at which the head angular rate signal returned to baseline after the impact event was considered as the end limit for trimming the other numerical data channels. Similarly, the raw video data were trimmed with a starting limit of ten milliseconds prior to Tzero. The end limit was set when the gross movement of the specimen was stopped completely.

1.18.2 Processed staging

Primarily, this staging is concerned with filtering the sensor data and tracking the specimen motion during the event. The Converted angular rate signals were filtered using a 1650Hz digital filter, while the remaining signals were filtered using 3000 Hz digital filter. The motion block provided the acceleration and angular velocity data of the structure on which the motion block was mounted, while strain gauges were used in an effort to determine the timing of fractures and to examine the strain through the desired bone during the impact. Next, the test subject kinematic during the event was examined by tracking the target markers' 2D displacement using TEMA motion tracking software. The target markers used for tracking specimen motion and the corresponding anatomical location where it was applied are shown in Table (4-8). The steps involved in the kinematic analysis are described in the following section.

1.18.2.1 Kinematic analysis using video

Each target marker was tracked frame by frame for both lateral and overhead views. The lateral camera was used to view the lateral aspect of the specimen motion (anatomical Z and X direction), while the overhead camera captured the frontal view of the specimen motion (anatomical Z and Y direction). The following procedure describes the technique used to track the markers using TEMA software.

A) The video file (.avi) was created and opened into the TEMA software. The frame rate was set to 2000 fps.

B) The scale factor for tracking was calculated by dividing the pixel distance between two target points on the seat pan with the actual distance between the same points.

C) In addition to a scale factor, the 2D frame distance from the camera was set at 1.6 m for the lateral camera, while in the overhead camera the value was measured to be 1.78 m. (Lateral measurement- the distance between the right side seat to lateral camera lens. Orthogonal measurement – the distance between the overhead camera lens to the top surface of the foot plate).

D) Next, the offset for each target marker was set. This was achieved by measuring the distance between the plane used to set the 2D frame distance and the desired target marker. CMM coordinate points were used for the latter measurement.An example is the infraorbital target marker in the lateral video view:

Offset value = Right side seat Y coordinate point – infraorbital Y coordinate point

E) After setting the offset value for each marker, the target marker was tracked frame by frame for the specified duration.

F) The tracked displacement for each target marker was saved as Tab Delimited ASCII format (.TSV file).

Each body region motion was determined based on the tracked target marker in both the frontal and lateral view. The lateral epicondyle marker displacement provided knee motion in the anatomical X and Z axes (lateral aspect), while the patella marker motion gave knee motion in the anatomical Z and Y axes (frontal aspect). Similarly, shoulder displacement in the anatomical X and Z axes (lateral aspect) were determined by tracking the acromion or proximal humerus marker. Likewise, the head and foot lateral and frontal motions were provided by the corresponding target marker (Table 4-8) displacement, respectively.

1.18.3 Calculated staging

In this staging the numerical data from motion are transformed and aligned to the structure to which the 6DX transducers were attached. In addition, to coordinate transformations the following calculations were also determined.

1) Resultant Acceleration and Angular velocity
2) Head rotation in Torso XZ plane
3) Head rotation in Pelvis XZ plane
4) Spine compliance
5) Relative motion of the foot with respect to tibia (Foot motion about the ankle)
6) Shoulder motion relative to hip joint

1.18.3.1 Coordinate transformation

Acceleration and angular velocity were considered for analyzing the occupant's biomechanical response. Accurate evaluation of the linear acceleration and angular rate for each region during the impact event are essential to determining the injury mechanism as well as the development of a response corridor. Although the sensors were installed on the specimen based on the pre-defined protocol, during the pre-test positioning of the specimen there is a possibility for change in sensor orientation. Due to the need to compare responses across tests, it is necessary to transform the measured sensor data to the standardized local coordinate system. Transformation involved defining the local coordinate system for each bone and for the 6DX block. Next, the sensor coordinate system was aligned to the local bone coordinate system. Last, the acceleration and angular rate data were transformed to bone coordinate system.

1.18.3.1.1 Defining local anatomical and 6DX block coordinate systems

Eleven orthopedic regions (Table 4-8) which were expected to be susceptible to injury during an underbody blast impact were identified and instrumented with the 6DX sensor. Anatomical coordinate axis for each bone was defined as shown in Table (4-8). First, the three dimensional coordinates for each specified anatomical landmarks were extracted from the post-instrumentation CT scans using MIMICs Version 15 (Materialise, MI) image analyzing software.

Table 4-8 summarizes the required landmarks needed to define the local coordinate system and the corresponding coordinate axis defined for each region. In addition, the origin for each bone coordinate system was determined from the same CT scans. The origins for each bone are described in Table 4-8. The sensor coordinate system was determined based on the installed orientation of the 6DX block with respect to its sensitive axes. The origin of the sensor coordinate system was pre-defined by the manufacturer. Appendix D shows sensor orientation relative to the bone region.

Table 0-8: Summarized anatomical loandmark required to define the local bone coordinate system.

Region	Landmarks required to define coordinate system	Anatomical origin	Local bone coordinate definition		
			X axis	Y axis	Z axis
Head	L/R tragion, L/R Infraorbital	Head (cg) with jaw closed	Y-axis x Z-axis	vector left → right tragion	vector left tragion → midpoint of the line (L/R infraorbital – Yaxis)
Sternum	Suprasternal notch, Xiphoid process, L/R fourth rib anterior insertion points	Midpoint (suprasternal notch - xiphoid process along z-axis)	Z-axis x vector (left → right fourth rib insertion points)	Z-axis x X-axis	vector (suprasternal notch → xiphoid process
Thoracic Spine	L/R transverse process	Centroid of the vertebral body	Y-axis x vector (upper → lower endplates)	vector (left → right transverse process)	X-axis x Y-axis
Pelvis	L/R ASIS, L/R PSIS, L/R anterior pubic tubercles	Midpoint (left - right PSIS)	Y-axis x Z-axis	vector (left → right ASIS)	Vector (L/R PSIS midpoint → L/R ASIS midpoint)
Femur	M/L epicondyle, VL**, Greater trochanter posterior tip, Hip joint center	1/4th distance (knee joint- hip joint center; closer to knee) along Z-axis	Z-axis x vector (medial → lateral epicondyle)	Z-axis x X-axis	Vector (VL/posterior trochanter midpoint → epicondyles midpoint)

Tibia	Intercondylar tibial eminence center, Tibial tuberosity, M/L malleolus , Ankle joint center (midpoint of malleolus)	1/4th distance (ankle joint-intercondylar tibial eminence center; closer to ankle) along Z-axis	Y-axis x Z-axis	Z-axis x vector (intercondylar tibial eminence center →tibial tuberosity)	vector (intercondylar tibial eminence center → midpoint of M/L malleolus)

** Vastus Lateralus muscle attachment point along the greater trochanter superior surface.

1.18.3.1.2 Aligning the defined coordinate systems

The sensor coordinate points extracted from the CT images were then aligned with the local bone coordinate system. A script was written in the Python programming language for processing the coordinate transformation. The workflow of the script was as follows:

A) The unit vectors for both the bone and sensor coordinate systems were calculated. The unit vectors defined the axis component for the global coordinate system (calculation procedure obtained from (Kerrigan et al., 2008; Rudd et al., 2006))

B) Based on the unit vectors, a global matrix for the bone and sensor was defined.

C) Each global matrix represented the local coordinate system with respect to the global coordinate system.

D) A third matrix termed "Transformation matrix" was defined. This matrix was the cross product of two global matrix defined in step B.

E) Using the transformation matrix, the acceleration data from the sensor were rotated to the local bone coordinate system. Due to rigid body translation, angular rate data were not rotated but translated (Martin et al., 1998).

1.18.3.1.3 Translating the 6DX block origin to the local anatomical coordinate system origin.

After rotating the acceleration data from the sensor coordinate system to the bone coordinate system, both the acceleration and the angular rate data were transformed to the origin of the bone coordinate system. Each coordinate system is defined briefly in Table (4-8). The rigid body translation methodology described by (Rudd et al., 2006) was referenced for translating the data.

1.18.3.2 Miscellaneous Calculations

Next, the resultant values for both the acceleration and angular rate sensor were determined using the script written in Python. Furthermore, the relative rotation of the head with respect to the T1 spine and sacrum was calculated. First, the head angular velocity (anatomical Y axis) data with the center of gravity as the origin were integrated to obtain head rotation. Similarly, the T1 and Sacrum Y axis rotation data were obtained by integrating the angular velocity of the T1spine and sacrum, respectively. Last, the head Y rotation data were subtracted by the T1 and Sacrum Y rotation data to get the relative motion, respectively.

In addition to relative rotation, the spine axial compliance between the spine segments for the three axes was calculated. The acceleration data collected at the head and thoracic spine sensors were double integrated to obtain respective displacements. For this analysis, the head origin from center of gravity was shifted to the midpoint of the line joining the right and left Atlanto-occipital joints. The transformed head acceleration were translated to a new origin. The segment range for this analysis included the head/T1, T1/T5, T5/T8, T8/T12, and T12/S1. The displacement of the former segment relative to the latter for each axis was examined. For example, for the T1/T5 segment the T1 motion relative to T5 was evaluated. Spinal complaince data along the anatomical Z axis provided spine compression during vertical loading.

The last two parameters determined in the calculated staging were foot motion along the ankle and the shoulder motion relative to hip joint. Foot motion along the ankle was calculated by tracking the angle between a horizontal and vertical segment. The horizontal segment was formed by a line which connected the lateral epicondyle and lateral mallelous respectively, while the vertical segment consisted of a line joining the lateral mallelous to the toe marker. Using TEMA software, the angle between these segments was measured.

Shoulder motion relative to the hip joint center was determined using a combined approach which included CMM coordinate points, a local bone coordinate system, and video data. The following paragraph provides a detailed overview of the techniques used to determine shoulder kinematics.

Shoulder motion: The steps in evaluating the shoulder kinematics relative to the hip-joint center involves (1) defining the global coordinate system for the center of the hip joint relative to the seat at time =0, (2) normalizing the tracked acromion target motion data based on the test subject's height, and (3) determining the acromion target motion relative to the trochanter target marker using lateral video data.

<u>Defining global hip joint center coordinate system</u>

The hip center global coordinate system was defined in two steps. First, Using MIMICs Version 15 (Materialise, MI) a 2D mask was applied to the post-instrumented CT image of the femur head up to the level of the femur neck. Followed by masking, a 3D femur head model was extracted from the 2D mask. Next, the selected femur head was fitted with a sphere. The center of the sphere was defined as the local hip joint center coordinate system. Second, based on the local hip coordinate system and CMM coordinate points, the global coordinate system was determined. A pictorial representation of the procedure is shown in Figure 4-11. The lateral video data and the right side of the local ASIS coordinate system were considered for this analysis. The following protocol provides a brief overview for determining the global hip joint coordinate system.

A) The right hip joint center and the right ASIS local coordinate points were obtained from the pre-instrumentation CT data set
B) Both the x and z-axis distance between the ASIS and hip-joint center were determined from the pre-instrumentation CT data set
C) The distance between the ASIS to seatback and seat bottom to the ASIS were measured using CMM coordinate points
D) Generally, in the sitting position the ASIS point is superior and anterior relative to the hip joint (KEEGAN and Omaha, 1953; Schoberth and Hegemann, 1962). Therefore, the hip joint center global coordinate point was determined by the following equation:

   X-coordinate point = [x distance based on CT data (ASIS – hip joint center) – x distance based on CMM data (ASIS – seat back)]

   Z-coordinate point = [z distance based on CT data (ASIS – hip joint center) – z distance based on CMM data (ASIS – seat bottom)]

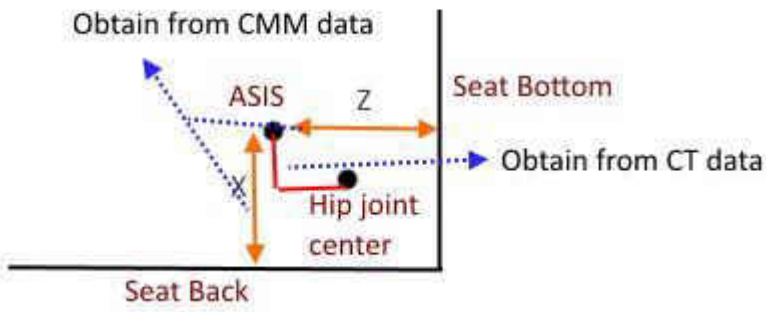

Figure 0-11: Summarizes the procedure followed to calcuate the hip-joint center.

After defining the global hip-joint center coordinate points, the tracked acromion marker displacement data were normalized based on the length. The methodolgy to determine the scale factor is described in Section 4.8.4.

Determining shoulder motion relative to hip joint center

First, the distance between the lateral camera lens and the horizontal seat system was determined. For the current study, the distance was measured to be 1.6 m. Second, the acromion and the trochanter target marker relative to the distance from the seat origin was calculated using CMM coordinate points. Third, all three target markers that tracked displacement from the processed staging were used to obtain 3D motion of these markers in the laborardoty coordinate system. Finally, the shoulder displacement relative to the hip joint center was calculated.

1.18.4 Scaled Staging

To eliminate variation in the test data due to differences in specimen anatomy, the calculated acceleration data were scaled to the 50th percentile army male using the equal stress equal velocity technique reported by (Eppinger et al., 1984). This method normalizes the response data of the test while maintaining the original loading velocity. The acceleration calculated data for each region were scaled based on the corresponding reference mass obtained from the ANSUR II pilot study (Paquette et al., 2009). The normalization factor λ was determined using the following equation:

$$\lambda m = \left(\frac{M\ ref}{Mi}\right)^{1/3}$$

Where λm – scale factor, M ref- mass of 50th percentile army male, M i – specimen segment mass

The test subject segment masses were measured using the "CT Image Based Mass Calculation Technique", which is discussed in the section (4.8.4.1). Assuming that the elastic modulus and mass density are the same between test subjects, the acceleration and time normalization equations are as follows:

$$\text{Acceleration: } A_a = \lambda m^{-1} A_b$$

$$\text{Time: } T_a = \lambda m\, T_b$$

Where subscript 'a' indicates normalized data and subscript 'b' indicates calculated sensor data.

In addition to acceleration data, the knee and shoulder motion processed data were also normalized. For both motion data, instead of mass ratio, length based normalization technique was used for determining λ parameter. The λ parameter for the knee and shoulder were calculated using the femur length and specimen stature height respectively. The reference length were obtained from the ANSUR II pilot study (Paquette et al., 2009).The length scale factor was determined using the following equation:

$$\lambda l = \left(\frac{L\ ref}{L\ i}\right)$$

Where λ l – scale factor, L ref- length of mass of 50th percentile army male, M i – specimen length

The specimen stature height and the femur length were obtained from the anthropometry measurement. The length and time normalization equations are as follows:

$$\text{Length: } L_a = \lambda l \, L_b$$

$$\text{Time: } T_a = \lambda l \, T_b$$

Where subscript 'a' indicates the normalized data and subscript 'b' indicates the processed kinematic data obtained by tracking the specified target marker on the specimen. The scale factor for both tests are shown in Appendix C

1.18.4.1 CT Image Based Mass Calculation Technique

Acceleration response data are one of the key measurements in the evaluation of biomechanical response due to UBB loading. In general, acceleration is inversely proportional to mass. Therefore, more mass will attenuate the acceleration impulse transmitted to the body during the impact. Thus, to understand the load distribution through each body region, each segment of mass must be calculated separately. The segmentation plane discussed by McConville at al. was referenced to identify the planes for segmenting each anatomical component (McConville et al., 1980). The following is a brief overview of the anatomical plane implemented for segmentation.

- Head – a plane through the Atlanto-occipital joint that extends along the inferior border of the mandible.
- Knee plane – a transverse plane inferior to the patella that passes through the femoral-tibia joint with the leg extended.

- Hip plane- the segmentation plane at the hip which starts above the femur head and extends obliquely along the acetabulum rim.

Pre-instrumentation CT scans were used for measuring the segment mass. If the subjects were not positioned ideally on the CT table during the scanning, the orientation of the segmentation planes was affected. Therefore, after segmenting the component, the unwanted segment regions or debris were removed. The protocol to measure segment mass from CT was referenced from (Heymsfield et al., 1979). The tissue threshold levels and the segmented mass calculation procedure are described as follows:

Threshold: MIMICs Version 15 (Materialise, MI) was used for measuring the segment mass. The WIAMan Scaling Working Group recommended that the Hounsfield unit values for the soft tissues fall in the range of 524 to 1579 HU, while the bone Hounsfield units should measure above 1579 HU. However, in MIMICs the Dicom translation uses (-1023 HU) as the minimum threshold value. Thus, to get a similar threshold value in MIMICs, 1023 HU were subtracted from the recommended threshold values. The program recommended and the MIMICs calculated threshold value for the bone and the soft tissue are reported in Table 4-9.

Table 0-9: Threshold value used for CT mass measurement.

	Threshold HU	
	Soft tissue range	Bone range
WIAMan program recommended	$524 \leq T \leq 1579$	$1579 \leq T$
MIMICs calculated	$-499 \leq T \leq 556$	$556 \leq T$

Mass measurement protocol:

A) CT Dicom images were read into MIMIC software

B) Bone and soft tissue threshold values were set

C) Based on the threshold value, separate 2D masks were created for bone and soft tissue for the desired anatomical regions.

D) Unwanted tissue regions were removed using the edit mask option

E) A 3D model was created using the property option

F) The default volume for the 3D model was set to cm^3

G) The segment mass was predicted as a product of calculated volume and the pre-defined tissue density (Bone = 1 g/cm^3 and Soft tissue = 1.92 g/cm^3).

With the normalizing of accelereation and the knee and shoulder motion data, the data processing for the vertical testing came to an end. Appendix B provides a summary of the data processing performed in each stages.

For each stage, a separate readme (.txt file) was created, which included the channel processed in that stage, engineering units, sensor ID and the corresponding filter used. These readme files give a brief overview of each stage. Followed by data processing, the data from all the stages were plotted using DIADEM software to analysis and check the quality of the processed data. The response data with the indication of fracture were excluded from further analysis and were labeled as bad channels in the corresponding (.TVS format) channel file and in the readme file of all the stages.

CHAPTER 5

CADAVER IMPACT RESPONSE

The following is a summary of the PMHS responses and the corresponding injuries that occurred in the two reported tests. The relevant anthropometric measurements for each specimen are tabulated in Appendix A. The CT and the pathologist's findings are confirmed and documented with photography and radiology images. The representative CT and autopsy images of the injuries for each specimen are shown in Figures 5-1 and 5-2, respectively.

WSU-003 Autopsy and Radiology Summary (Specimen No-OSU 6908)

Pre-existing Injuries

- Diffuse arthritic findings with bridging osteophytes at C4/C5 and C6/C7

Post-test Injuries

- Impaction fracture of L1

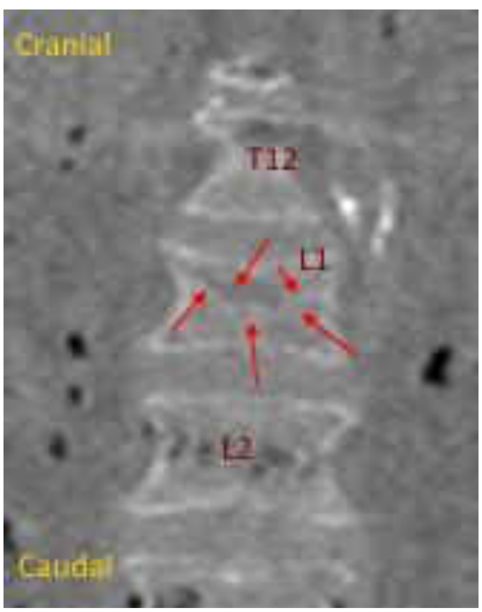

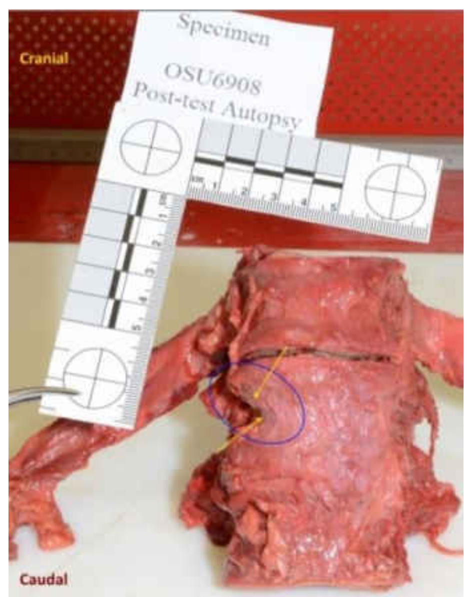

Figure 2-1: Illustration of the CT and autopsy demonstrating the impaction fracture of the L1 spine sustained by the OSU 6908 specimen. The test subject was impacted at a seat velocity of 4m/s with 10ms time to peak.

WSU-004 Autopsy and Radiology Summery (Specimen No- LMD 14-00355)

Pre-existing Injuries

- Left nasal bone fracture
- 12 cm cavitary mass in the left hemithorax

Post-test Injuries

- Compression fracture of L3 (mild)

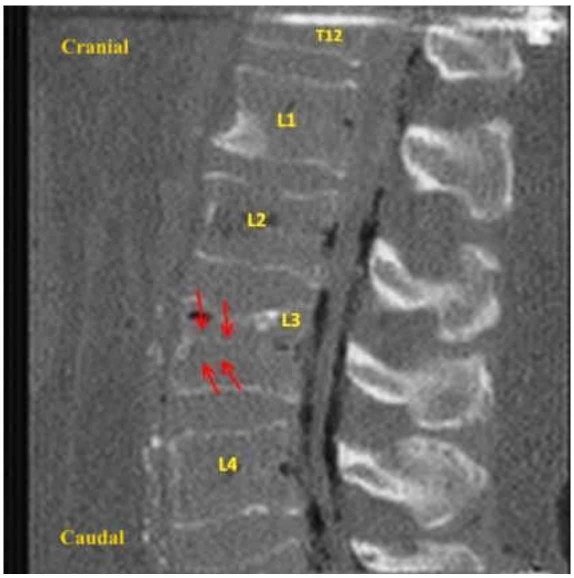

Figure 2-2: Illustration of the CT demonstrating the compression fracture of the L3 spine sustained by the LMD 14-00355 specimen. This test subject was also impacted at a seat velocity of 4m/s with 10ms time to peak.

2.1 Impact Response

The biomechanical responses were measured in terms of acceleration and angular velocity using the 6DX motion block mounted to the desired anatomical regions. The resultant acceleration and integrated angular velocity data were used to analyze the impact responses of each region instrumented with transducers. For the current study, the normalized linear acceleration X and Z were used for calculating the resultant, while angular velocity measured around the anatomical Y axis was considered for determining the rotation. These data channels were the primary response parameters. Table 5-1 presents the peak acceleration and velocity for each anatomical region and for each test. The peak velocity data is useful from the injury response perspective as the human tissue exhibits a velocity-dependent nature (Nordin and Frankel, 2001). The impact response of each body part from the foot to the head is addressed separately in the following section.

Table 2-1: A Summary of the Peak Acceleration and the Corresponding Peak Velocity for Each Test.

	WSU-003		WSU-004	
	Peak Acceleration (g)	Peak Velocity (m/s)	Peak Acceleration (g)	Peak Velocity (m/s)
Floor	230	6.31	240	6.13
Right Calcaneus	NA	NA	NA	NA
Left Calcaneus	182.1	5.77	224.1	4.51
Left Tibia	164.6	6.52	175.8	6.26
Right Tibia	132.4	6.01	177.3	5.86
Left Femur	86.0	4.30	73.8	5.50
Right Femur	94.7	4.35	94.2	5.49
Seat	128.9	4.72	139	4.48
Sacrum	67.1	2.17	33.18	1.27
T12	152.0	3.78	112.2	4.23
T8	181.1	3.24	80.09	3.81
T5	146.4	2.92	77.7	4.41
T1	42.1	1.46	59.8	3.79
Sternum	23.7	4.36	24.9	4.86
Head	16.9	2.37	21.4	4.41

Lower extremity: Neither specimen sustained a lower extremity injury. The lower extremity data were evaluated in two ways: First, the response data measured from the right leg was compared to the left leg measurement for each test (Inter-analysis). Next, the data were compared between the tests (Intra-analysis). The lower extremity biomechanical response in terms of foot linear Z acceleration, tibia XZ resultant and Z linear acceleration, femur XZ resultant and Z linear acceleration, and tibia and femur Y rotation were measured for the current study. The representative Z linear, XZ resultant acceleration and Y rotation data for each region are shown in Figures 5-3 through 5-9.

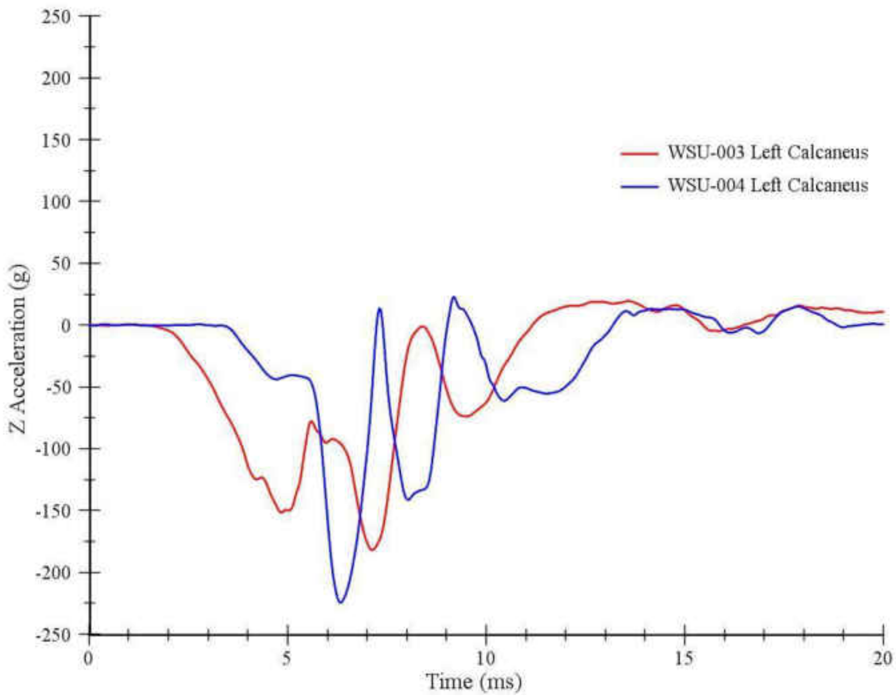

Figure 2-3: Calcaneus Z Linear Acceleration

The right calcaneus Z linear acceleration data for the WSU-003 test subject was missing due to a sensor failure. Also, for the WSU-004 test subject, the right calcaneus mount popped off the bone surface during the post-impact inspection. Since the right foot acceleration data were missing, the foot acceleration inter-analysis was not preformed. It can be observed from Table 5-1 that the WSU-003 test subject had a maximum foot response of 182 g's, while the WSU-004 test subject had a peak response of 225 g's. Additionally, the area under the acceleration curve for the WSU-003 test subject was higher, as shown in Figure 5-3. This indicates that more kinetic energy was transmitted to the foot of the WSU-003 test subject.

In conjunction with the foot, the tibia receives the floor load. In this study, the motion sensor was mounted at the distal tibia region on each of the lower legs. The inter-analysis for the WSU-003 tibia data shows that the left tibia experienced a peak response of 164 g's, while the right tibia experienced response of 131 g's (Figure 5-4). For the WSU-004 test subject, the left tibia received a maximum acceleration of 175 g's, while the right tibia received 177 g's. Furthermore, both tibias of the WSU-003 test subject had a similar resultant acceleration profile, as shown in Figure 5-5.

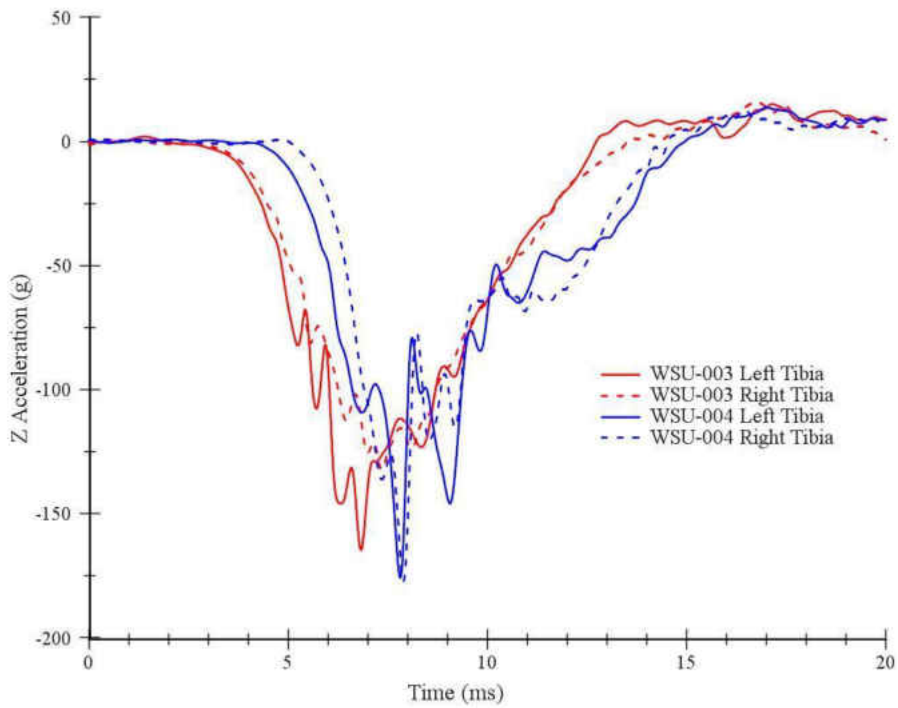

Figure 2-4: Tibia Z Linear Acceleration

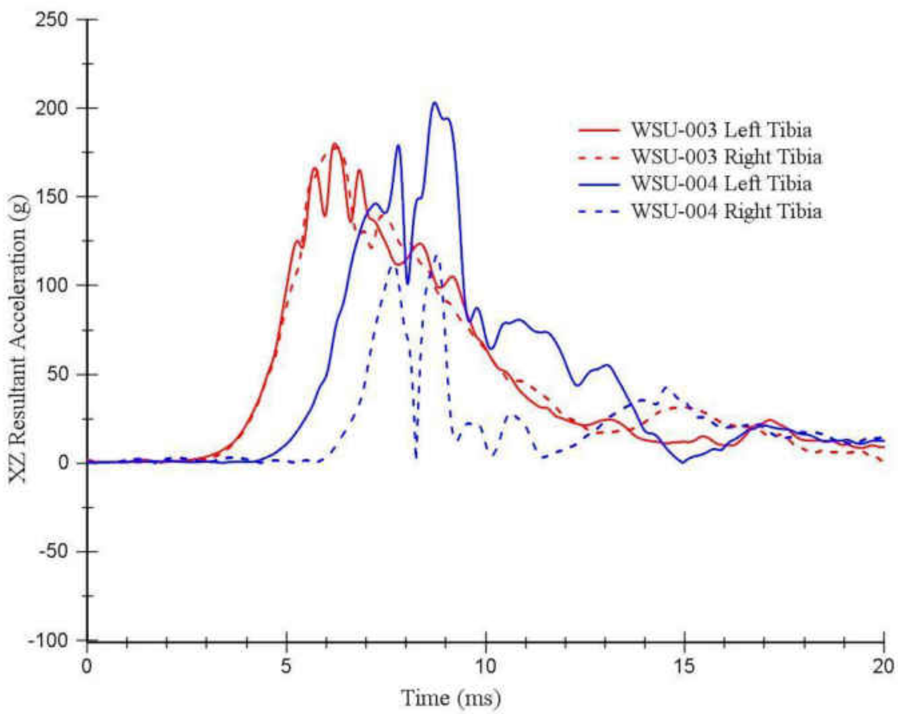

Figure 2-5: Tibia XZ Resultant Acceleration

This observation indicates that although the right tibia Z acceleration was lower compared to its counterpart, the acceleration along the X axis contributed to higher XZ resultant acceleration. A possible reason could be the orientation of the motion block relative to the bone at the right tibia, which could have influenced the response measurement. The WSU-004 XZ resultant acceleration curve in Figure 5-5 reveals that the right tibia experienced a negative acceleration along the X axis, which resulted for a lower XZ resultant response relative to that of the left tibia.

Next, the intra-analysis between the tests shows that the WSU-004 tibia had 1.3 ms delay in the response compared to that of the WSU-003 tibia data. The WSU-004 foot plate acceleration time of arrival lagged 0.96 ms relative to the WSU-003 foot plate arrival time (Table 5-1). This delay in the foot plate data explains the reason for the delay in the response between the tests.

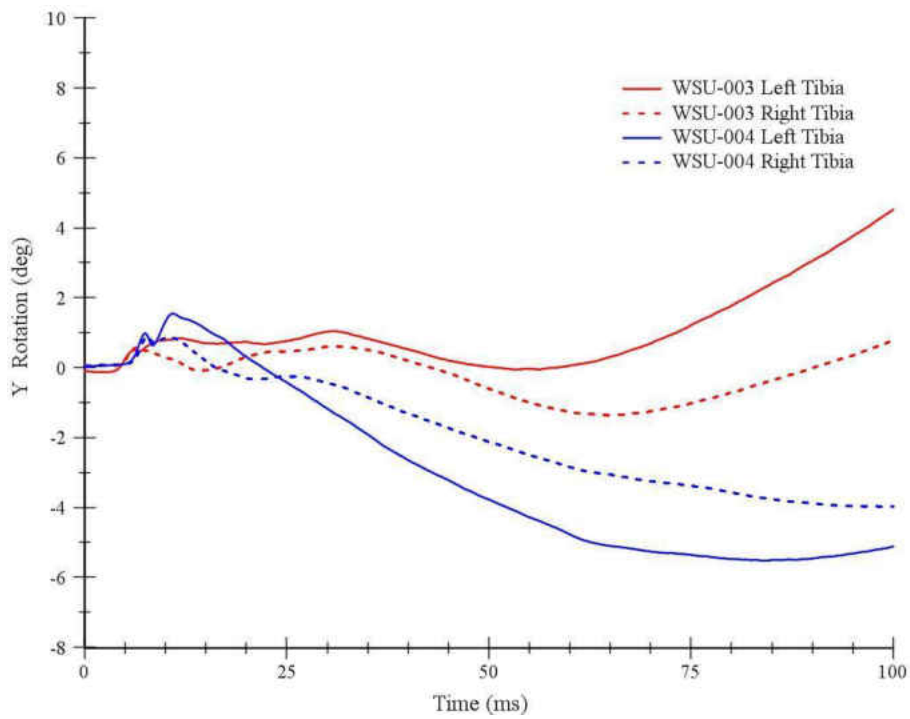

Figure 2-6: Tibia Y Rotation

In addition, the rotation data provides the orientation of the tibia during the event. The rotation around the Y axis for each test and for each tibia is shown in Figure 5-6. Up until 20 ms the tibia in both tests had a minimal rotation of 1- 2 degrees around the Y axis. Afterward, it can be observed from Figure 5-6 that the tibias in the WSU-003 test undergo flexion, while the WSU-004 tibias undergo extension. The potential reason could be the orientation of the sensor mounted on the tibias in both tests.

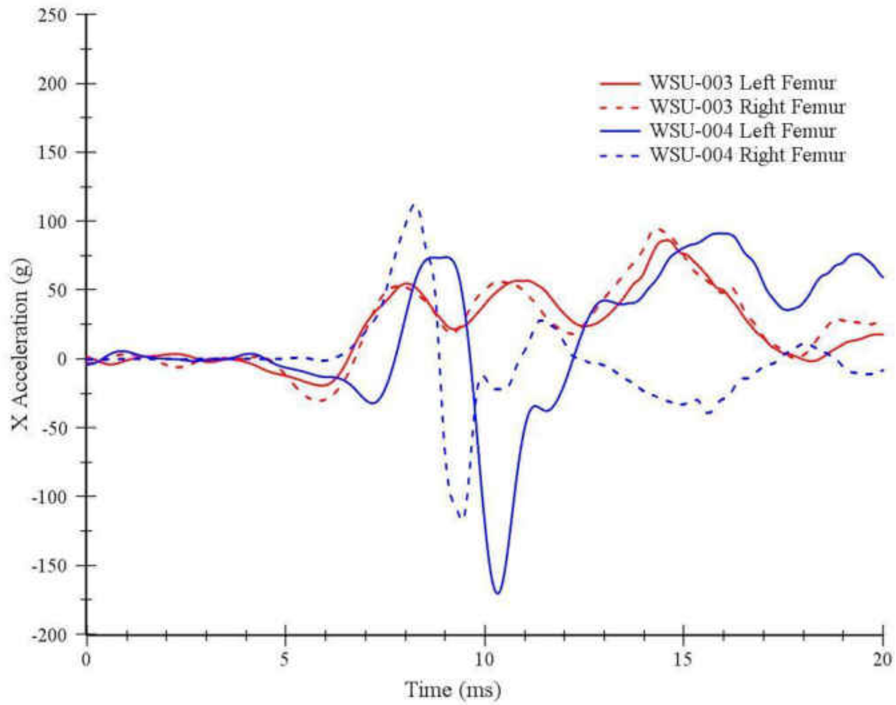

Figure 2-7: Femur X Linear Acceleration

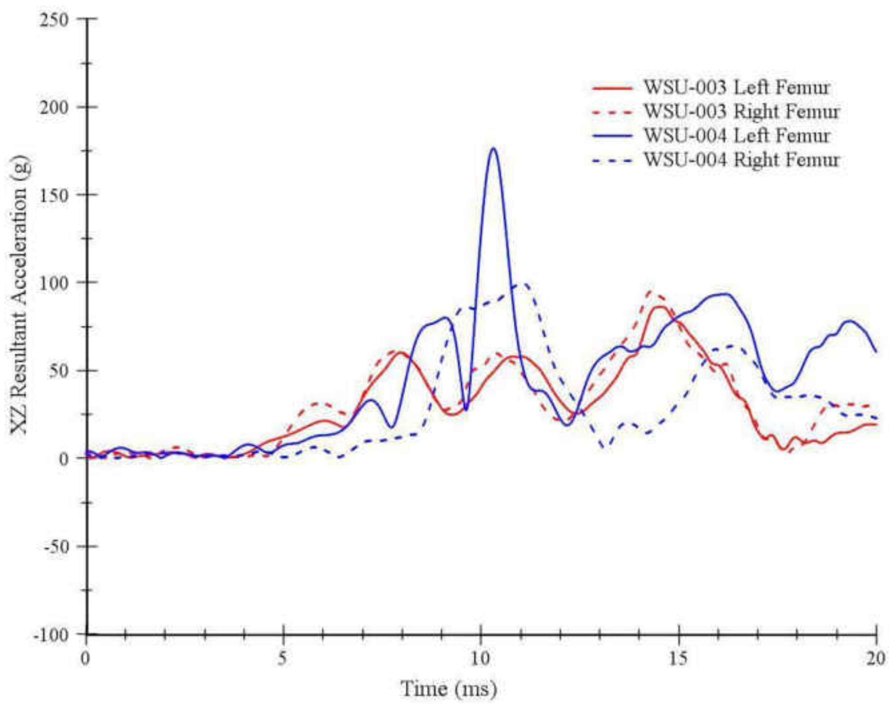

Figure 2-8: Femur XZ Resultant Acceleration

After the tibia, the floor load is transmitted to the femur. The inter-analysis for the WSU-003 test subject shows that the right femur experienced a maximum response of 56.15 g's, while the left femur experienced 56.76 g's. In the WSU-004 test subject, the right femur received a peak acceleration of 94.21 g's, while the left femur received 73.52 g's. The resultant acceleration curve in Figure 5-8 indicates that in both tests the Z linear acceleration had minimal influence on the femur response.

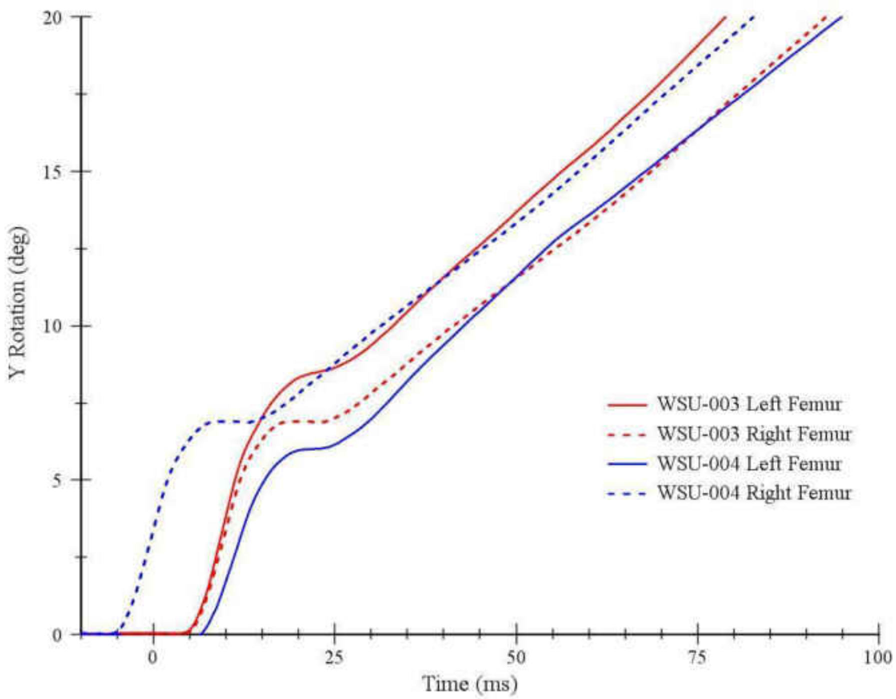

Figure 2-9: Femur Y Rotation

The femur rotation curve in Figure 5-9 reveals that the tibias in both tests flexes outwards around the Y axis producing extension at the knee. Moreover, the femur seemed to pause after having a rotation of 7 to 8 degrees for 3 to 5 ms, followed by further rotation in the same direction. The initial rotation was due to the effect of the floor load, while the latter rotated because of the pelvis rotation in flexion around the Y axis. Furthermore, upon impact, the pelvis inertia forced the pelvis to ride on the seat bottom and then rotate around the Y axis. This initial motion of the pelvis on the seat bottom could have caused the plateau phase, seen in Figure 5-9.

Pelvis: Neither of the specimens sustained pelvis injury; the pelvis was intact post impact for both test subjects. Figures 5-10 and 5-11 represent the pelvis linear Z and resultant XZ acceleration for both tests. The WSU-003 sacrum had a maximum Z acceleration of 67 g's, while the WSU-004 sacrum had an acceleration of 33.18 g's. A sudden positive spike at 21 ms for the WSU-003 test subject and at 15 ms for the WSU-004 test subject (Figure 5-10) could have been caused by an associated fracture in the spine. Both test subjects sustained a lumbar fracture. After the occurrence of the fracture, the torso loading resulted in a positive spike as mentioned above.

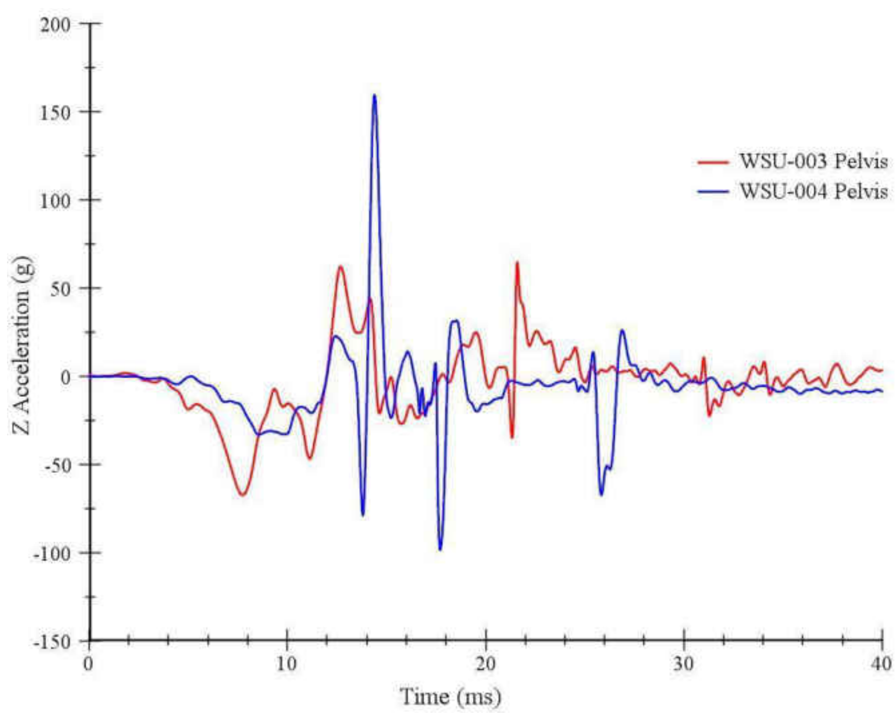

Figure 2-10: Sacrum Z Linear Acceleration

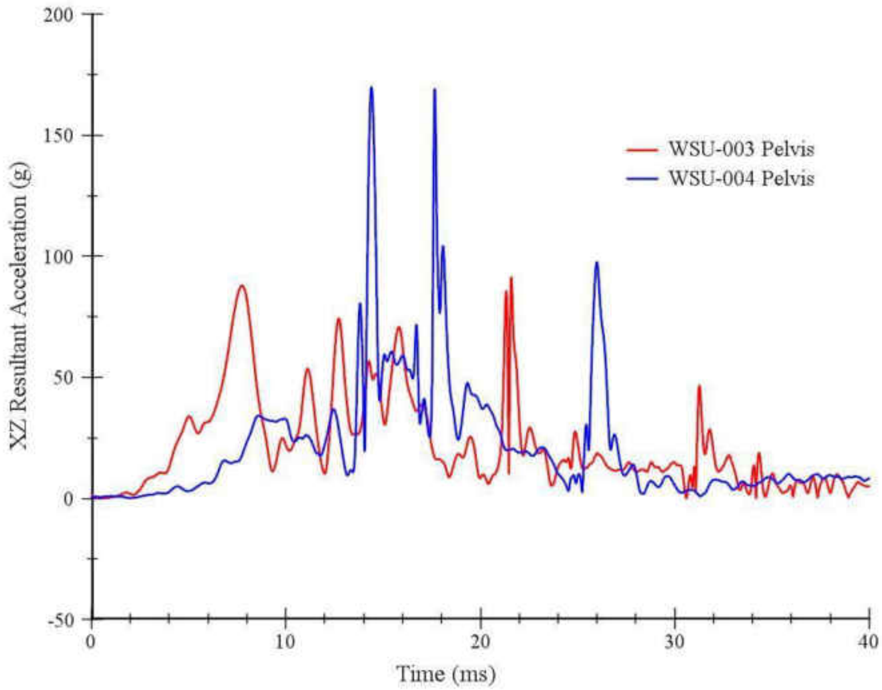

Figure 2-11: Sacrum XZ Resultant Acceleration

The XZ resultant data in Figure 5-11 indicates that the X linear acceleration influenced the pelvis impact response. The orientation of the 6DX motion sensor mounted to the sacrum could have caused the sensor to measure a higher peak response in the X direction. In the current test setup, the sacrum sensor was mounted to the S1 spine such that the sensor axis aligned with the anatomical coordinate axis. During specimen positioning on the sled prior to the impact, the pelvis was rotated to make an angle of 45° relative to seat back. In this position, the sensor was not aligned with the sled co-ordinate system. Therefore, the orientation of the sacrum motion block caused the sensor to measure a higher magnitude response in the X direction. The comparison of pelvis angle between the tests and corresponding peak response measured at the sacrum and T12 vertebrae (Table 5-2) indicates that the pelvis angle could have potentially influenced the sacrum and T12 impact response. Further investigation needs to be conducted to analysis this hypothesis.

Table 2-2: Comparison of the WSU-003 and WSU-004 measured pelvis and corresponding peak response experienced by the sacrum and T12 vertebrae, respectively.

Test no	Pelvis angle (degree)	Pelvis peak Z acceleration (g's)	Pelvis peak XZ resultant acceleration (g's)	T12 peak Z acceleration (g's)
WSU-003	41.18	67.10	99.10	151.5
WSU-004	46.33	33.18	39.05	112.23

Next, since the pelvis directly interfaces with the loading surface, it is essential to analyze the orientation of the pelvis during the event. Therefore, in addition to the rotation around the Y axis, the rotation data along the X and Z axes were also determined. The rotation curves in Figures 5-12 through 5-14 illustrate that the rotation around X and Z were minimal, accounting for $\pm 2^{\circ}$ - 3° rotation, while around the Y axis, the pelvis had a rotation of 12° and 20° for the WSU-003 and WSU-004 test subjects respectively. Further rotation was restrained by the lap belt. The positive rotation of the pelvis along the Y axis demonstrates that the pelvis rotates and tends to flex towards the torso. This motion of the pelvis also accelerates the femur towards the torso.

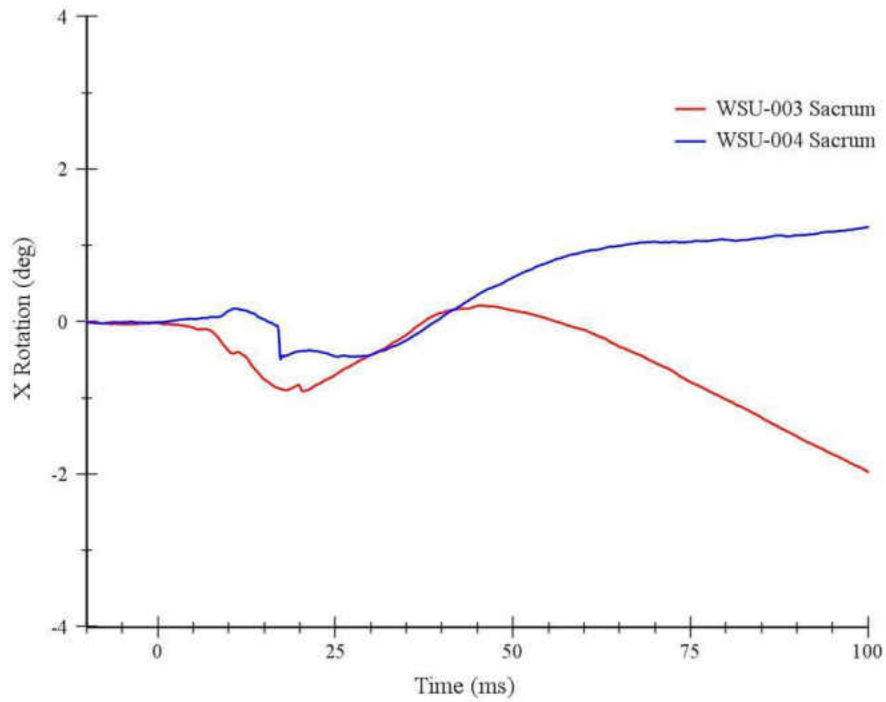

Figure 2-12: Sacrum X Rotation

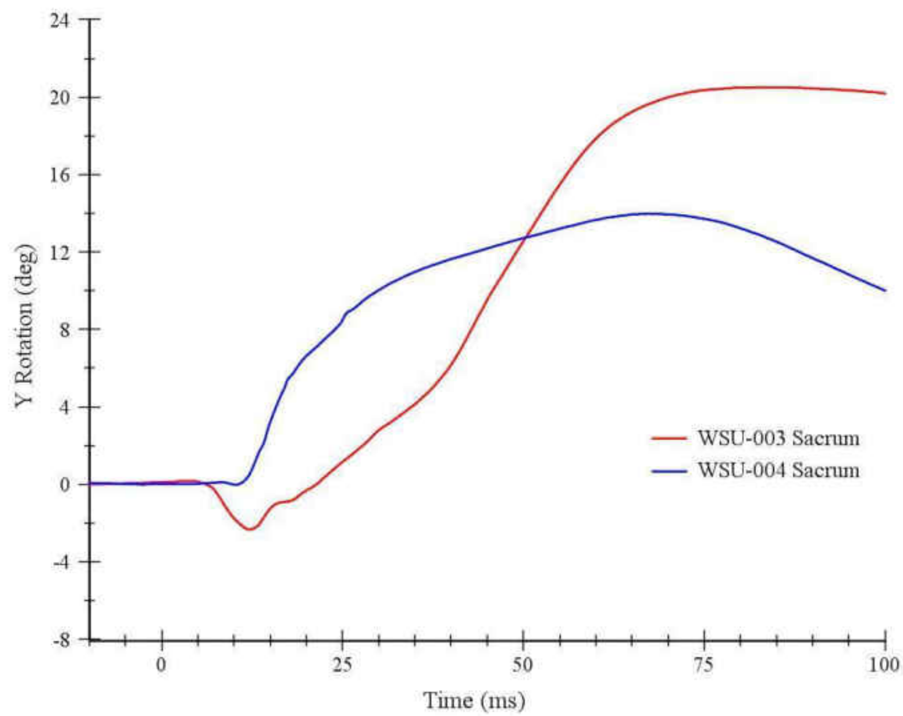

Figure 2-13: Sacrum Y Rotation

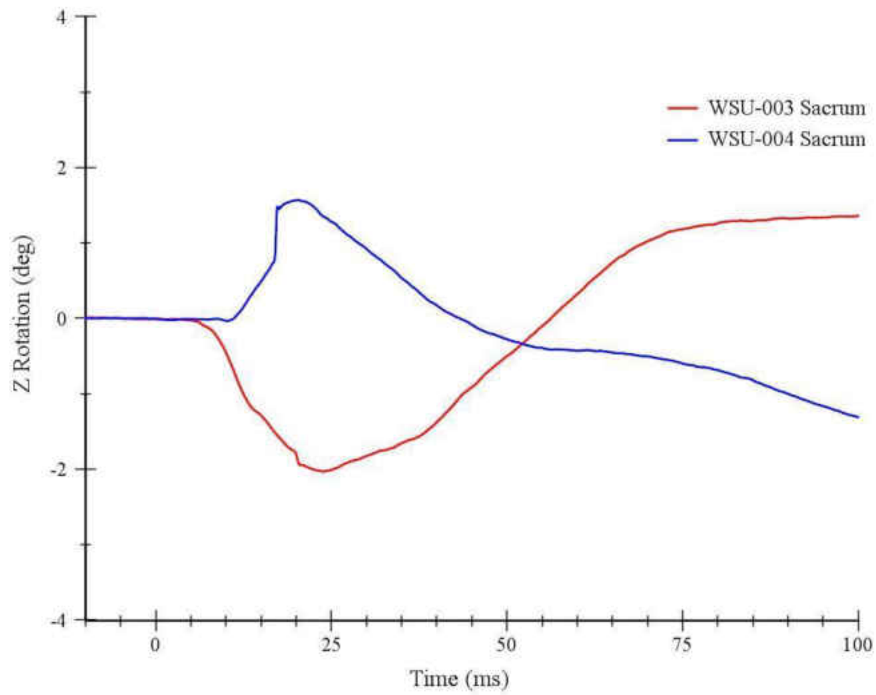

Figure 2-14: Sacrum Z Rotation

Spine: Both test subjects sustained a lumbar fracture. The WUS-003 test subject had an impaction fracture at L1, while the WSU-004 test subject had a L3 compression fracture. The spine response was measured using four transducers mounted to the thoracic vertebrae, which included T1, T5, T8 and T12. The Z linear and XZ resultant acceleration for each subject are separated by the individual spine region and shown in Figures 5-15 through 5-23. The response data from the spine sensors were used to investigate the injury mechanism.

Next to the sacrum, the transducer mounted to the T12 vertebra measures the acceleration transmitted cranially upward due to the seat impact. The WSU-003 T12 sensor measured a peak Z acceleration of 152 g's, while the WSU-004 T12 sensor measured 112 g's (Figure 5-15). It can be observed from Table 5-1 that in the WSU-003 test subject the T12 spine had a higher peak response compared to that of the sacrum. A similar response pattern was also noticed in the WSU-004 test subject as well. The potential reason for a higher response at the T12 spine could be due to the orientation of the pelvis relative to the seat back. In order to achieve a 45° angle between the pelvis and seat back, the pelvis is tilted and positioned on a foam block. This orientation of the pelvis causes the T12 sensor to be aligned with the primary loading direction more than the sacrum. Hence, the T12 sensor measures a higher peak Z acceleration compared to the sacrum. Furthermore, the T12 spine in WSU-004 measures a positive peak around 25 ms, which could be the result of the inertial loading of the torso followed by a compression fracture at the third lumbar vertebrae. The T12 spine XZ resultant acceleration curve in Figure 5-16 indicates that in both tests the T12 spine response was predominately due to linear Z acceleration.

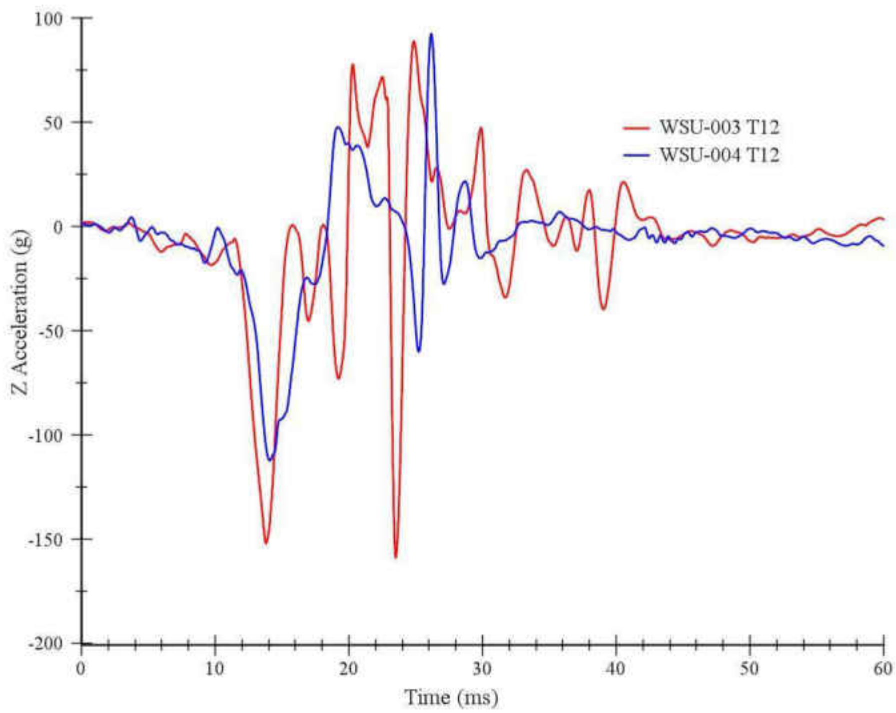

Figure 2-15: T12 Spine Z Linear Acceleration

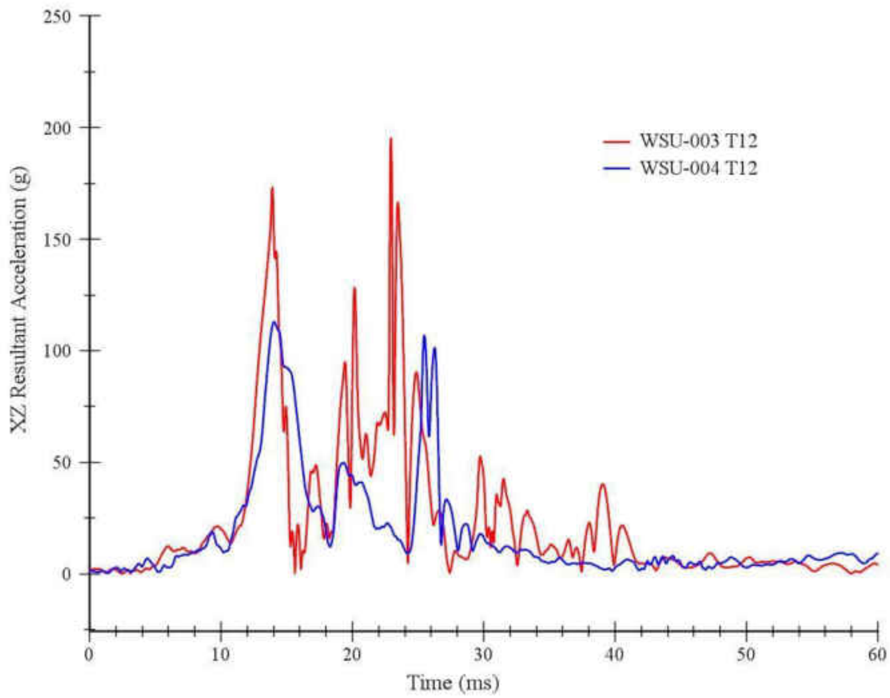

Figure 2-16: T12 Spine XZ Resultant Acceleration

Followed by the T12 sensor, the 6DX motion block installed at the T8 vertebrae measured the impact for load. The WSU-003 T8 spine sustained a maximum response of 181 g's, while the WSU-004 T8 spine sustained 80 g's. Furthermore, the T8 spine sensor measured a positive peak at 15 ms, which could have resulted due to an associated fracture at L1. Likewise, the influences of the L3 compression fracture were also observed in the WSU-004 T8 spine Z acceleration curve at 25 ms (Figure 5-17). Similar to the T12 resultant acceleration data, the T8 spine XZ resultant response was predominately caused by linear Z acceleration (Figure 5-18) for both tests.

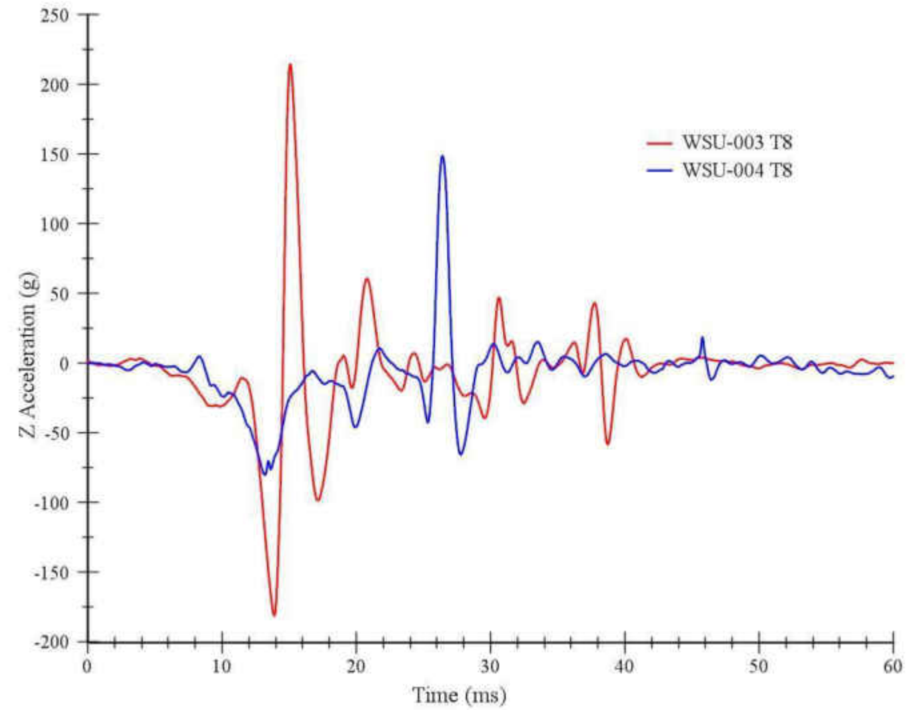

Figure 2-17: T8 Spine Z Linear Acceleration

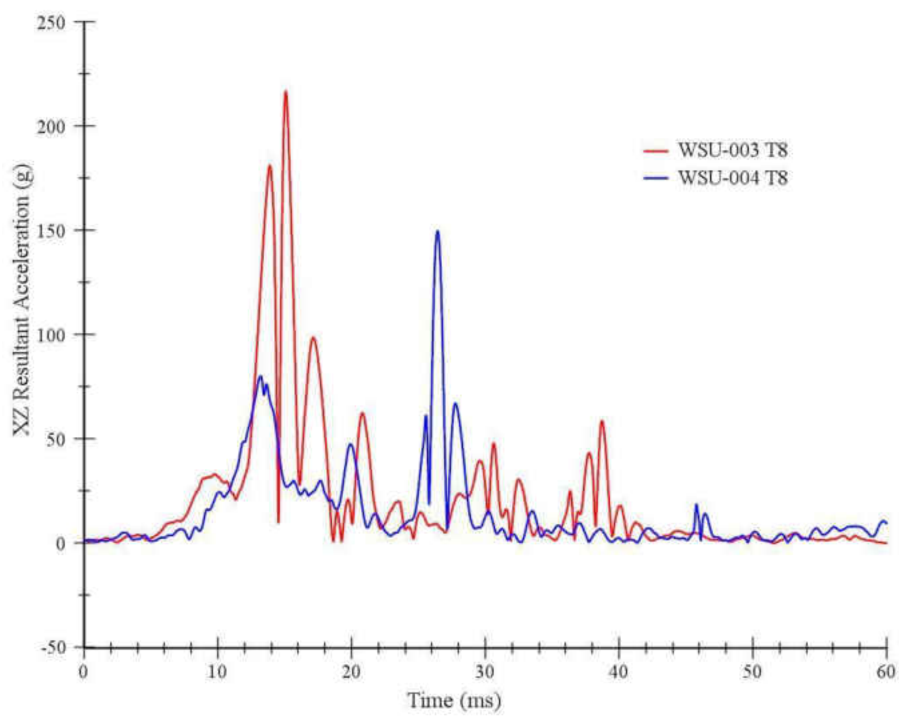

Figure 2-18: T8 Spine XZ Resultant Acceleration

After the T8 spine, the T5 spine was equipped with a 6DX sensor. The WSU-003 T5 spine had a maximum response of 146 g's, while the T5 spine of WSU-004 had a response of 77 g's. The influence of the fracture at the lumbar region was also noted in the T5 Z acceleration curves (Figure 5-19) for both tests. The resultant acceleration data in Figure 5-20 reveals the same conclusion as the previous resultant data and shows that the Z linear acceleration contributed to the T5 impact response.

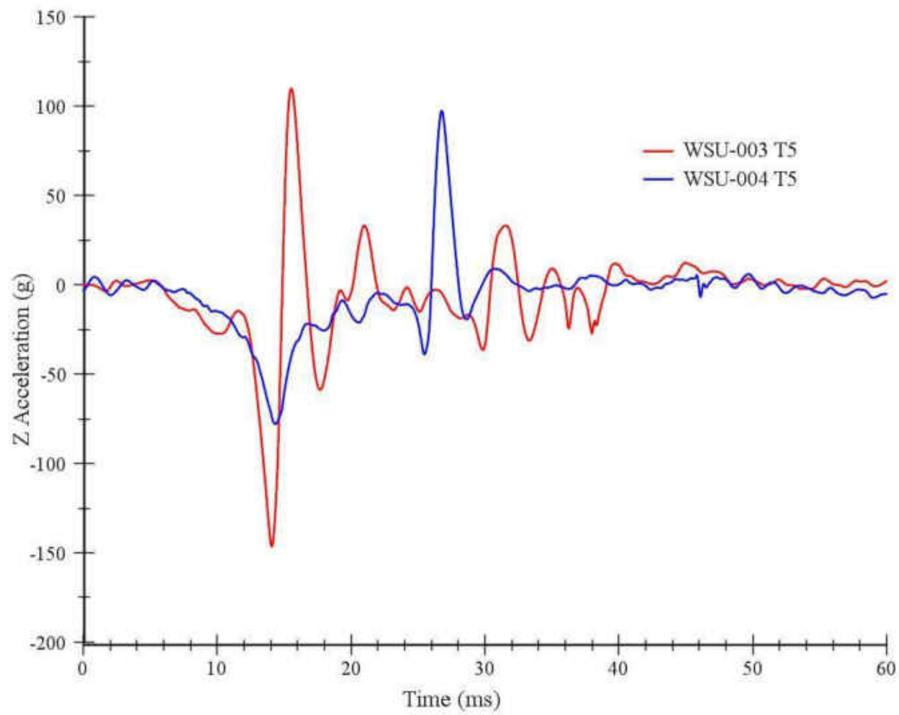

Figure 2-19: T5 Spine Z Linear Acceleration

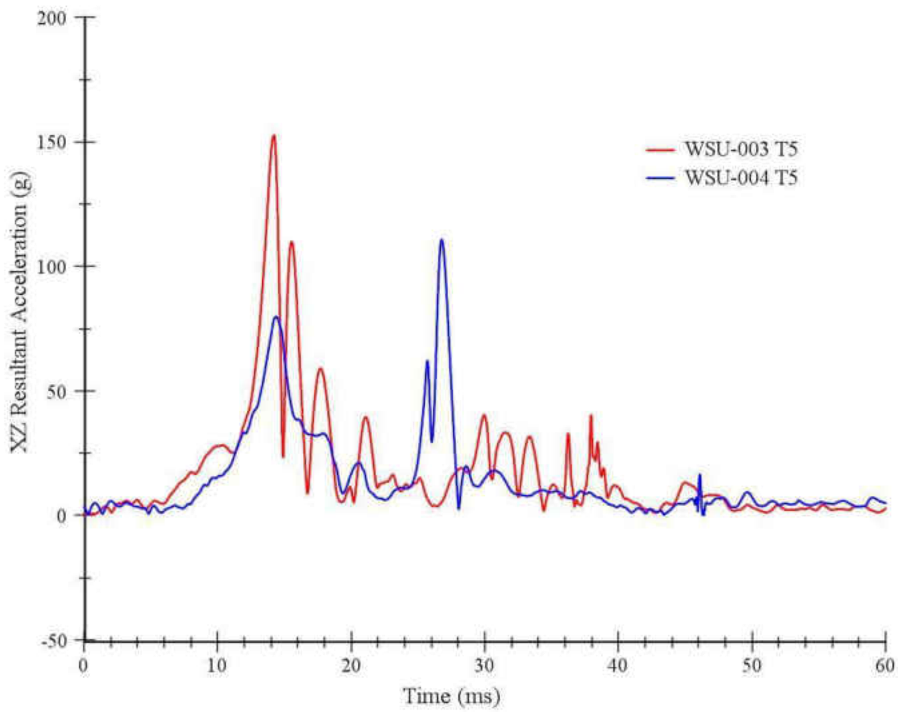

Figure 2-20: T5 Spine XZ Resultant Acceleration

Finally, the T1 spine was equipped with a 6DX motion sensor. The WSU-003 T1 spine measured a peak acceleration of 42 g's, while the WSU-004 T1 spine measured a peak acceleration of 59 g's (Figure 5-21). It can be observed from the T5 and T1 spine peak response data in Table 5-1 that the load measured by the T1 sensor was 55% less compared to the T5 sensor measurement in WSU-003. On the contrary, in WSU-004 the T1 peak response was 13% less compared to the T5 peak response. The possible reason for lower response at T1 for WSU-003 test subject could be due to the orientation of the T1 spine relative to the T5 spine during the flexion of the upper torso.

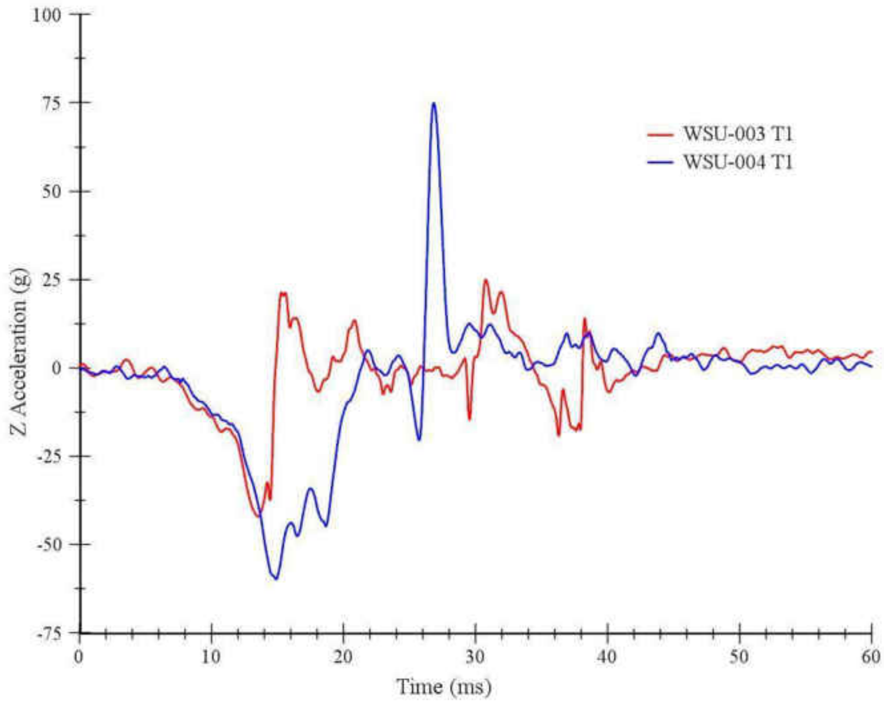

Figure 2-21: T1 Spine Z Linear Acceleration

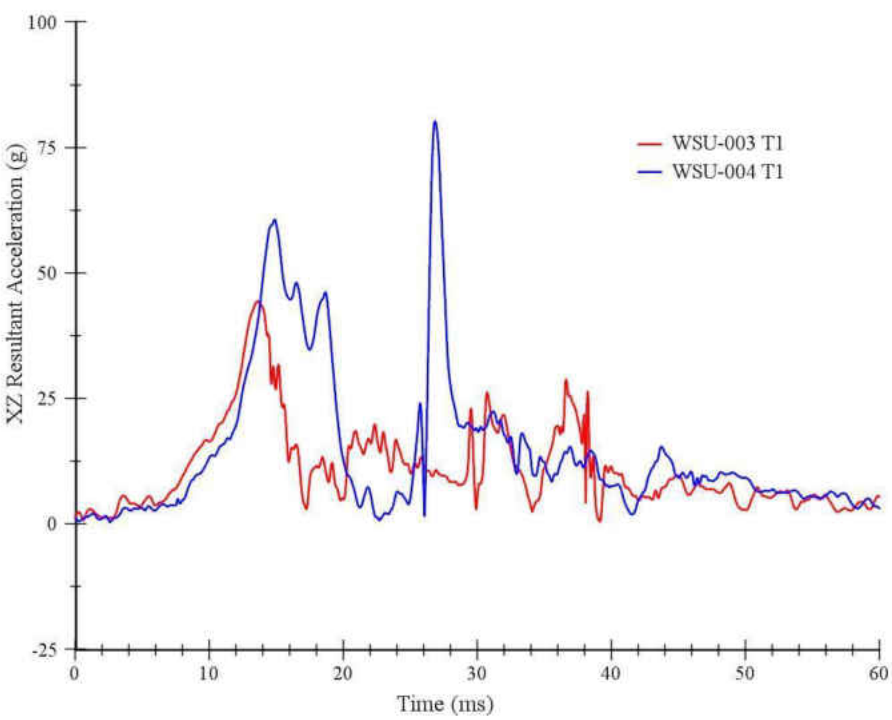

Figure 2-22: T1 Spine XZ Resultant Acceleration

In addition to acceleration data, the spine rotation data provides the local kinematics of the spine during the event. Figure 5-23 summarizes the Y rotation data experienced by each individual spine and for each test. In the WSU-003 test subject, only the T12 spine had a maximum rotation of 6°, while the rest had less than a 2° rotation around the Y axis respectively. However, in the WSU-004 test, the spine rotation around the Y-axis increased cranially with T1 having the maximum rotation of 12°.

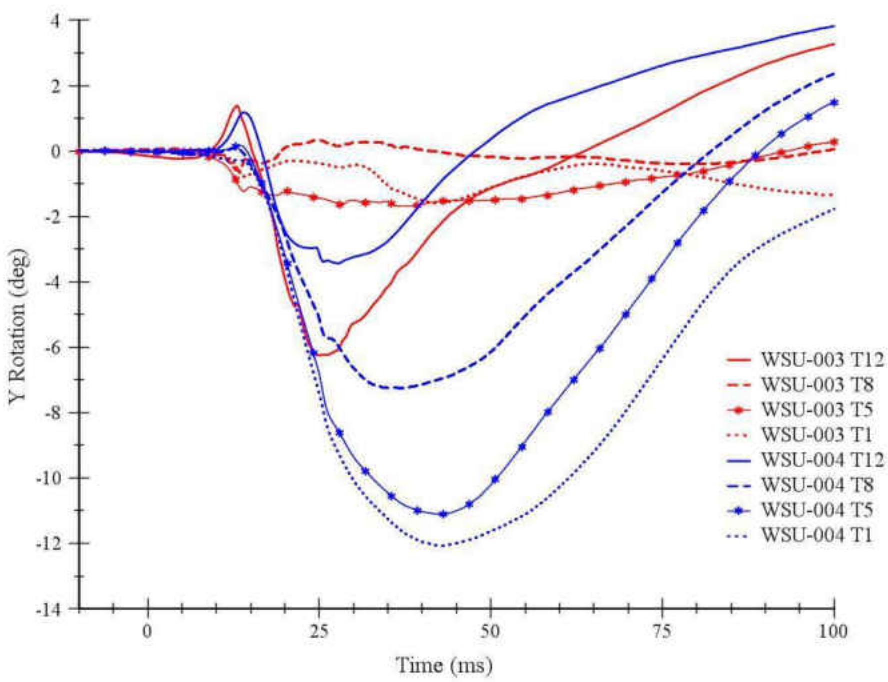

Figure 2-23: Thoracic Spine Y Rotation

As mentioned in the autopsy and radiography reports, both test subjects sustained a lumbar fracture. The WSU-003 test subject had an impaction fracture at L1, while WSU-004 had a L3 compression fracture. The timing of these injuries can be predicated by analyzing the thoracic spine response. The representative thoracic acceleration response curves are shown in Figures 5-25 and 5-26 for each test separately. A negative spike at 22 ms in the T12 Z acceleration curve seen in Figure 5-24 indicates the possible timing of the L1 impaction fracture. Furthermore, the

WSU-003 subject's lumbar spine DEXA scan shows that the L1 vertebral body bone mineral density falls in the osteopenia range with a T-score of -1.4 (described in section 4.4). The low bone mineral density level increases the risk of fracture. Next, the positive spike in the thoracic spine acceleration at 25 ms could be the possible timing for the L3 compression fracture as shown in Figure 5-25.

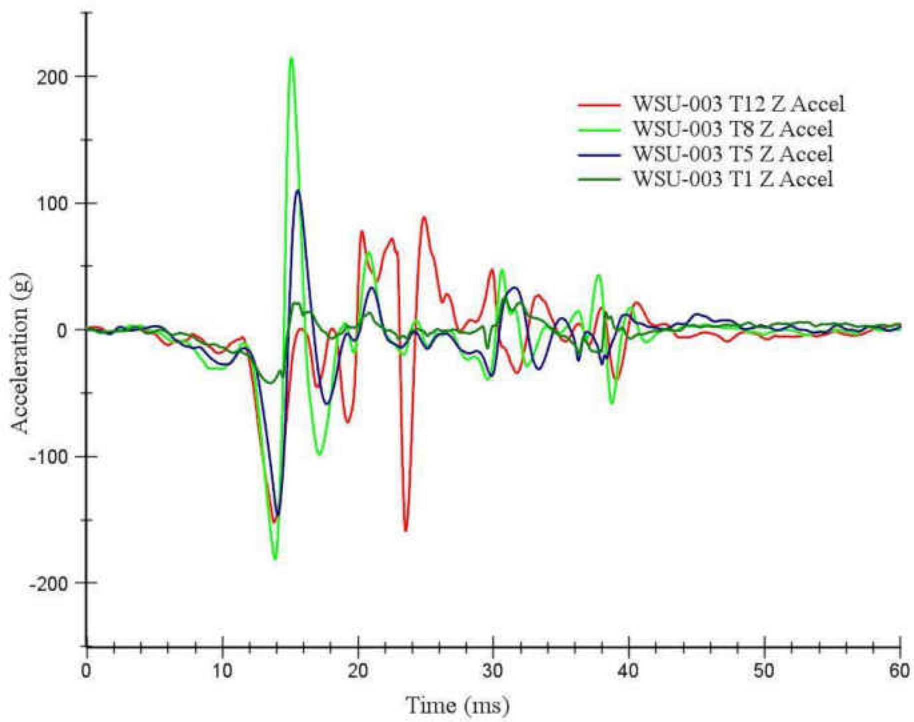

Figure 2-24: WSU-003 Spine Z Linear Acceleration.

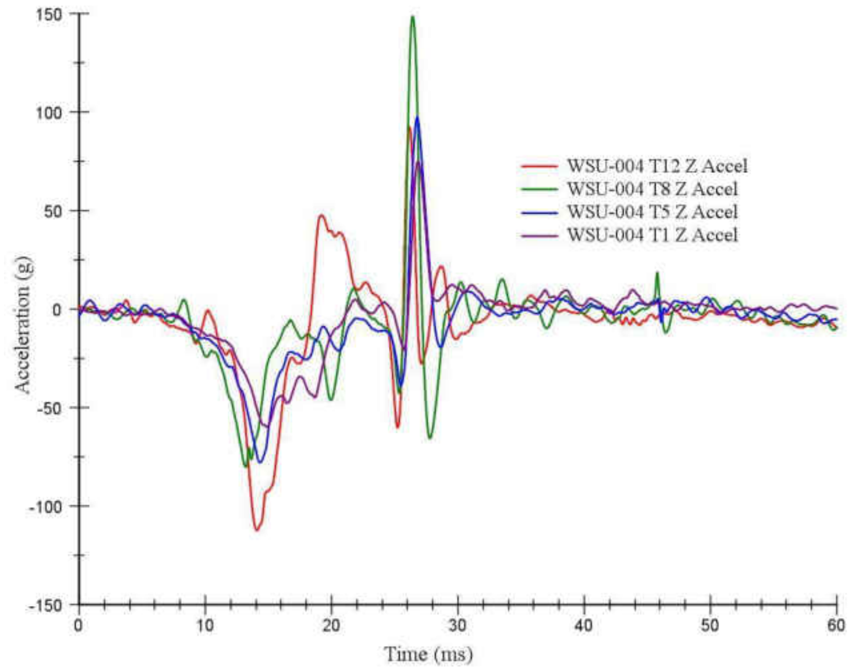

Figure 2-25: WSU-004 Spine Z Linear Acceleration.

Sternum: Figure 5-26 shows the sternum Z linear acceleration curve for both tests. The WSU-003 sternum received a maximum response of 23 g's while the WSU-004 sternum received a response of 24 g's. In addition, the WSU-004 sternum acceleration curve shows a positive peak of 175 g's at around 40ms. The CT scan of WSU-004's thorax showed a 12 cm cavitary mass in the left hemi-thorax region. Furthermore, in Figure 5-23 the spine rotation data for the WSU-004 test subject shows that the T1 spine had a maximum rotation at approximately 40ms. Therefore, the flexion of the torso and the presence of the cavitary mass could have resulted in a discrepancy in the sternum response at 40ms. The XZ resultant acceleration curve in Figure 5-27 indicates that the acceleration around the X axis was minimal and the sternum impact response was predominately caused by Z linear acceleration.

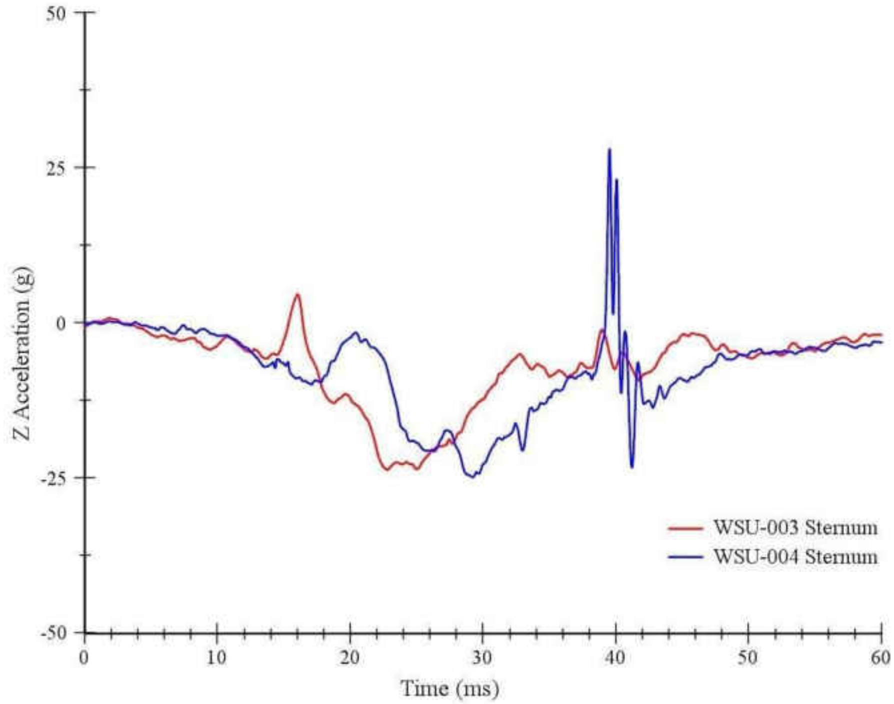

Figure 2-26: Sternum Z Linear Acceleration

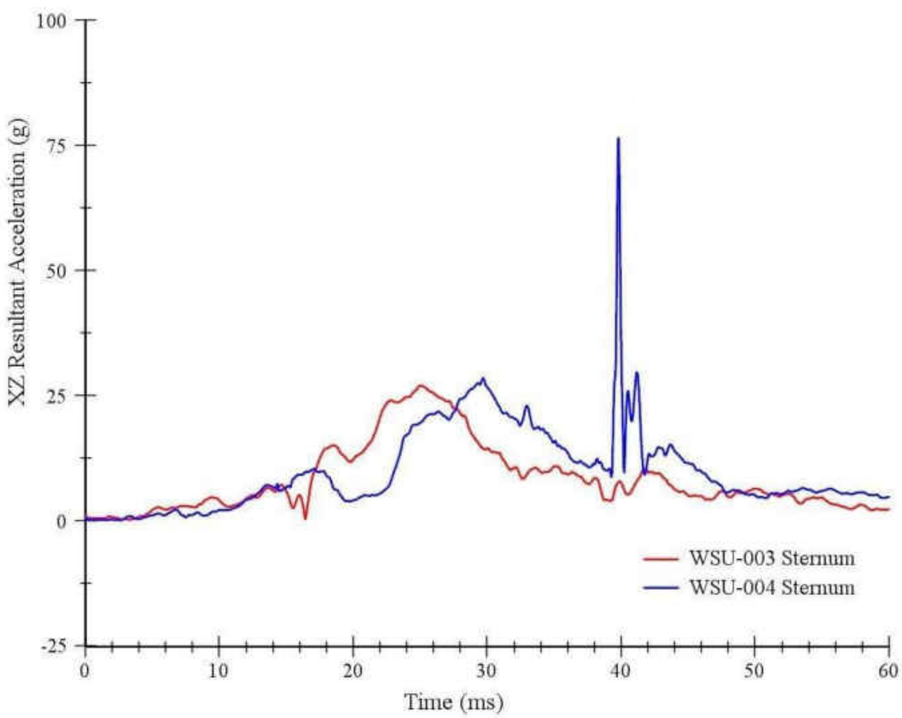

Figure 2-27: Sternum XZ Resultant Acceleration

Next, the sternum rotation in Figure 5-28 shows that both test subjects had a maximum Y rotation of 6°. In addition, the sternum in both tests initially rotates in a counterclockwise direction (extension) and reverses its rotation after 50ms. Two causes for this are possible. First, the shoulder belt could have restrained the torso flexion motion. Second, the flexion motion of the lower abdomen region towards the torso could have contributed to extension rotation of the sternum. It can also be observed from the sternum rotation curve for the WSU-003 test subject that post 50ms the sternum rotates in a clockwise direction with maximum rotation of 3.5°. This opposite rotation may have been caused by the head motion towards the torso.

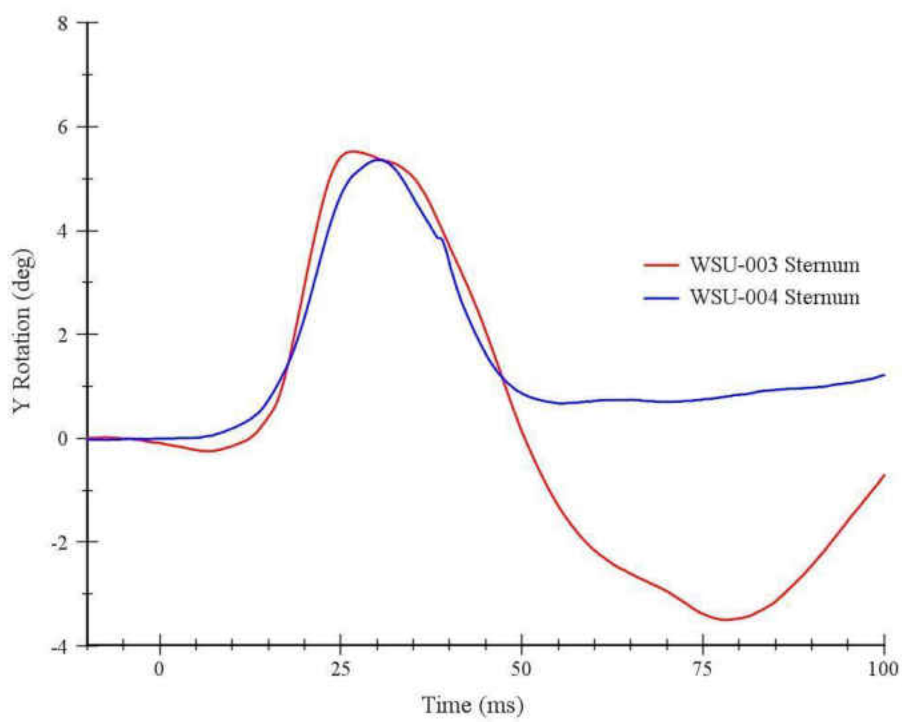

Figure 2-28: Sternum Y Rotation

Head: The head Z acceleration data tabulated in Table 5-1 shows minimal acceleration compared to other body regions for both test subjects. The head of WSU-003 received a peak acceleration of 16 g's, while the head of WSU-004 received 21 g's. Figure 5-29 show that the linear Z acceleration data had discrepancies, possibly due to the influence of angular velocity data. Next, the XZ resultant acceleration data were determined as well. The resultant curve in Figure 5-30 indicates that the head impact response was predominately caused by Z linear acceleration.

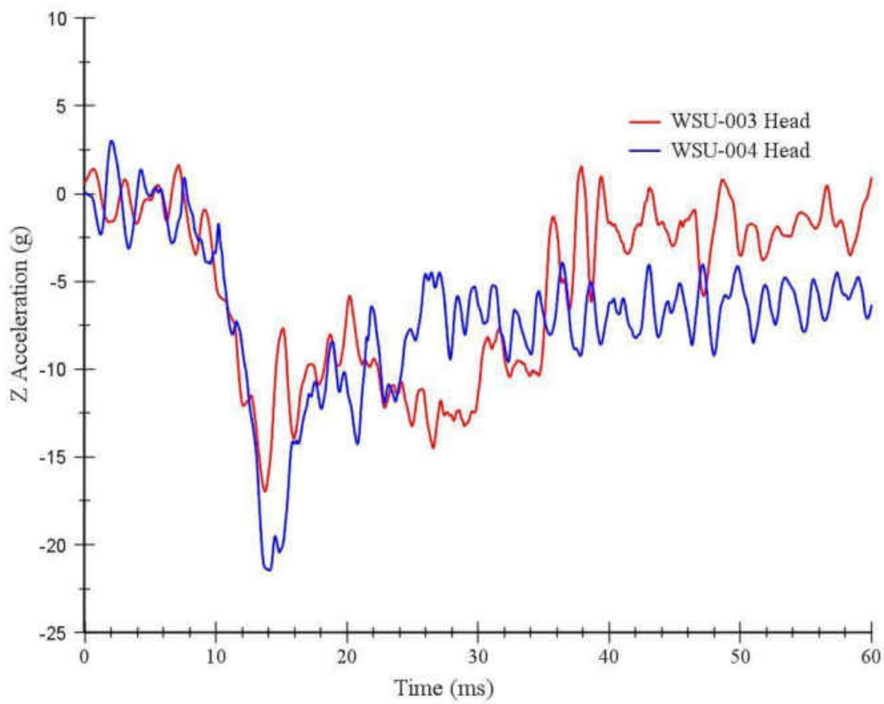

Figure 2-29: Head Z Linear Acceleration

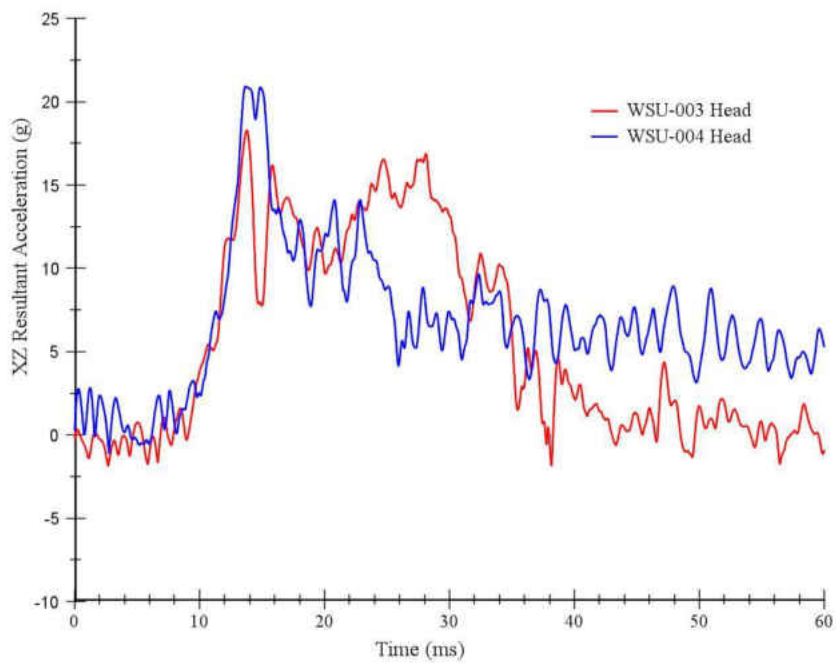

Figure 2-30: Head XZ Resultant Acceleration

The head rotation data due to impact were determined as well. The head rotation around the Y axis was the primary parameter for analysis. However, to examine the local kinematics of the head, its rotation around the X and Z axis was also measured. Additionally, the sensor kinematic data were further verified with the video kinematic data. The X rotation curve in Figure 5-31 initially shows that the head in both tests tends to rotate in a counterclockwise direction around the X axis with a peak rotation of 5°. After 65 ms, the head of WSU-003 maintains its rotation in the same direction, while the WSU-004 head reverses its rotation and inclines towards its left. Next, the rotation data around the Y axis in Figure 5-32 illustrates that upon impact the head initially undergoes an extension motion with maximum rotation of 15° and 10° for the WSU-003 and WSU-004 test respectively. Furthermore, in both tests, after 50 ms the head reverses it rotation and flexes towards the torso. At the same time the sacrum flexes towards the torso (Figure 5-13). This observation demonstrates the submarine motion of the occupant. Finally, the

Z rotation curve in Figure 5-33 shows a maximum rotation of ± 2°, which is minimal compared to the motion around the other coordinate axes.

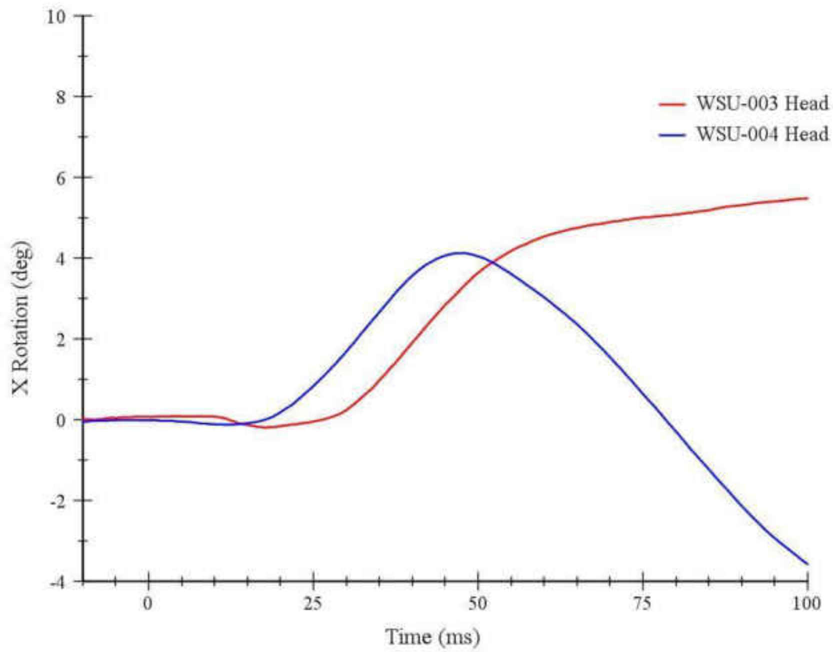

Figure 2-31: Head X Rotation

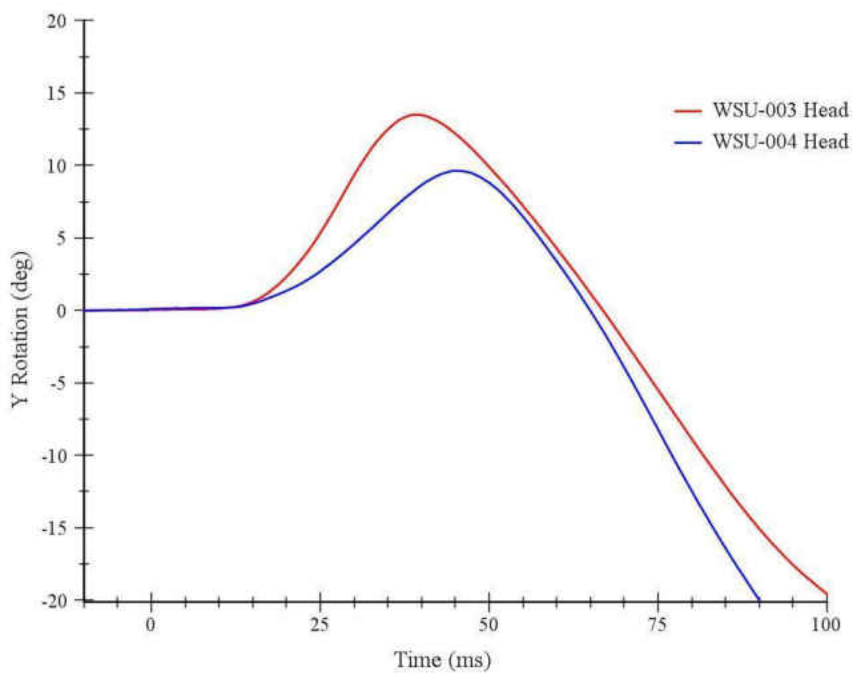

Figure 2-32: Head Y rotation

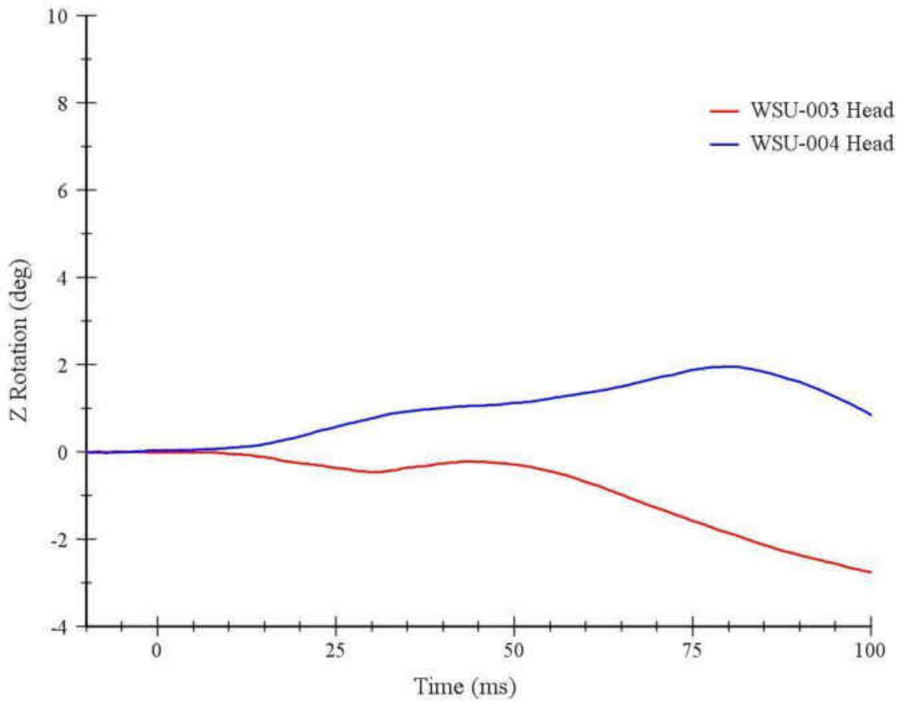

Figure 2-33: Head Z Rotation

In addition to the head acceleration and rotation data, the head motion relative to the torso and sacrum were also determined in this study. The Y rotation data of the head and T1 spine were used to calculate the head/torso relative motion. These relative motion data provide the timing and magnitude between the aforementioned body regions during the simulated vertical loading event. The relative head/T1 spine and head/sacrum rotation along the Y axis, for each test, is shown in Figure 5-34. The head/T1 motion indicates that the head has a maximum rotation relative to the torso, while the head kinematics in relation to the sacrum shows the torso flexion with the buttock riding upward in the X direction on the seat bottom.

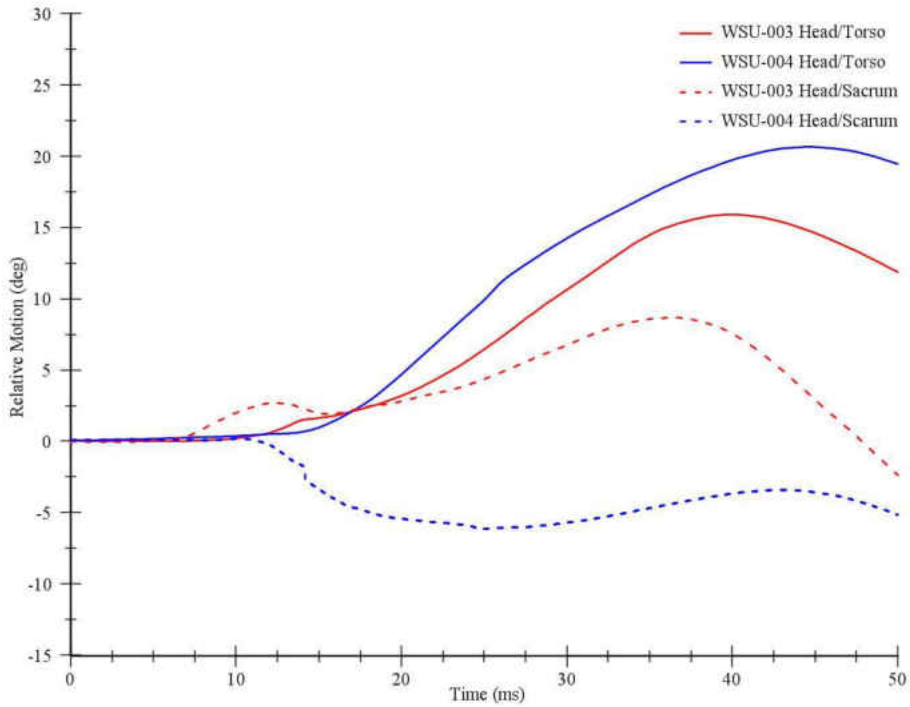

Figure 2-34: Relative Motion

2.1.1 Spinal Compliance

The spine responses under vertical loading were also evaluated by measuring the displacement between the transducers along the spine-head segment. In the current study, the double integrated Z linear acceleration data were used to analyze spine compliance along the primary loading Z axis. Figure 5-35 shows the spine compression in the Z direction between the head, AO- T1, T1-T5, T5-T8, T8-T12, and T12-S1 respectively, separated for each test. The spine compliance data measures the displacement of the former segment relative to the latter. For example the T1/T5 compliance data provides the displacement of the T1 segment relative to the T5 segment.

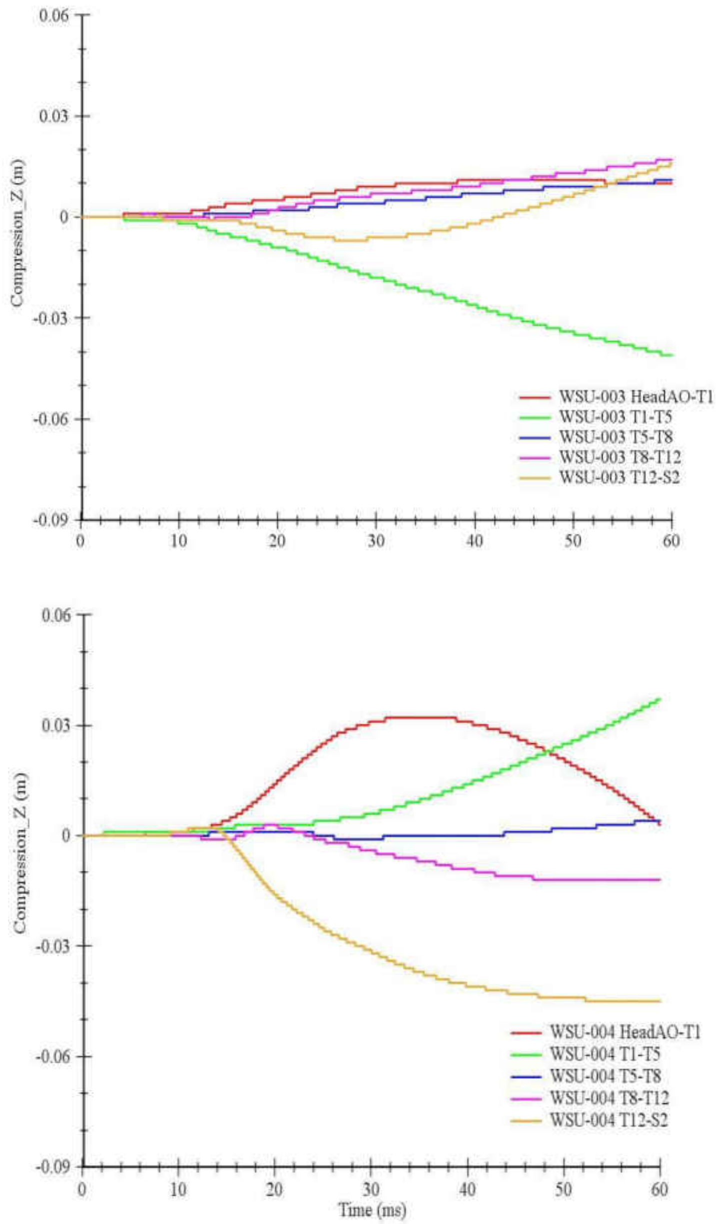

Figure 2-35: Spine Z Axial Compliance, WSU-003 [top] and WSU-004 [bottom]

2.2 Video Kinematic Analysis

Kinematic responses were analyzed in two ways. First, the test subject kinematics during the event was compared between the two tests. Next, the target marker displacement was determined. In the current study, these analyses were performed using the video recorded by the lateral camera. The video data were trimmed with a range set as Time zero (time of impact) to

300 ms. For the first analysis, desired time frames were selected which correspond to 0 ms, 20 ms, 100 ms and 300 ms. Figure 5-36 illustrates the kinematics comparison between the two tests. In addition, in Figure 5-37 the frame corresponding to 300 ms was superimposed on the Tzero frame. Furthermore, the Z displacement pathways followed by the target markers are also presented in the same figure. The arrow shows the direction of the displacement of the marker on the Z axis. For the second analysis, target markers glued to the specimen suit were tracked to obtain the displacement of the Z and X axis respectively. The representative displacement curves along the X and Z axis are plotted in Figures 5-38 and 5-39 for WSU-003 and WSU-004, respectively. The aforementioned target marker displacement curves for both tests reveal that the specimens had similar kinematic motion.

Figure 2-36: Kinematic comparison between WSU-003 and WSU-004 at different time points which includes: Time zero, 20, 100, 300 ms, respectively.

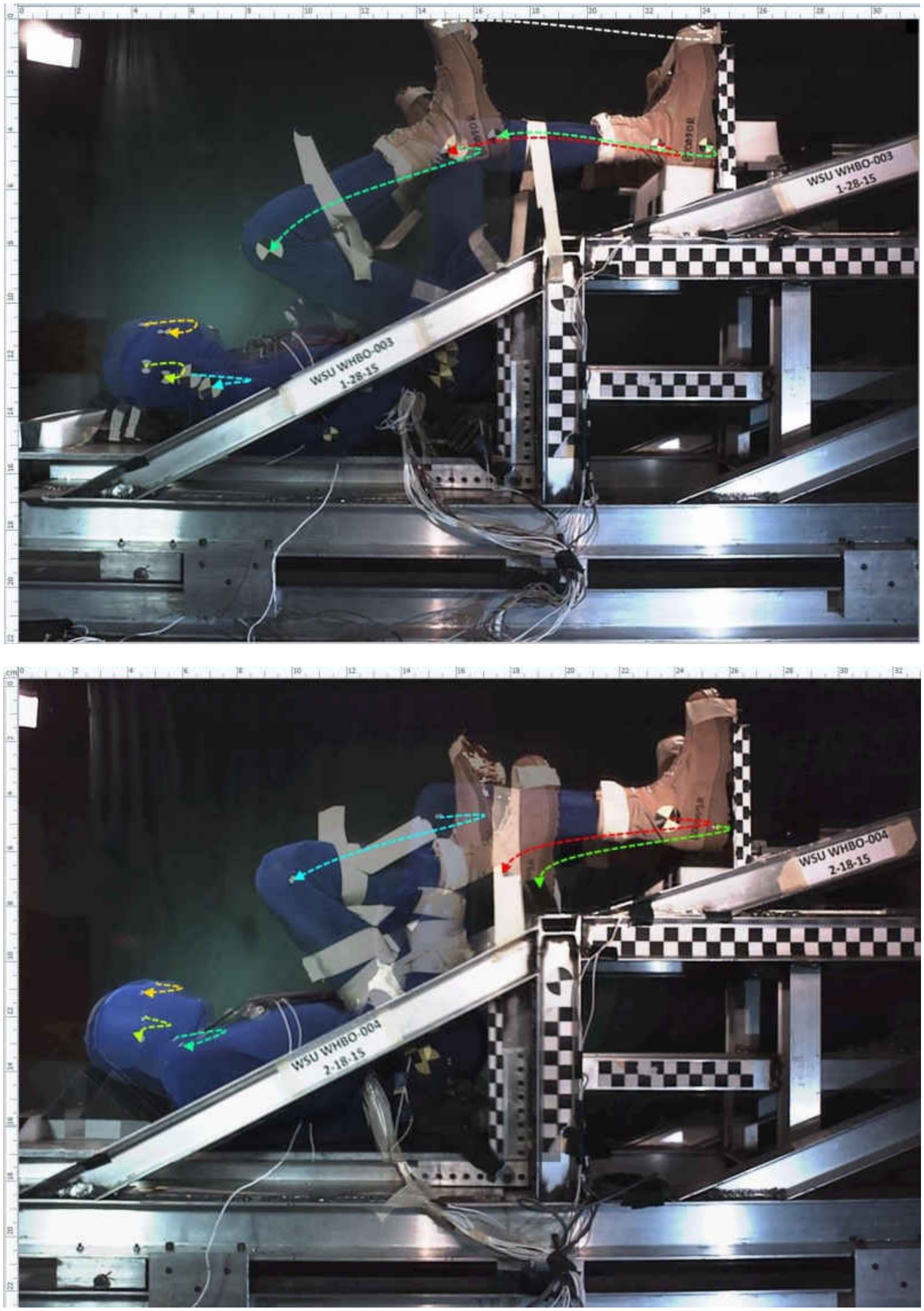

Figure 2-37: Target marker displacement (cm) in Z from Time zero to 300ms for WSU-003 [top] and WSU-004 [bottom]. Targets were placed at the lateral malleolus, boot heel, tragion, infraorbital notch, lateral epicondyle and proximal humerus, respectively in this study.

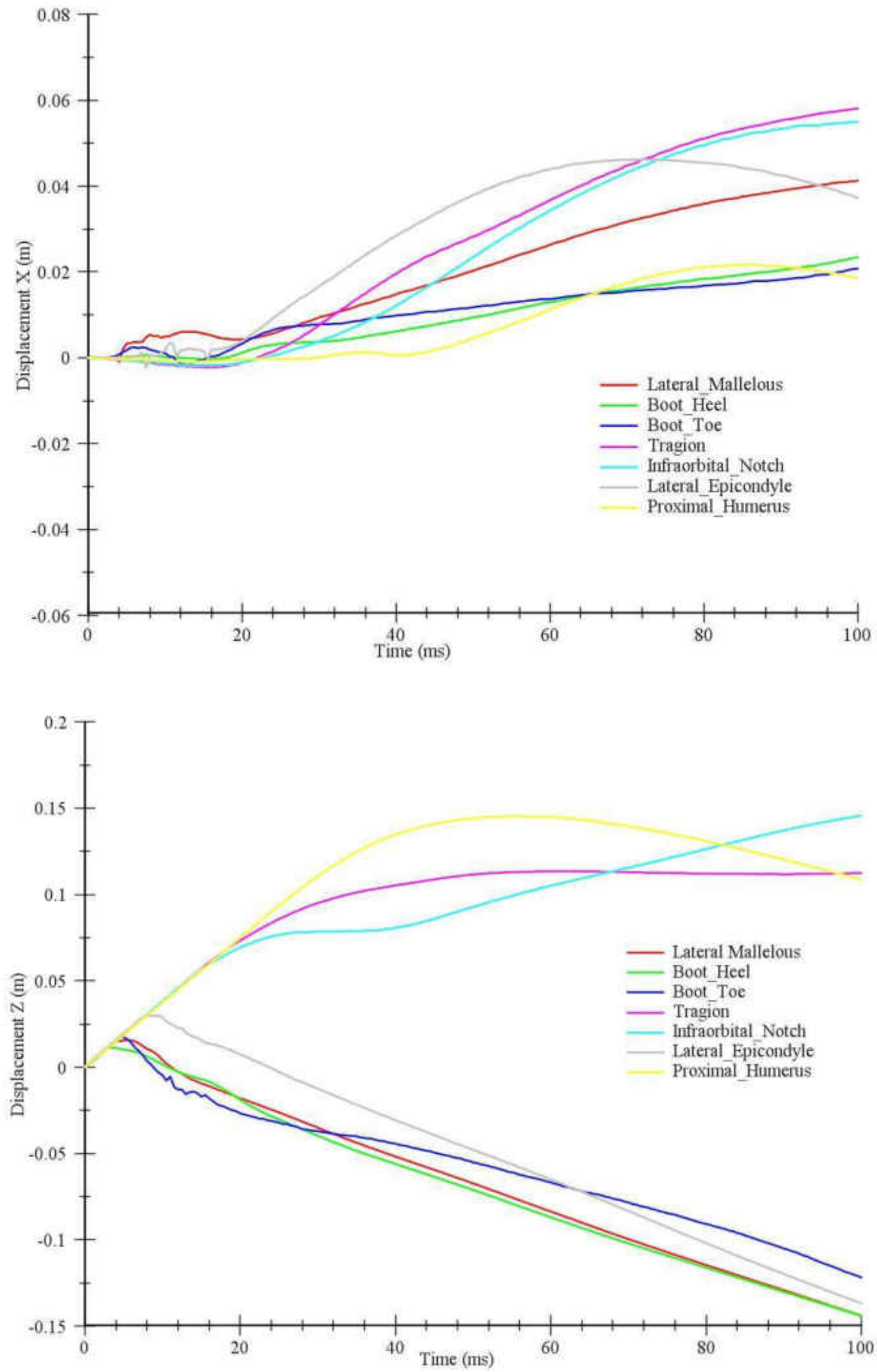

Figure 2-38: WSU-003 Target Marker Displacement along X [top] and Z [bottom] relative to seat.

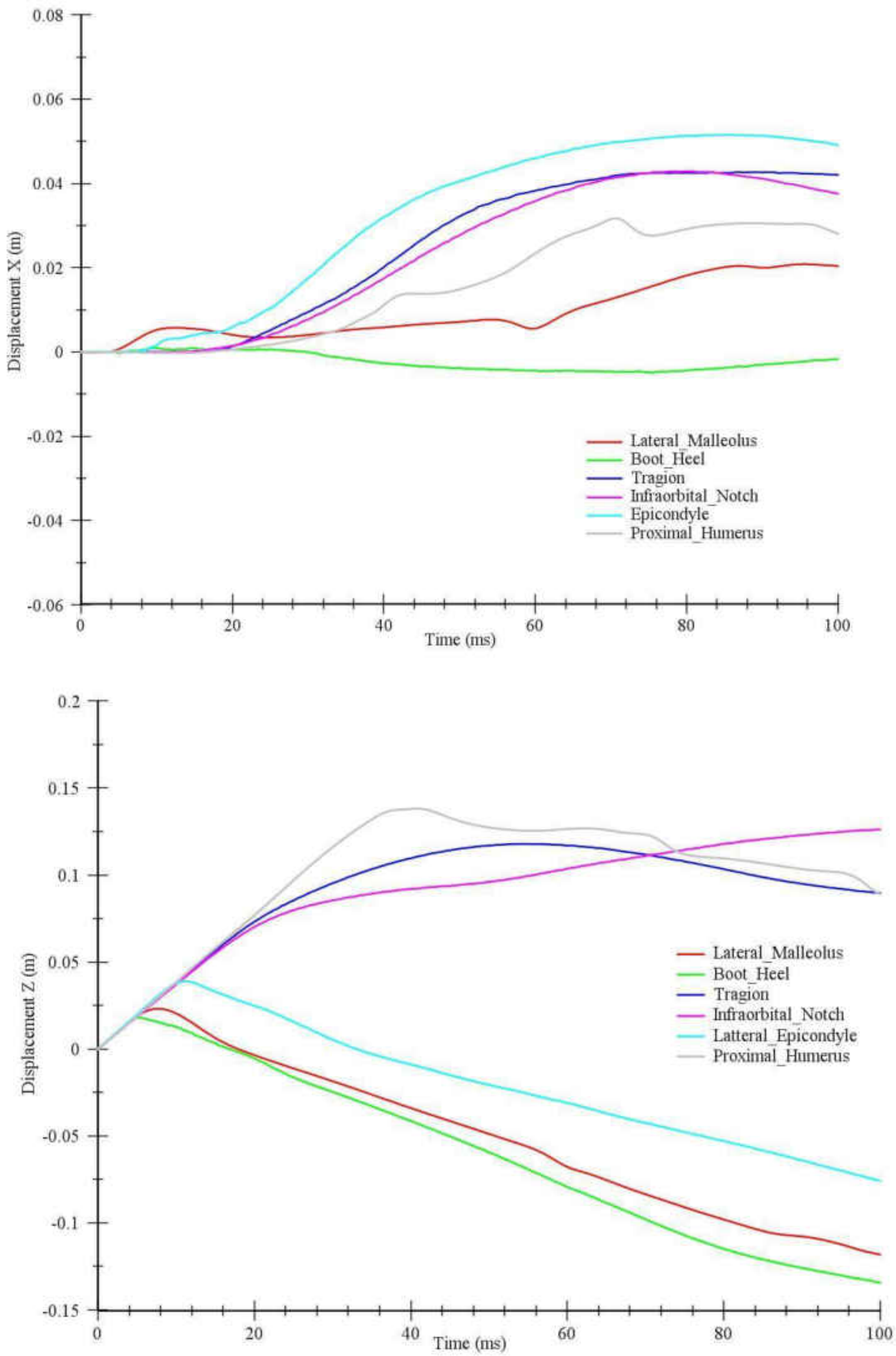

Figure 2-39: WSU-004 Target Marker Displacement along X [top] and Z [bottom] relative to seat.

In addition to tracking the target displacement for the shoulder, knee, and ankle, advanced processing was performed. For the shoulder kinematics, the proximal humerus target marker displacement was considered and the data were normalized based on the test subject's height. Furthermore, using the Romer Arm and MIMICs coordinate points, the hip center was estimated. Using this combined approach, the shoulder motion relative to the hip joint's center was determined. Figure 5-40 presents the shoulder displacement along the X and Z axis, for each test respectively.

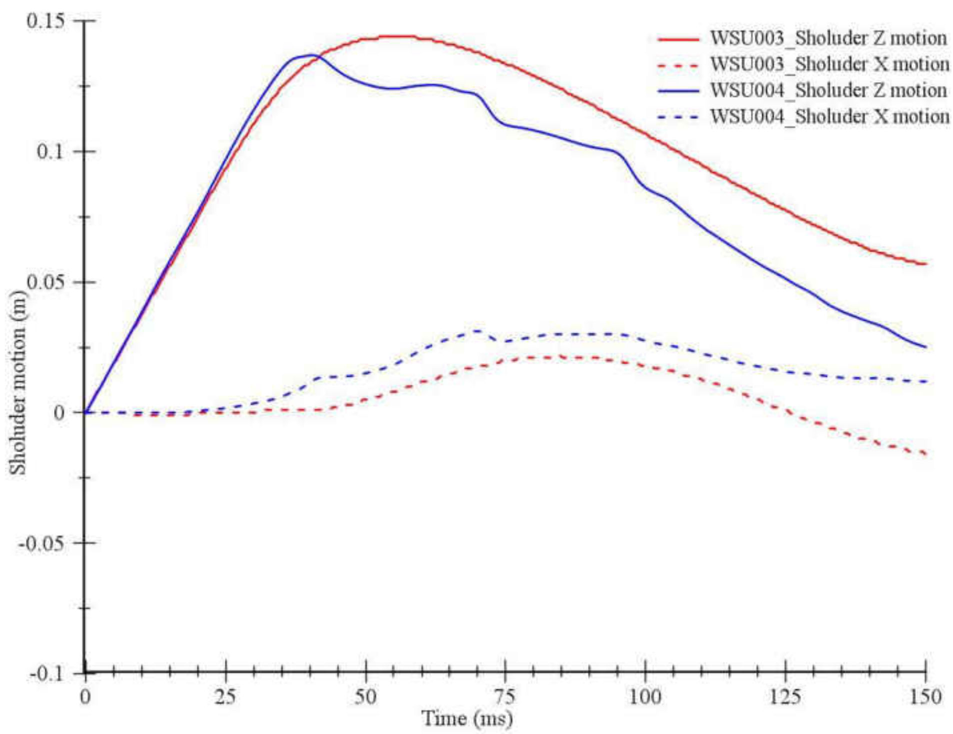

Figure 2-40: The Shoulder Motion.

For knee motion the target marker displacement data obtained from both the lateral and overhead video analysis were used. The epicondyle and patella target maker displacement from the lateral and overhead camera views were selected for this analysis. The tracked displacement data were normalized based on the test subjects' femur length. Figure 5-41 illustrates the knee motion relative to the three axes X, Y, and Z respectively. The knee displacement along the Z direction was higher compared to the displacement in the other two directions. Also, the knee displacement in the negative Z direction confirms the motion of the femur towards the head

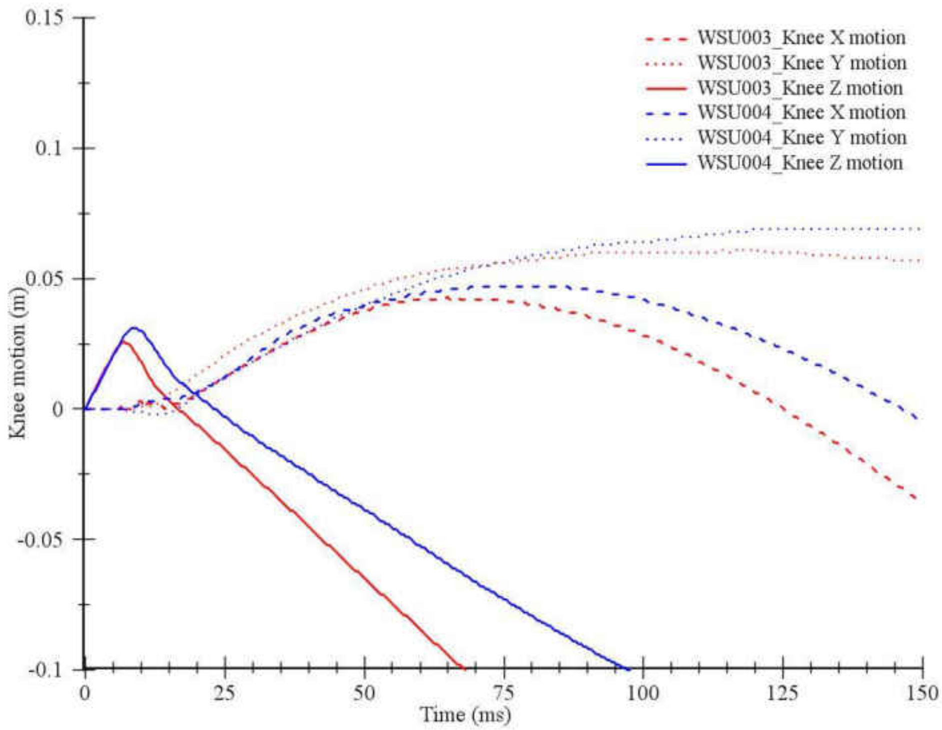

Figure 2-41: The Right Knee Motion.

The ankle joint angle was evaluated by measuring the angle formed by the foot with the tibia during the event. For this measurement, the angle formed by the lateral epicondyle, boot heel and the boot toe marker were considered. Prior to impact the ankle was positioned at a 90° angle. Upon impact the angle increased by 3° to 5° initially, followed by a decrease of 3° to 6°. The feet inertia could have caused the initial increase in the angle. Upon impact, the floor pushed the boot upward toward the torso in the Z direction. The upward displacement of the tibia increased the ankle angle further (Figure 5-42). In the WUS-003 test subject, the ankle had a maximum angle of 114° measured at 75 ms, while the ankle of WSU-004 had a maximum angle of 96° at the same time.

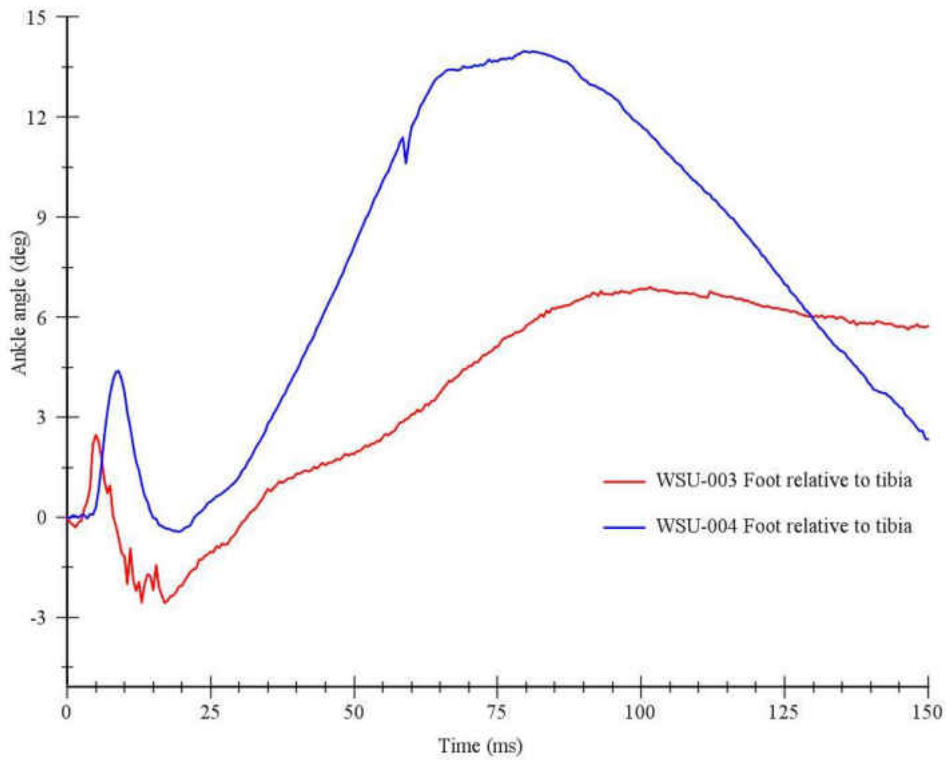

Figure 2-42: The Right Foot Motion Relative to the Right Tibia.

The two PMHS tests provide a preliminary understanding in terms of biomechanical response due to simulated UBB loading. Additionally, these impact responses could support the development of biomechanical response corridors for the warrior dummy design.

CHAPTER 6

AN EXPERIMENTAL AND NUMERICAL STUDY OF HYBRID III DUMMY RESPONSE TO SIMULATED UNDERBODY BLAST IMPACTS

6.1 Introduction

Work has been continuous to improve the biofidelity of mechanical surrogates, such as anthropometric test devices (ATDs) commonly known as crash test dummies, to provide better occupant protection and injury mitigation in motor vehicle crashes. These ATDs are widely used as physical surrogates to investigate occupant response and develop safety equipment in automobiles. In recent years, researchers have also started using automotive ATDs for analyzing an occupant's response to an underbody landmine blast for military vehicles. In particular, the Hybrid III ATD has been used in both live fire (explosive) testing and seat cushion (static) evaluation studies (Bosch et al., 2014; Kargus et al., 2008; Van der Horst et al., 2005; van der Horst and Leerdam, 2002). In an underbody improvised explosive device (IED) explosion scenario, the detonation generates blast waves with substantial kinetic energy. This blast energy accelerates the vehicle and its occupants vertically upward, as well as deforms the structure of the vehicle. The deformed floor transmits loading directly to the lower extremities of the occupants, whereas the vertical acceleration of the vehicle produces large pelvic and spine acceleration. This, in turn, produces complex acceleration-deceleration injuries to lower legs, pelvis and spine. The resulting injuries, often incapacitating, have a long lasting effect on the soldiers, yet the injury mechanism for these kinds of combat-related trauma is not yet fully understood.

Most of the recent underbelly blast (UBB) studies have concentrated on investigating the lower extremity responses to vertical loading. Next to the tibia, the lumbar spine is the second most vulnerable region when the body sustains a very large vertical acceleration (TR-HFM-090, 2007). Compared to studies of isolated lower extremities, very little whole body cadaver testing (Bailey et al., 2013; Yoganandan et al., 2014) has been performed for evaluating whole body responses to UBB loading conditions. In addition, only a few researchers have investigated the Hybrid III dummy response under similar vertical loads (Bailey et al., 2013; Ken-An Lou, 2013). Of the reported ATD blast impact studies, only the lower leg and lower torso responses were analyzed (Bailey et al., 2013; Ken-An Lou, 2013). Evaluating the whole ATD response and the kinematic behavior is essential for understanding the occupant response to such vertical impact conditions. The performance and accuracy of these ATDs are crucial during the assessment of occupant injury under UBB impact. The objective of this study was to conduct a series of simulated UBB impact tests to examine the high rate vertical loading response of a Hybrid III ATD. The response, in terms of pelvis acceleration, tibia force, lumbar spine force, chest acceleration, upper neck force, and head acceleration was measured. In addition to the ATD test series, the finite element Hybrid III dummy model developed by LSTC (Livermore, CA) was updated with high rate material properties then validated against measured experimental data. This validated model was used to understand the issues related to damaged pelvis flesh and foam noted in Hybrid III testing.

6.2 Methodology

Two series of Hybrid III dummy impact tests were performed using a modified Wayne Horizontal Acceleration Mechanism (WHAM) III sled system. The two loading conditions used for these tests are shown in Table 6-1. For all experiments, the Hybrid III dummy was fitted with a pair of Lightweight Desert Combat Boots (Size 11, Belleville Boot Company, IL). Five tests were conducted for each loading condition.

Table 6-1: Experimental impact test condition matrix.

	Seat		Foot Floor	
	Impact Speed (m/s)	Time to peak (ms)	Impact speed (m/s)	Time to peak (ms)
Condition 1	5	5	5	5
Condition 2	4	10	6	5

For condition 2 ATDs testing were performed using the same sled setup as the one used for PMHS testing. While for condition 1 with the same seat and foot floor velocity, the movable foot floor system was replaced with a rigid foot plate mounted directly to the seat fixture. Furthermore, the honeycomb blocks were replaced with four hydraulic shock absorbers (model RCOS 2X 5 BS 04 54 Efdyn Inc., OK). During the impact, these hydraulic shock absorbers stopped the seat and determined the time to peak for both seat and floor pulse. Figure 6-1 shows the rigid floor plate and hydraulic shock absorber used in the tests for loading condition 1.

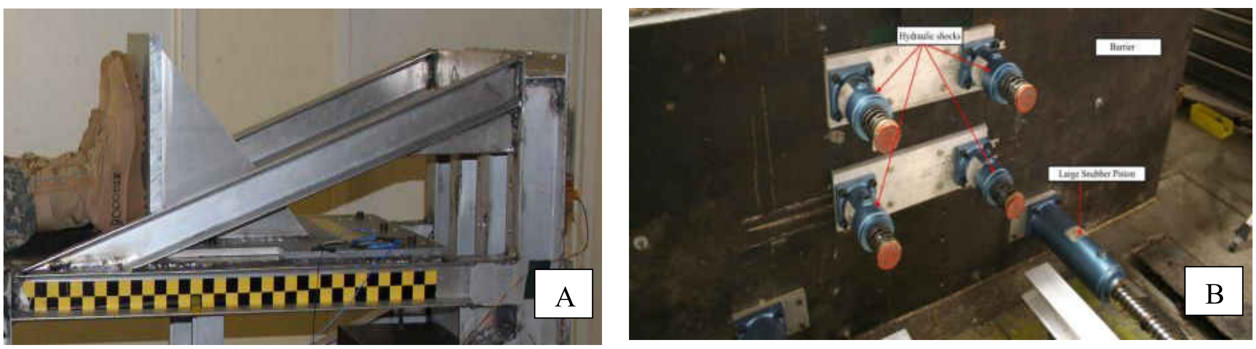

Figure 6-1: A, B- A rigid foot floor plate and four hydraulic shock absorbers used for test condition 1 with the same loading condition at the seat and foot floor.

6.2.1 Data Acquisition System and Dummy Instrumentation

A slice Pro (Diversified Technical Systems, Inc., CA) data acquisition system was used for each test. A total of 51 channels were sampled at the rate of 500,000 samples per second with a 100,000 Hz anti-aliasing, multipole low-pass Butterworth filter. A lateral view of the event was recorded using an NAC GX-1 camera (NAC Image Technology, CA) with a 24 mm Nikon lens. This camera was positioned at 1.57 m from the right side edge of the seat and recorded the event at 2,000 frames per second. Acceleration and force data were an integral part of evaluating the dummy's biomechanical responses. The acceleration data were measured using (model 7264 Endevco San Juan Capistrano, CA) accelerometers, while various load cells (Humanetics, Plymouth, MI) were used to quantity the force and moment data. Table 6-2 lists the transducers installed in the ATD. Additioanlly, the seat pan and floor accelerations were measured using 7270 Endevco accelerometers which were attached to the bottom of the seat and foot plate, respectively.

Table 6-2: Instrumentation Matrix

Description	Manufacture	Model	Number
Pelvis Accelerometer	Endevco	7264C-2KTZ	3 (each per axis)X, Y, Z
Chest Accelerometer	Endevco	7264C-2KTZ	3 (each per axis) X, Y, Z
Head Accelerometer	Endevco	7264C-2KTZ	3 (each per axis) X, Y, Z
Upper Tibia Load Cell	Humanetics	1583	2 (each per leg) R, L
Lower Tibia Load Cell	Humanetics	1584A	2 (each per leg) R, L
Femur Load Cell	Humanetics	1914AJLN2	2 (each per leg) R, L
Lumbar Spine Load Cell	Humanetics	1842	1
Upper Neck Load Cell	Humanetics	1716A	1
Lower Neck Load Cell	Humanetics	1794A	1

6.2.2 Simulation Setup

In addition to the Hybrid III tests, a finite element model was used to analyze the biomechanical response along with stress-strain values in detail. Although the overall kinematics and biomechanical responses are available through experiments, numerical modeling can be used to analyze the response at component level in more detail. Additionally, after the computational model is properly validated, it can be used to predict the stress-strain contours at the material level and determine the local response of failed components. For example, the stress generated in the foot and buttock regions, which are in direct contact with the loading surface, would be worthy of further investigations in this study. Elsewhere, researchers have also considered a combined laboratory test and numerical based approach for evaluating the lower extremity response due to vertical load (Kraft et al., 2012; Manseau and Keown, 2005; van der Horst and Leerdam, 2002). Lou et al., examined the pelvis and lumbar spine response to vertical loading by conducting both physical test and numerical studies (Ken-An Lou, 2013). A similar combined approach was used in this study to understand the biomechanical response for two UBB impact loading conditions.

A finite element model with rigid seat and a movable floor plate was created with the same geometric details and mass as those used in the experiments. The vertical seat pan and floor acceleration profiles measured from the Hybrid III tests in conditions 1 and 2 were used to validate the numerical model. Figure 4 shows the numerical model positioned on the sled which includes the buttock/seat contact and boot/foot floor plate contact, this simulation setup matched well with the corresponding laboratory setup. All simulations were performed using a commercially available FEA package LS-DYNA 971_R4.2 (LSTC, Livermore, CA).

An initial simulation study with the original LSTC Hybrid III dummy model showed that the FE model failed to replicate the laboratory test response and encountered numerical instabilities at higher speeds. Reasons for such discrepancy include the lack of proper strain rate dependent material properties for various components of the ATD model, especially with the pelvis and the lower leg that are in direct interface with the structure. Because a typical UBB event includes very large magnitude acceleration in less than 10 ms, a finite element analysis of such a loading environment requires a strain rate-dependent material model in order to provide accurate stiffness results. Therefore, the material laws and properties for four components, namely the pelvis flesh, lower leg flesh, heel pad, and lower leg skin, of the original LSTC dummy model were modified. As previously stated, these dummy parts were directly involved in the pathways of load transfer to the torso and lower limbs.

Zhu et al. (2015) validated a lower extremity finite element model by a combined experimental and numerical approach to determine the high rate material properties of the lower leg flesh, heel foam, and lower leg skin of a Hybrid III ATD. Their results were integrated into the public domain LSTC Hybrid III FE model for this study. Furthermore, Kalra et al. (2016) incorporated the combat boot model and validated the model against experiments done by Barbir et al. (2005) for similar loading conditions. The validated lower extremity model, which included strain rate dependent material models and associated properties for the aforementioned components and the validated boot model were integrated into the LSTC Hybrid III model for this study. The dummy position relative to the seat pan and foot floor plate matched with the experimental ATDs positioning (Figure 6-2).

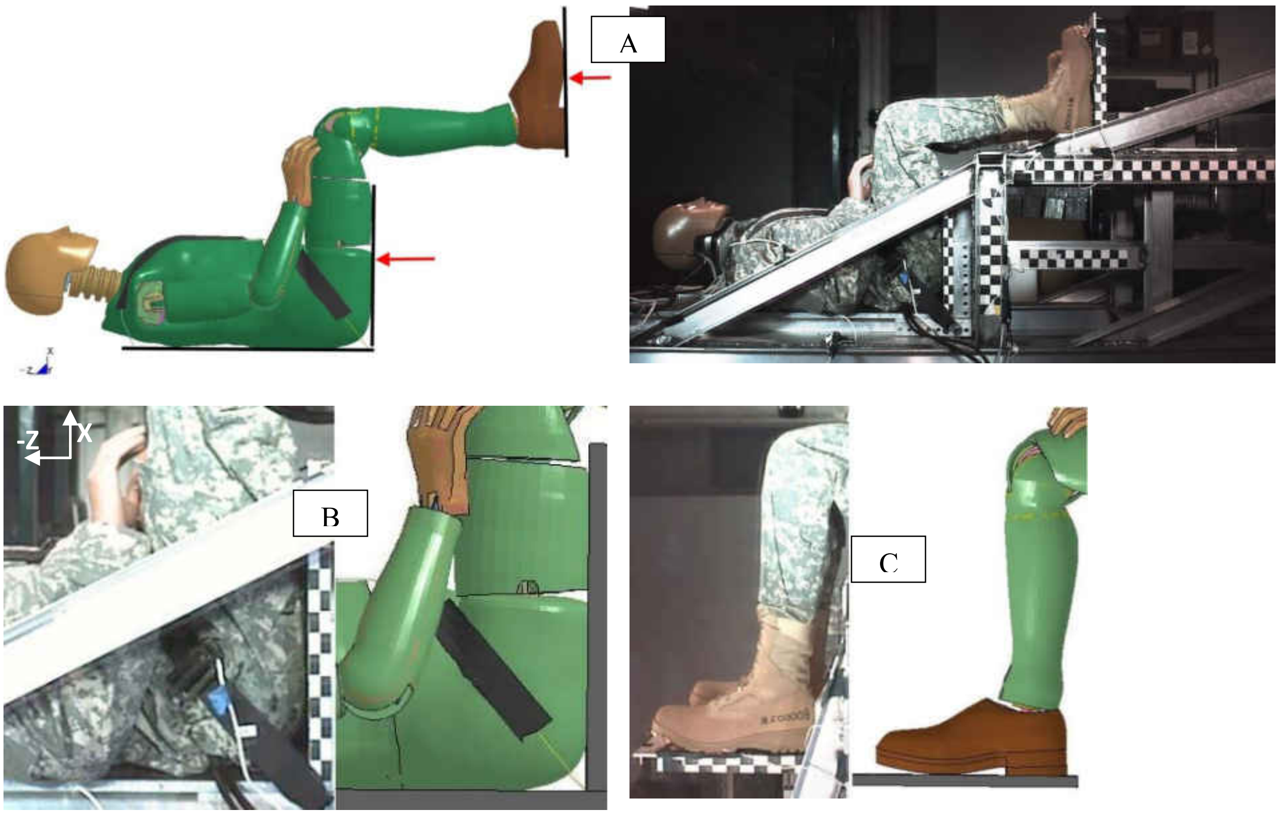

Figure 6-2: A- Comparison between the finite element and physical Hybrid III sled setups. B, C – The pelvis and foot of the FE model and physical ATD contact with the seat and floor plate, respectively.

The integrated Hybrid III, lower extremities, and boot model required additional modifications before it could be used. The material model which was optimized for the lower leg flesh from Zhu et.al (2015) study, was also used for pelvis flesh model since both share the same material in physical dummy. Furthermore, the pelvis section was updated to solid elements with same thickness as of the original LSTC pelvic component (Appendix E). In addition, the mechanical behavior of the lumbar spine was rationalized by integrating a stiffer viscoelastic material card obtained from a previous study (Ken-An Lou, 2013). Table 6-3 shows a summary of the material model "cards" that were used in this study.

The WSU whole body finite element model was used to simulate the experimental seat and foot impact loading conditions. Once validated, the model was used to determine the stress generated on the pelvis flesh due to the vertical load generated by the seat pan in order to investigate why the Hybrid III pelvis ruptured during the simulated UBB tests.

A commercially available software package Correlation and Analysis (CORA) version 3.6.1 was used to evaluate the correlation between the WSU FE model response and the test 1 data for both loading conditions. CORA software has two sub techniques to assess the correlation: corridor and cross-correlation methods. In the current study, cross-correlation was used to evaluate the relationship between the model and actual ATD. The cross-correlation technique uses phase shift, shape and area below the curve for assessing the score (Gehre et al., 2009). A separate cross correlation rating score for the numerical response for body region, for each loading condition was determined. Table 6-4 shows the parameters used in CORA for this study. CORA allows users to adjust the duration for which the analysis is performed. For pelvis acceleration, the response was completed within 15ms; therefore, the duration for correlation analysis was set to 15 ms for the pelvis data, whereas for the remaining responses especially for the torso, the loading event is longer. For the torso, tibia and head response the phase duration for correlation analysis was extended to 25 ms. Last, for LSTC numerical model, the CORA analysis was run up to 12 ms for the pelvis response alone. Since the original LSTC model becomes numerical unstable upon impact under the current loading condition.

Table 6-3: Material Model Matrix.

Material	LS-DYNA material type, material properties (units: mm, kg, ms, GPa, kN)					
Heel-pad foam	* MAT_FU_CHANG_FOAM (Mat_83) (Zhu et al., 2015)					
	RO	E	DAMP	TBID	BVFLAG	HU
	6.4E-7	0.15	0.05	Figure 15	1.0	1.0E-3
Foot-skin	* MAT_OGDEN_RUBBER (Mat_77_O) (Zhu et al., 2015)					
	RO	PR	MU1	MU2	ALPHA1	ALPHA2
	1.28E-6	0.49	2.0E-4	-1.0E-4	1.60	-1.30
	G1	G2	G3			
	0.022	0.0010	1.00E-4			
	BETA1	BETA2	BETA3			
	11.0	5.0	1.0			
Lower leg flesh	* MAT_OGDEN_RUBBER (Mat_77_O) (Zhu et al., 2015)					
	RO	PR	MU1	MU2	ALPHA1	ALPHA2
	8.6E-7	0.49	0.028	-0.0025	0.2	-0.116
Pelvis flesh	* MAT_OGDEN_RUBBER (Mat_77_O)					
	RO	PR	MU1	MU2	ALPHA1	ALPHA2
	8.516e-9	0.49	0.0028	-0.0025	0.2	-0.116
Lumbar Spine	* MAT_VISCOELASTIC (Mat_006) (Ken-An Lou, 2013)					
	RO	BULK	G0	GI	BETA	
	2.050E-6	0.112	0.00123	0.001	0.11	

Table 6-4: The CORA Analysis Parameter used in this study.

A_THRES	B_THRES	A_EVAL	D_MIN	D_MAX	INT_MIN	K_V
0	0	1	0.01	0.12	0.80	10
K_G	K_P	G_V	G_G	G_P	G_2	
1	1	0.50	0.50	0	0.50	

6.3 Results

The representative floor and seat acceleration curves, separated for each loading condition are plotted in Figures 6-3 and 6-4. The structure and dummy acceleration responses were filtered using a 1,000 Hz digital filter, while the force responses were filtered using 600 Hz digital filter. The biomechanical responses, in terms of the lower tibia force, pelvis acceleration, chest acceleration, head acceleration, lumbar force, and upper neck force, were measured (Figures 6-5 through 6-10).

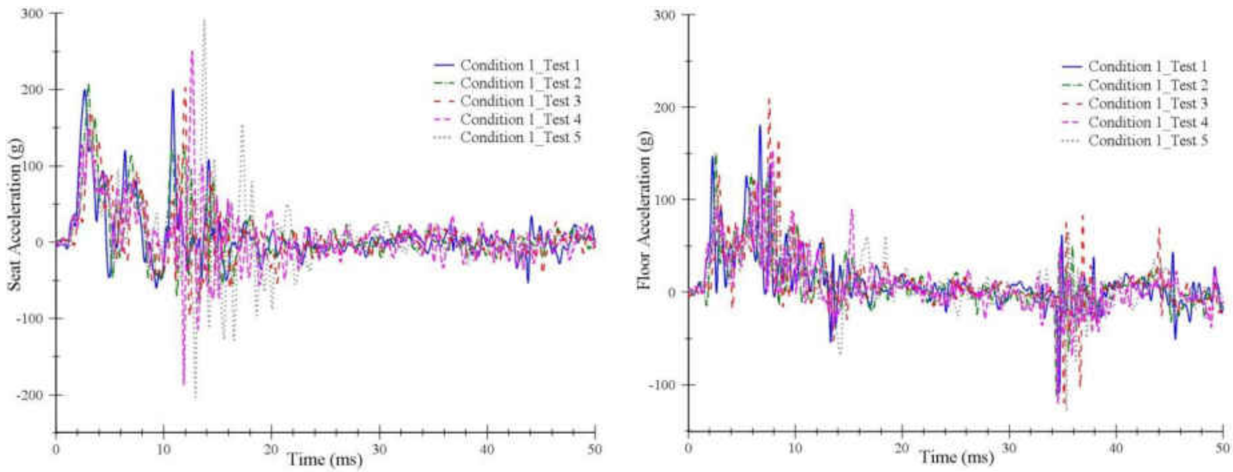

Figure 6-3: Loading condition 1 floor and seat acceleration curve for the five consecutive tests, respectively.

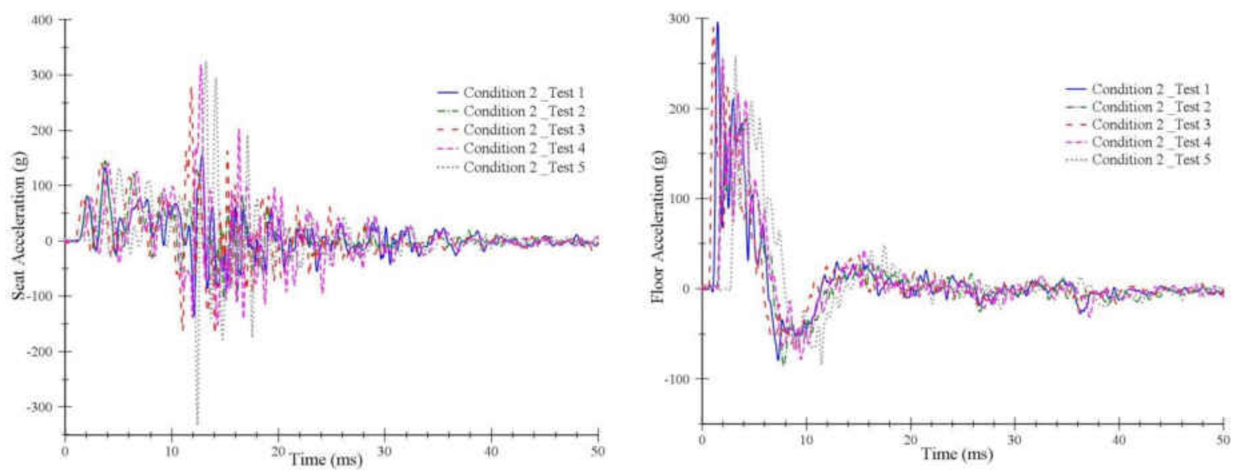

Figure 6-4: Loading condition 2 floor and seat acceleration curve for the five consecutive tests, respectively.

The lumbar spine force response for loading condition 1 was missing due to a sensor failure. The structure acceleration data in Figures 6-3 and 6-4 showed that the sled was capable of producing highly similar acceleration time histories among the tests. Though the seat accelerations were similar between the consecutive tests, the ATD pelvis responses were very close in duration but the peak value increased with each successive impact as shown in Figure 6-5. On the contrary, the lumbar spine, chest, upper neck, head, and lower tibia had a similar response profiles (Figure 6-5 through Figure 6-10) for a given tests condition.

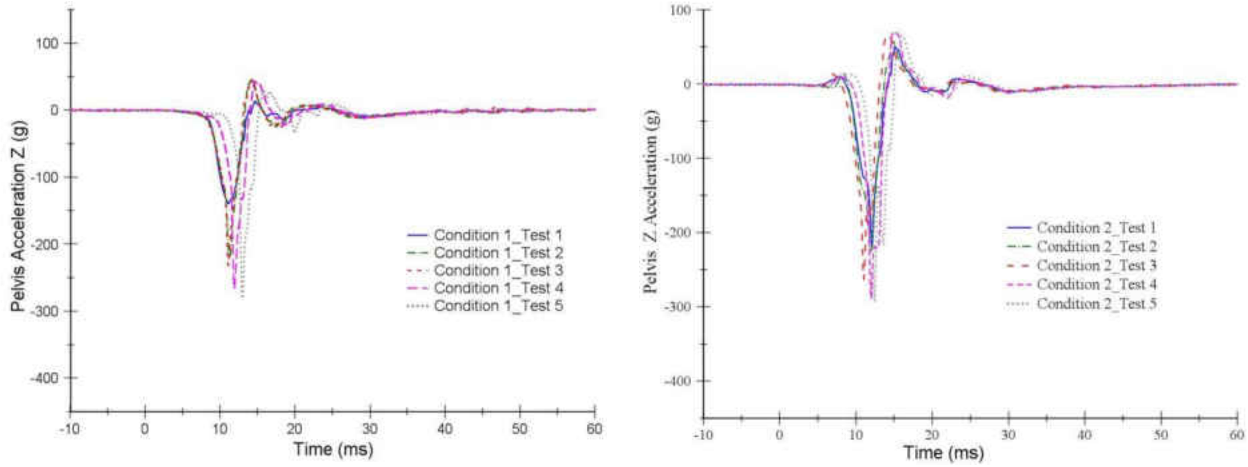

Figure 6-5: The pelvis acceleration for loading condition 1 and 2, respectively.

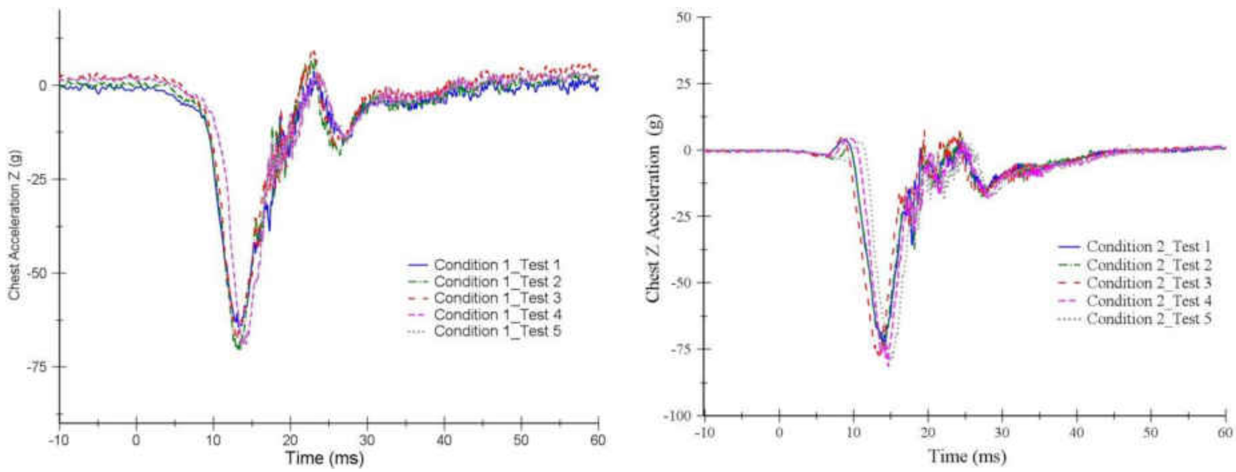

Figure 6-6: The chest acceleration for loading condition 1 and 2, respectively.

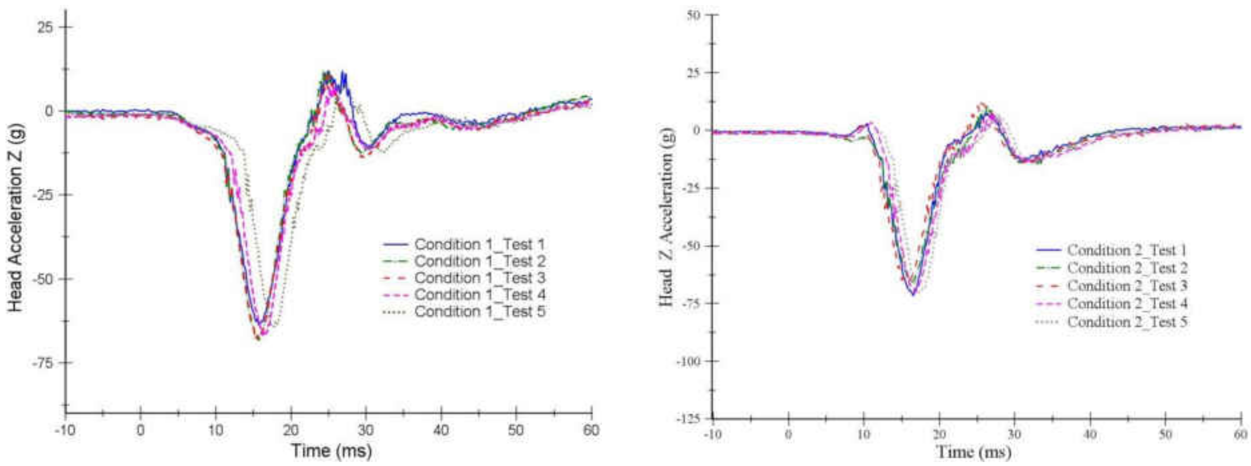

Figure 6-7: The pelvis acceleration for loading condition 1 and 2, respectively.

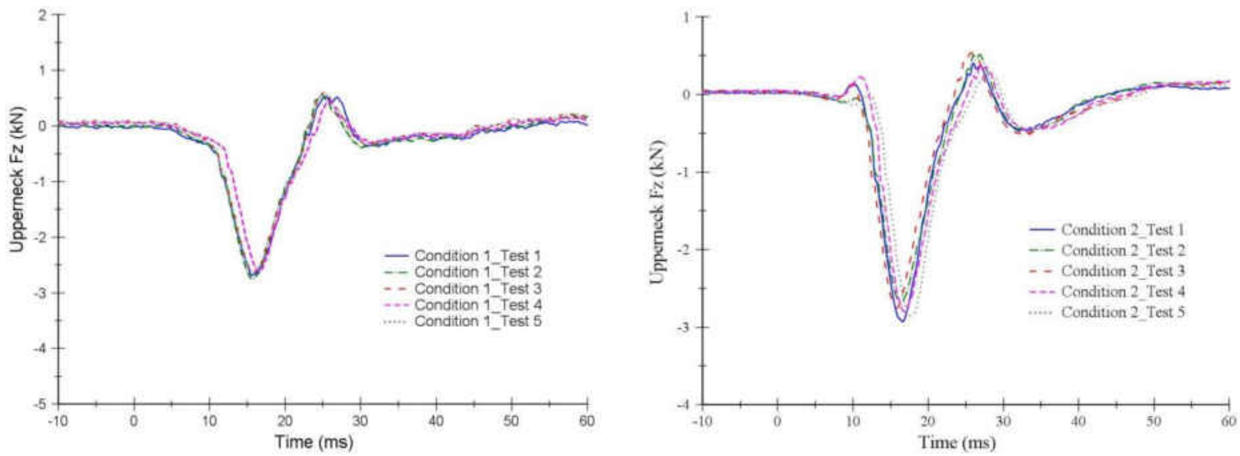

Figure 6-8: The upper neck force for loading condition 1 and 2, respectively.

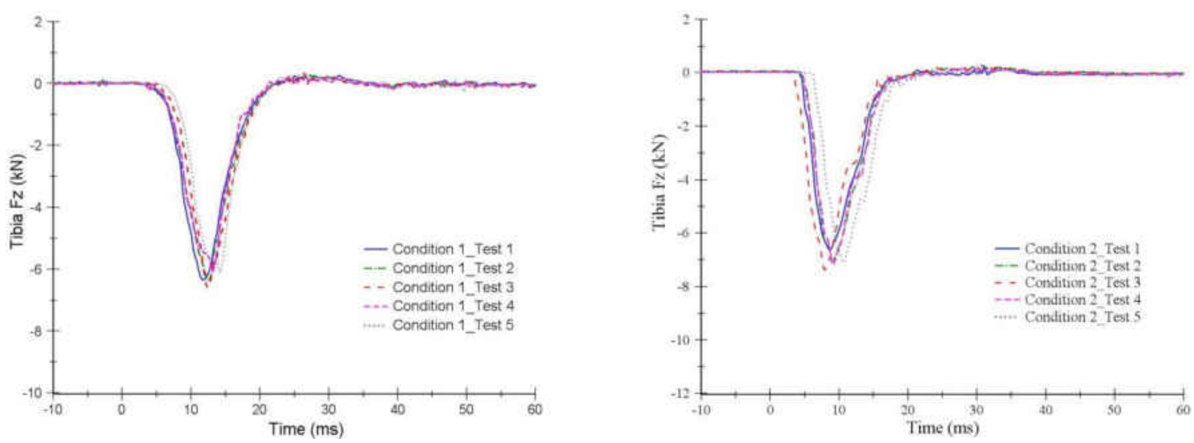

Figure 6-9: The tibia force for loading condition 1 and 2, respectively.

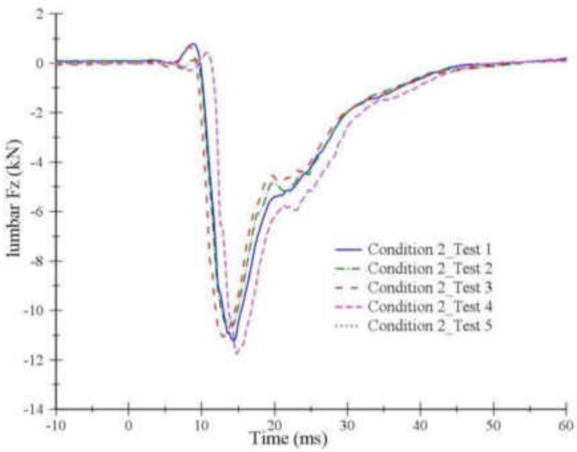

Figure 6-10: The lumbar spine load for loading condition 2.

In addition to the increase in pelvis peak response with each successive test, it was also observed that the pelvis flesh and foam ruptured after the first impact and the condition worsened with consecutive impacts, respectively, as shown in Figure 6-11. Due the pelvis flesh damage, only the structure acceleration profile from the first test for both the condition was considered for the numerical study.

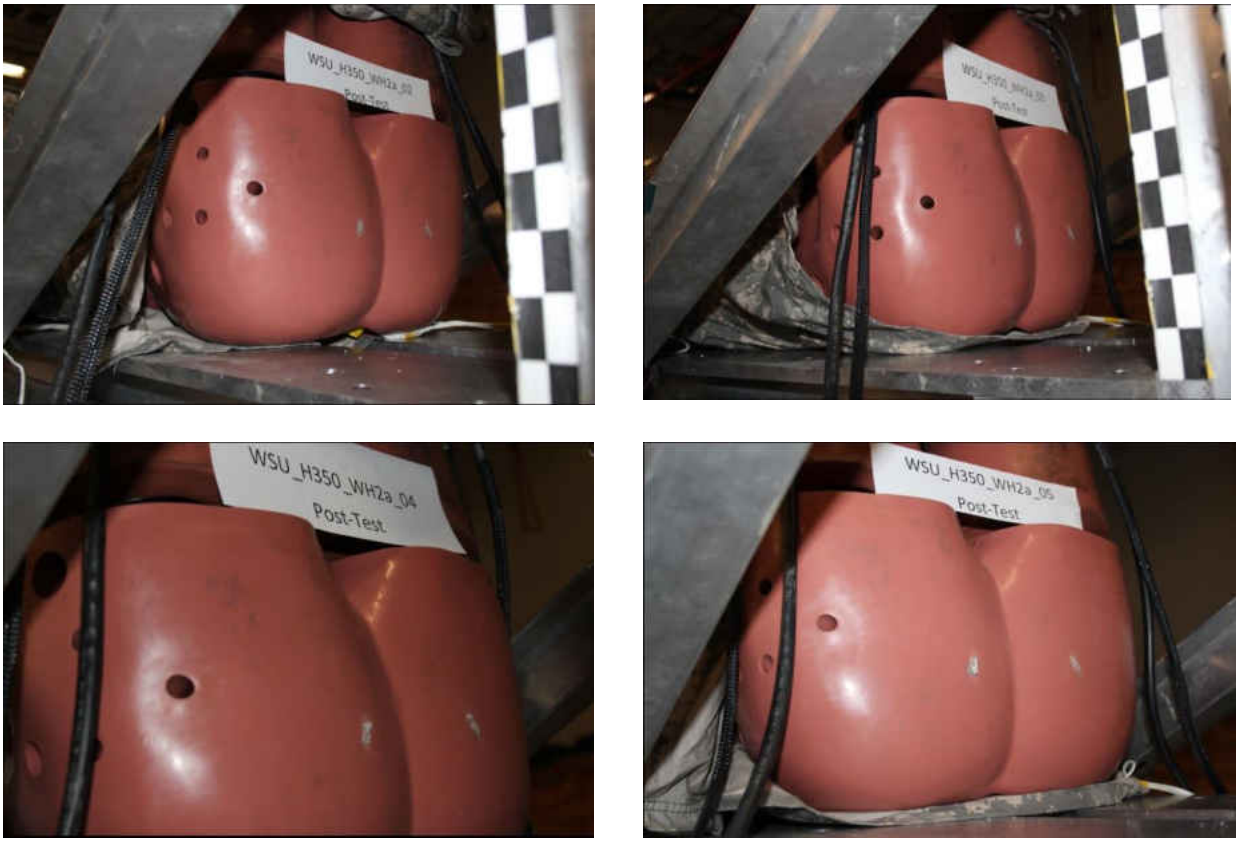

Figure 6-11: Snapshot showing the punctured pelvis flesh impacted with loading condition 2. After the first experiment the rupture worsen with additional tests.

The loading and boundary conditions for the finite element analysis were the same as the physical test. First, the WSU HIII model was validated against the response data obtained from loading condition 1. The seat and floor acceleration profile for the first test of impact condition 1 (Figure 6-3) was used as the input parameters for the validation study. CORA was used to compare how well the updated model correlated to each of the regions of the ATD. The individual regions assessed included acceleration at the (pelvis, chest and head) and force at the (lumbar, tibia and neck). For this comparison, only first test (Test 1) for each condition was assessed. The cross correlation rating for each of the aforementioned responses is shown in Tables 6-5 and 6-6.

The CORA score of the WSU FE model for loading condition 1 ranged from 0.800 to 0.970 and the overall rating was 0.878 using the average of all the responses, where in score with 1 indicates perfect correlation between the selected signals. The shaded region in Figure 6-12 indicates the duration consider for CORA analysis. A reasonable agreement between simulation results and test data indicated that the WSU FE model of the Hybrid III can successfully capture the biomechanical responses in such loading scenarios. Since the lumbar spine force data for loading condition 1 was missing, the simulated lumbar spine force response was not reported. Due to numerical instability for LSTC model the pelvis response up to 12ms was shown in the response plot.

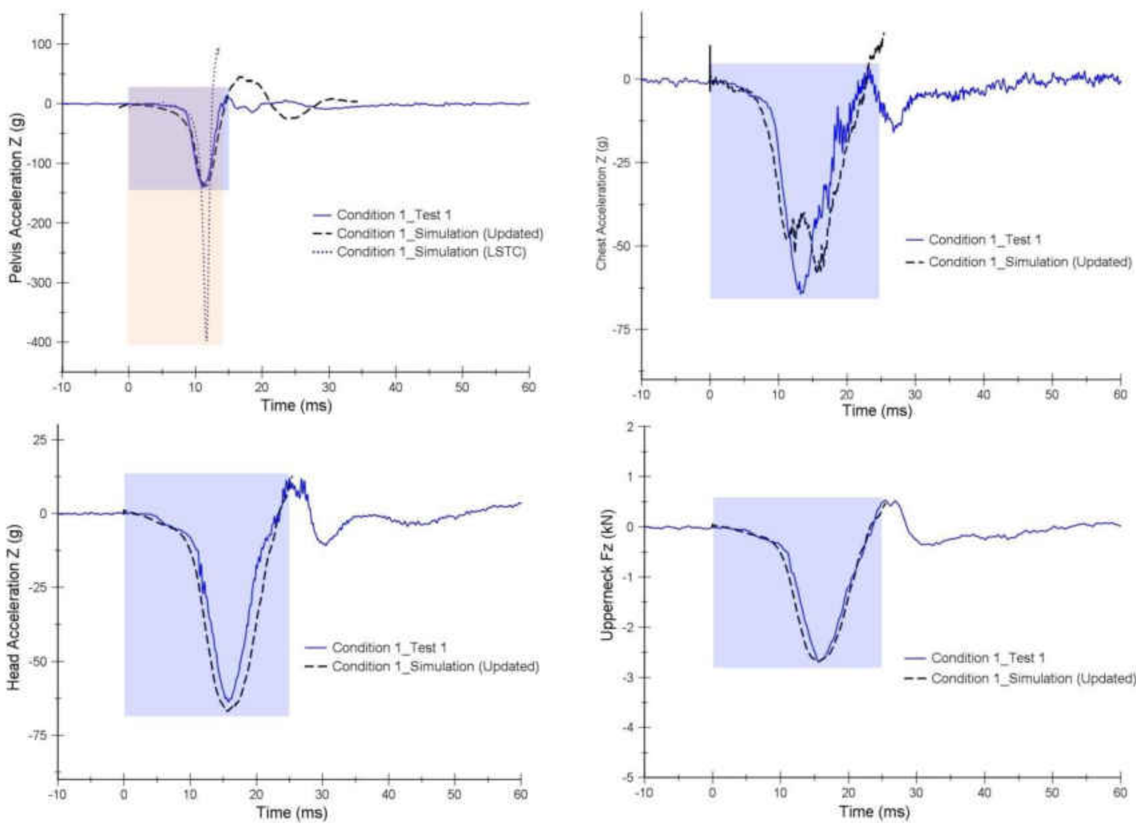

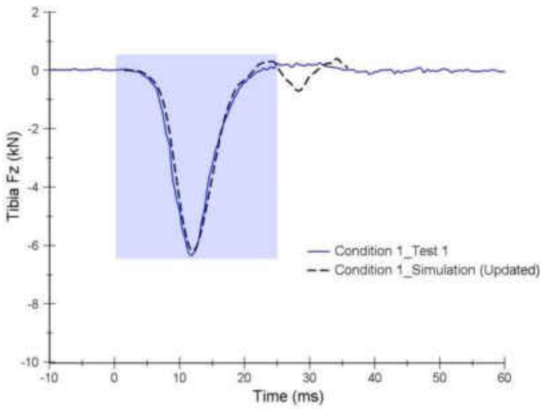

Figure 6-12: Comparisons of the WSU Hybrid III dummy model-predicted and physical test measured impact responses for impact condition 1.

The validated numerical model was also used to simulate condition 2 (a combination of different seat and floor impact conditions). This second simulation study was used to further verify the response of the numerical model to different loading combination at the foot and seat. Figure 6-13 shows a comparison plot of the Hybrid III ATD tests and numerical simulation response curves for the loading condition 2. Like condition 1 numerical study, the CORA score for each FE model response were determined. The shaded region in Figure 6-13 indicates the duration considered for CORA analysis. The score ranged from 0.653 to 0.901 (Tables 6-5 and 6-6) and the overall rating was 0.790 using the average of all the responses. The quantiative analysis between the experiment and WSU FE model showed that the differences in peak response between the two studies ranged from 1.5% to 12.7%. The numerical model response matched the experimental results of the Hybrid III dummy well.

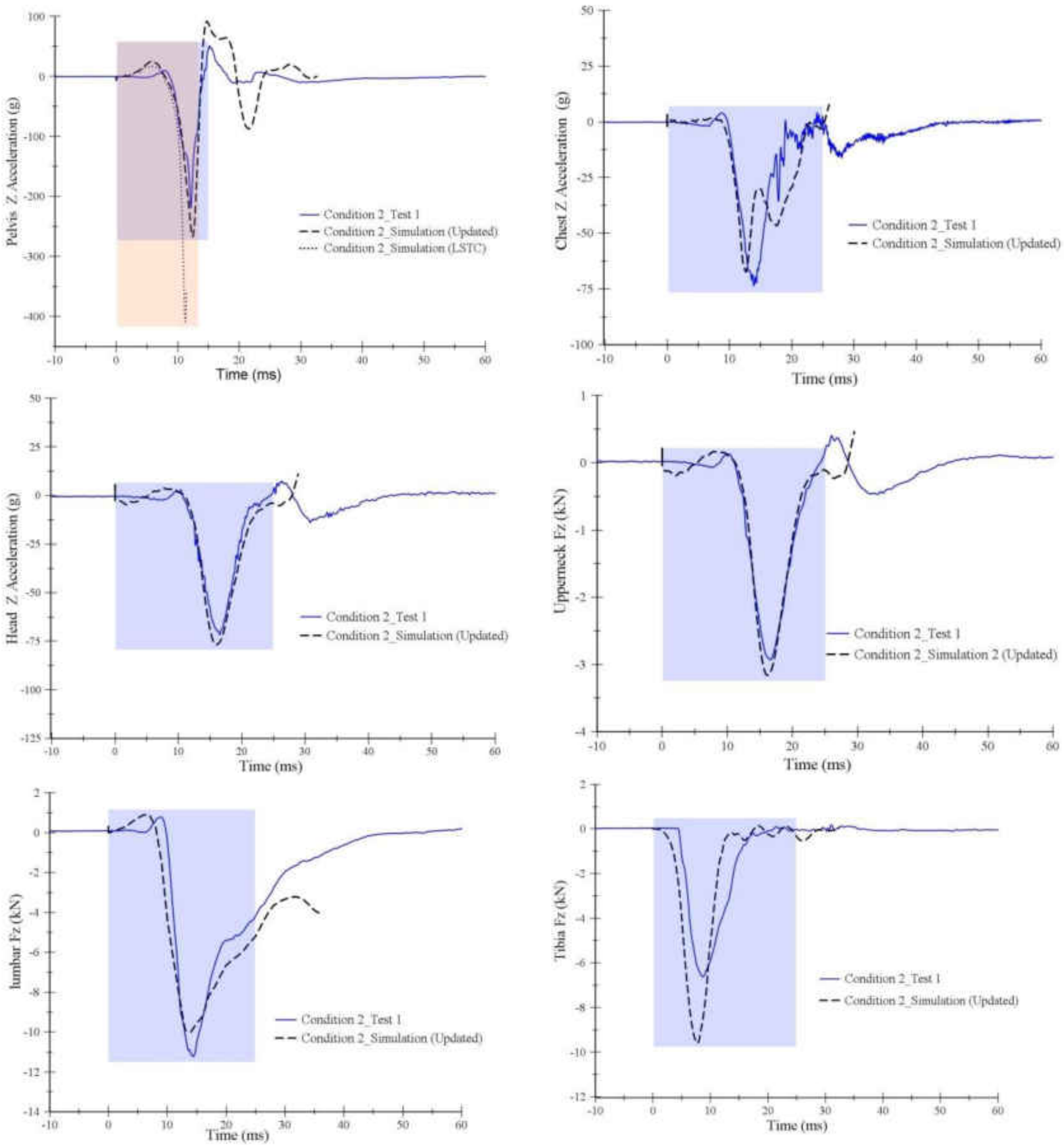

Figure 6-12: Comparison of the WSU Hybrid III dummy model-predicted and physical test measured impact response for impact condition 2.

Table 6-5: Quantitative comparison of numerical model predicted response with the experimental peak pelvis acceleration and corresponding FE model cross correlation rating for WSU model.

Seat Velocity	Test data (g's)	Simulation-LSTC (g's)		Simulation-WSU (g's)	
	Peak Response (Z)	Peak Response (Z)	CORA Score (up to 12ms)	Peak response (Z)	CORA Score (up to 15ms)
5m/s	139.26	396.75	0.147	138.53	0.890
4m/s	218.66	408.54	0.00097	176.41	0.784

Table 6-6: Quantitative comparison of numerical model predicted response with the experimental peak responses for different body regions and corresponding FE model cross correlation rating for WSU model.

Test condition	Response	Test data	Simulation-WSU		
		Peak response	Peak response	Difference (%)	CORA Score (up to 25ms)
Condition 1	Chest Az (g's)	64.05	57.09	5.74	0.841
	Head Az (g's)	63.58	66.49	2.23	0.800
	Upper neck Fz (kN)	2.66	2.70	0.74	0.893
	Lumbar Fz (kN)	N/A	N/A	N/A	N/A
	Tibia Fz (kN)	6.33	6.19	1.11	0.970
Condition 2	Chest Az (g's)	73.59	58.22	11.68	0.653
	Head Az (g's)	71.49	69.74	1.23	0.792
	Upper neck Fz (kN)	2.92	2.82	1.74	0.901
	Lumbar Fz (kN)	11.23	8.97	11.18	0.843
	Tibia Fz (kN)	7.16	9.26	12.78	0.768

Furthermore, along with the numerical response data validation, the kinematics verification is another essential parameter for checking the validity of the simulation study. For a UBB impact test, local kinematics of the foot and pelvis are important to evaluate. Because these components were in direct contact with the loading surfaces and their positions prior to impact and movement upon impact affected the load transmission further into the body. The orientation of the foot and pelvis were matched relative to the foot floor plate and seat prior to impact, respectively (Figures 6-2 B and 6-2 C). Figure 16 shows comparisons of the kinematics between the Hybrid III dummy and those predicted by the WSU model for impact condition 2 at selected time frames. The frame corresponds to Tzero (impact), 10 ms, 30 ms, 60 ms, respectively. The numerical model was able to reproduce similar foot, tibia, pelvis and torso kinematics to those observed in the physical Hybrid III ATD experiments.

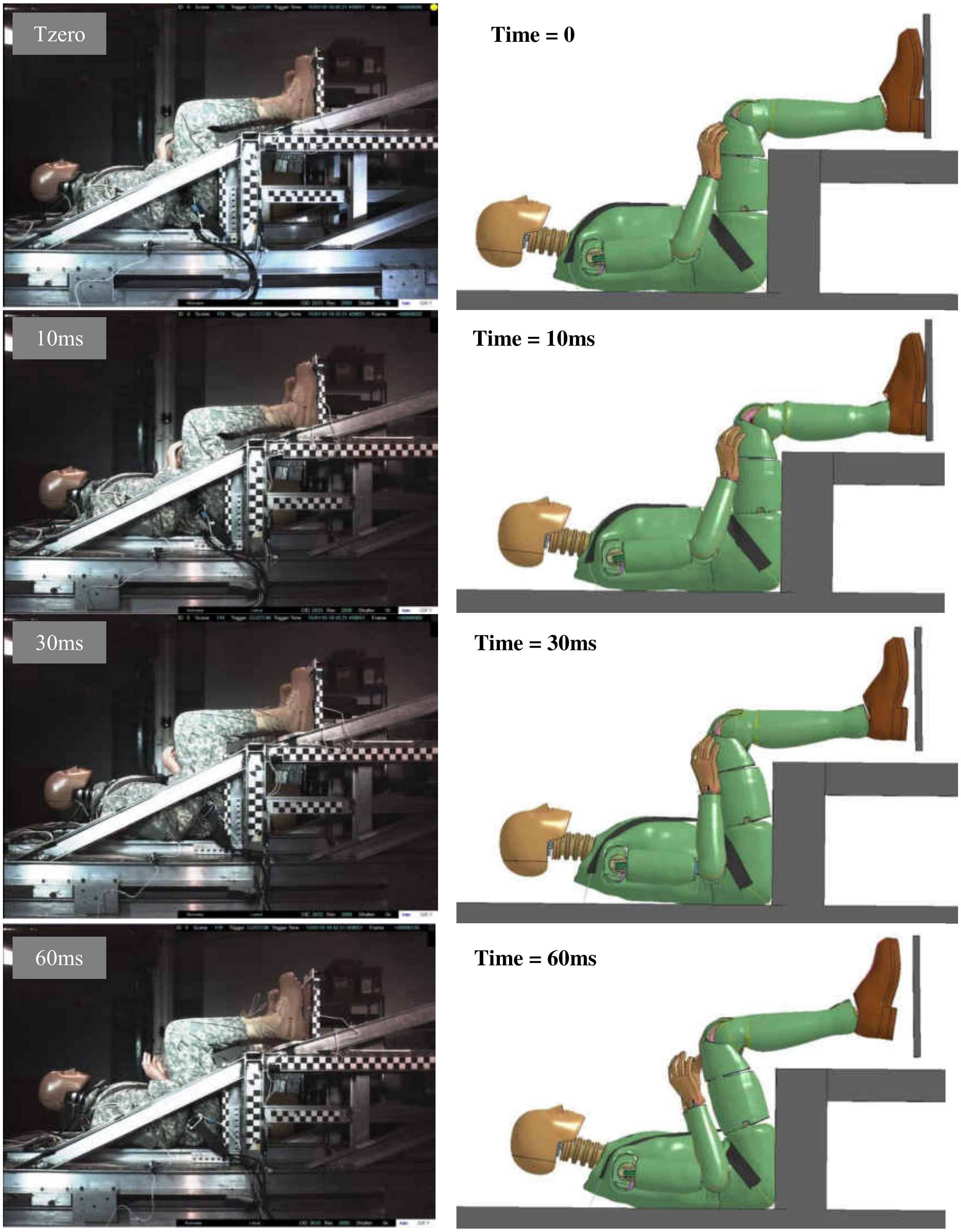

Figure 6-13: Comparison of the Hybrid III kinematics and validated dummy model for impact condition 2. From top to bottom the frame represents Tzero, 10 ms, 30 ms, and 60 ms, respectively.

6.4 Discussion

The post-impact Hybrid III ATD inspection showed a puncture in the pelvis flesh and foam after the first impact for both impact conditions. Examination of the damaged pelvis revealed that the pelvis flesh and foam ruptured at the location where the ATD's metal skeleton, specifically the ischial tuberosities were closest to the seat. Successive testing with the same pelvis worsened the rupture and led to the increase in the peak pelvis acceleration between successive tests as shown in Figure 6-5.

Next, Figure 6-14 shows a cross-sectional view of the Hybrid III pelvis component model. This model mimics the actual physical dummy pelvis .The pelvis component of the Hybrid III ATD consists of the pelvis flesh, pelvis foam, pelvis, spine bracket, and lumbar spine. The vertical distance between the pelvis outer surfaces to the ischial tuberosity of the pelvis metal is noted to be 36 mm, which includes a 6 mm thick pelvis flesh and a 30 mm thick pelvis foam material. During vertical impact, only the pelvis foam and the flesh could undergo deformation.

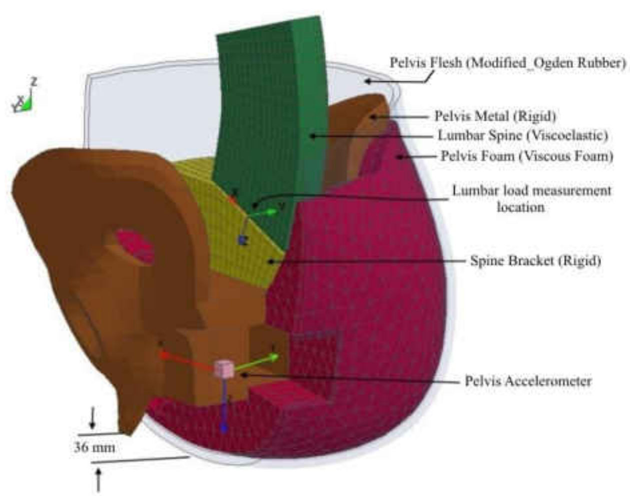

Figure 6-14: An isometric view of the different components of the FE pelvis model with the pelvis flesh and foam removed from the right side.

The finite element pelvis kinematic analyses showed that the 30 mm foam was compressed fully within 11 ms, while the pelvis flesh compressed less.This event corresponds to a blunt puncture of the pelvis foam and pelvis flesh by the sharp rigid ischial tuberocities in the actual Hybrid III tests.

Followed by a blunt puncture of pelvis foam first and then the flesh by the sharp, rigid of the ischial tuberosity. Figure 6-15 shows a comparison of the pelvis component captured at initial time (t = 0 ms) and 11 ms (t = 11ms) post impact, respectively.

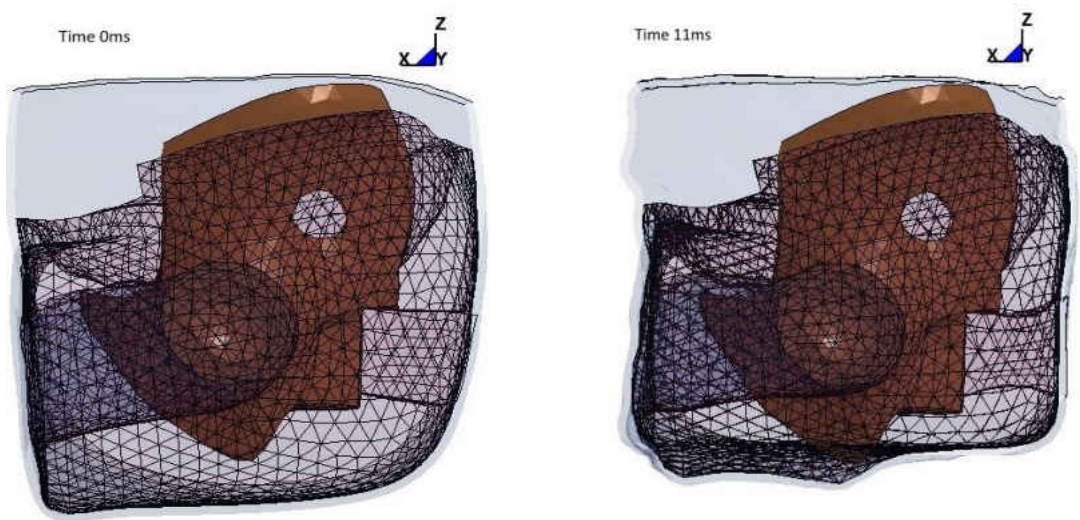

Figure 6-15: Side view of finite element pelvis captured at t = 0 ms and t = 11 ms, respectively.

Furthermore, the principal stress contours in the pelvis flesh and pelvis foam component model were examined. Figure 6-16 shows that the location where the finite element model predicted maximum principal stresses agreed with the experimental testing location where the Hybrid III ATD pelvis was damaged. In addition, finite element analysis showed that the maximum stress location was observed to be approximately the same in both the pelvis flesh and pelvis foam.

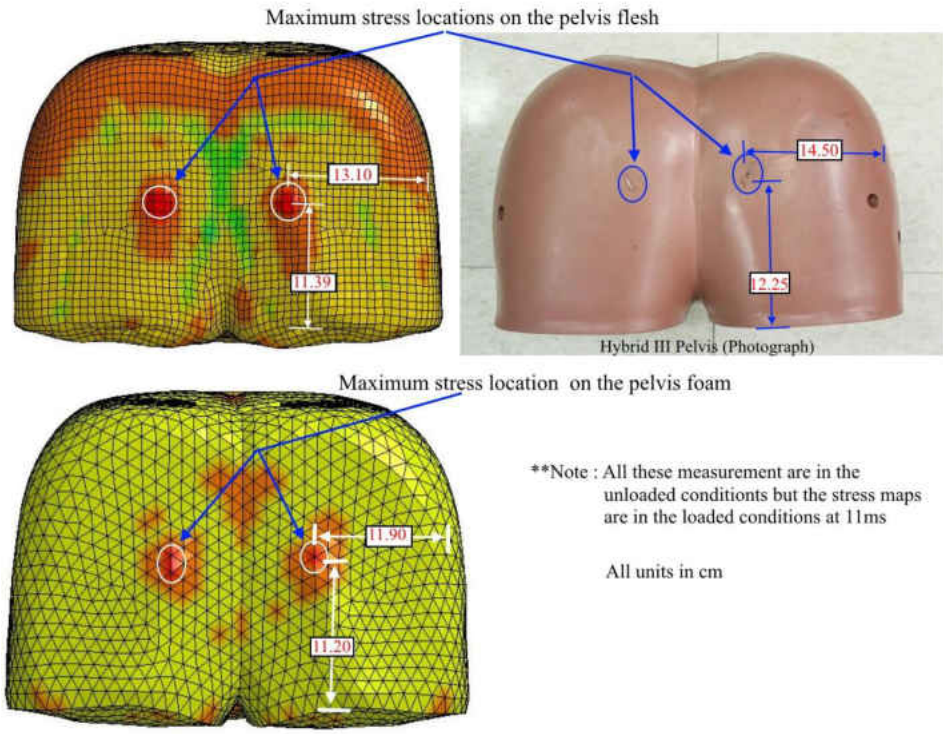

Figure 6-16: The location of pelvis flesh rupture observed in the post test Hybrid III dummy for loading condition 2 coincided with the location where the FE model predicted maximum principal stresses. Below image shows the corresponding pelvis foam stress map.

The principal stress contour in Figure 6-16 indicates that during the loading event the concentrated load produced by the ischial tuberosities on the foam and flesh resulted in the ATD pelvis damage. In addition, the Hybrid III ATD exhibited an increase in the peak pelvis acceleration between consecutive impacts for the same loading condition. A comparison of the ATD responses measured from five consecutive tests for each loading condition is shown in Figure 6-17. The percentage increase in the ATD response between the first and the second impacts under the same loading conditions was determined to be 22.02% for condition 1 and 1.46%, for condition 2. Although the change in peak response in condition 2 testing was lower compared to condition 1, the vertical load at the seat was enough to puncture both the pelvis flesh and foam, thus the pelvis acceleration measured in the second impact was higher compared to the acceleration measured after first impact. It can also be observed from the pelvis response

(Figure 6-17) that the peak acceleration increased further during each subsequent impact. This increase in pelvis response may be due to the deterioration of the pelvis foam rupture with successive impacts. The positive percentage change in Figure 6-17 indicates the rise in the response relative to Test 1 data.

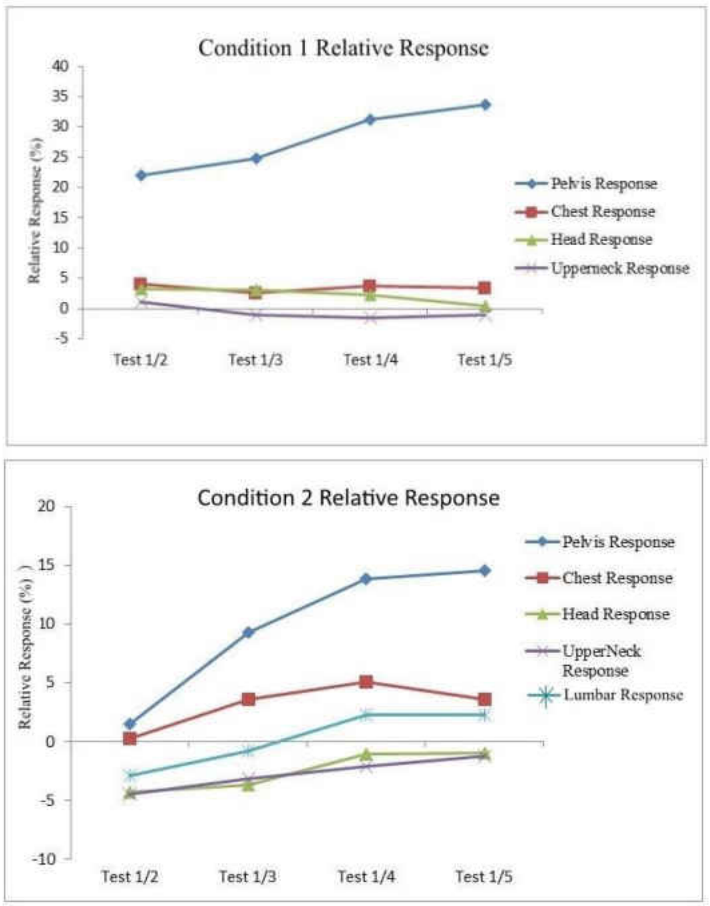

Figure 6-17: Comparisons of the Hybrid III Test 1 relative response with consecutive test data, separated by each loading condition.

For the chest, upper neck and head the test 1 relative response with consecutive impact data ranged within ± 5 % for both loading condition. For the pelvis the test 1 relative response ranged from (20% to 35%) and (3% to 15%) for condition 1 and 2, respectively (Figure 6-17). This observation reveals that, the pelvis response measured at successive tests did not have much influence on the chest, neck and head data. The potential reason could be that the lumbar spine material might attenuate the load transferred through the body.

The quantitative peak response comparison and the overall CORA rating show that the WSU numerical model matched well with the test data (Tables 6-5 and 6-6). Whereas the LSTC model becomes numerical unstable after 12 ms. Within the 12ms the LSTC original model was able to predicate the pelvis peak response alone. The predicated pelvis peak value was relatively higher compare to the test data. For condition 1, the LSTC model predicted a 48% higher response compare to the experiment, while for condition 2, the LSTC model had a 30% higher response than the test data. Therefore finite element analysis showed that the changes in the pelvis flesh material properties improved the CORA score of the finite element ATD pelvis model response from 0.147 to 0.890 and 0.00097 to 0.784 for condition 1 and 2 respectively.

Limitations of the current study include the fact that the loading condition range of the impact tests was very narrow, a lack of pelvis component testing, and a lack of pelvis foam material testing up to failure. The WSU numerical model better matched the biomechanical response as measured by the impact tests for this loading range. However, further numerical study needs to be conducted with this WSU model for different loading conditions. In addition, component level testing for the pelvis will provide a better understanding about the pelvis foam behavior for high-speed conditions. As observed in present ATD testing, after the first impact, the dummy pelvis ruptures and deteriorates further with successive impacts. Therefore, the dummy response is affected only after the first impact. It would be challenging to mimic such behavior of the foam in finite element modelling. Further material testing needed to be performed to evaluate the actual pelvis foam failure stress under concentrated loading. This will provide more accurate material model for the pelvis foam and flesh, respectively.

CHAPTER 7

CONCLUSION

In the current study, two PMHS simulated underbody blast impact tests were conducted under laboratory conditions. Both tests were performed with a rigid seat and no body armor. The loading condition used in this study represents a baseline testing condition for developing biomechanical response corridors. The detailed methodology for these PMHS tests is provided in the thesis. The PMHS test results provided detail biomechanical response data for a defined UBB input condition. The peak tibia Z acceleration results no injuries to lower extremities. Further both the test showed symmetrical lower extremities response. Though the UBB loading condition implemented for this study was initially considered to be a non-injurious, the test condition produced a lumbar fracture in both PMHS tests. The lumbar fractures influenced the thoracic spine and pelvis impact response. The T12 impact response provided information regarding the time of injury. Moreover, the pelvis angle was hypothesized to affect the sacrum and T12 vertebra impact responses. Further experiments would need to be conducted to assess the pelvis and spine behavior for different pelvis angles.

In addition, a series of whole body ATD tests were performed for similar impact conditions to investigate the behavior of the crash dummy for high impact loads. Also, a finite element LSTC model was updated and then validated against the Hybrid III experimental data by modifying the dummy component material models and associated properties. The overall cross correlation rating of 0.878 and 0.790 of the numerical model response for conditions 1 and 2, respectively, reveals that the WSU dummy model was able to simulate actual tests results. In addition, the WSU model revealed high stress concentrations at the same locations where the pelvis flesh and pelvis foam in the actual ATD showed rupture. The stress contour under the ischial tuberosity in the finite element model provides a possible explanation for the factor material and rupture in the actual Hybrid III tests.

APPENDIX A

6.5 ANTHROPOMETRIC MEASUREMENT [cm]

Region	OSU 6908		LMD 14-00355	
Stature	177.0		177.0	
Shoulder Height	155.0		153.0	
Vertex to Symphysis	920.		88.3	
Scye Circumference	R	L	R	L
	43.9	44.0	43.7	41.5
Interscye	32.8		49.1	
Waist Height	101.5		99.2	
Crotch Height	78.0		81.5	
Head Length	19.5		19.5	
Head Breadth	14.5		15.6	
Head Height (Vertex to Mentum)	19.0		22.4	
Bizygomatic Breadth	12.8		12.2	
Menton-Sellion Length	15.7		12.6	
Neck Circumference	37.4		41.1	
Shoulder Breadth	40.8		37.3	
Chest Depth	20.1		25.7	
Chest Circumference	96.9		104.9	
Chest Breadth	33.4		32.4	
Waist Depth	15.5		20.3	

Region	OSU 6908		LMD 14-00355	
Buttock Depth	16.3		18.8	
Buttock Circumference	91.3		97.5	
Tibial Height	R	L	R	L
	46.0	46.5	44.0	45.0
Hip Breadth	30.5		29.2	
Shoulder to Elbow	R	L	R	L
	36.5	36.5	36.8	36.7
Forearm to Hand	R	L	R	L
	48.0	48.2	47.0	47.5
Bicep Circumference	R	L	R	L
	25.0	24.0	27.5	28.2
Elbow Circumference	R	L	R	L
	31.9	30.8	28.1	29.1
Wrist Circumference	R	L	R	L
	17.5	17.5	25.2	25.5
Trochanter to Trochanter Breadth	32.5		34.5	
Upper Thigh Circumference	R	L	R	L
	47.3	48.0	51.2	50.6
Lower Thigh Circumference	R	L	R	L
	34.0	33.8	36.8	35.3
Knee Circumference 90 degree	R	L	R	L
	36.5	36.3	37.5	37.2
Knee Circumference Extended	R	L	R	L
	36.8	36.9	36.5	36.6
Calf Circumference	R	L	R	L
	31.1	30.5	31.8	30.6
Ankle Circumference	R	L	R	L
	22.8	22.8	21.4	21.1
Ankle Height	R	L	R	L
	9.0	9.3	10.5	9.8
Foot Breadth	R	L	R	L
	9.2	9.5	9.2	9.3

6.1 SEATED MEASUREMENT [cm]

Region	OSU 6908		LMD 14-00355		Region	OSU 6908	LMD 14-00355
Vertex to Trochanter	87.5		88.3		Biacrominal Breadth	34.0	33.1
Back length (C7 to Omphalion)	58.0		53.0		Hip Breadth, Sitting	38.5	35.5
Buttock-Knee Length	60.5		58.9		Bideltoid Breadth	45.3	42.8
Knee Height, Sitting	R	L	R	L	Sitting, Height	96.5	97.5
	53.3	53.0	55.3	56.0			

6.2 ROMER ARM DATA

Type	Unit	Nominal	Tolerance	WSU-003	WSU-004
Pelvis Angle	Degree	46	±5	41.18	46.33
Left & Right ASIS alignment along X Axis	MM	0	±20	16.31	2.88
Left & Right ASIS alignment along Z Axis	MM	0	±20	11.73	7.29
C7 to ASIS midpoint	MM	90	±10	91.10	93.00
Left & Right Acromion alignment in X direction	MM	0	±20	3.06	5.30
Left & Right Acromion alignment in Z direction	MM	0	±20	11.75	2.30
Distance between Tragion and C7	MM	85	±10	79.52	83.77
Angle (Right leg to seat back)	Degree	0	±2	1.67	1.32
Angle (Left leg to seat back)	Degree	0	±2	3.00	1.74

APPENDIX B

7.1 PMHS Instrumentation Channel Assignment Matrix

Channel	Location	Sensor Type	Units	Axis
1	Sacrum (S1-S2)	Linear Accelerometer	g	X
2	Sacrum (S1-S2)	Linear Accelerometer	g	Y
3	Sacrum (S1-S2)	Linear Accelerometer	g	Z
4	Sacrum (S1-S2)	Angular Rate Sensor	deg/sec	X
5	Sacrum (S1-S2)	Angular Rate Sensor	deg/sec	Y
6	Sacrum (S1-S2)	Angular Rate Sensor	deg/sec	Z
7	Left Distal Tibia	Linear Accelerometer	g	X
8	Left Distal Tibia	Linear Accelerometer	g	Y
9	Left Distal Tibia	Linear Accelerometer	g	Z
10	Left Distal Tibia	Angular Rate Sensor	deg/sec	X
11	Left Distal Tibia	Angular Rate Sensor	deg/sec	Y
12	Left Distal Tibia	Angular Rate Sensor	deg/sec	Z
13	Left Distal Femur	Linear Accelerometer	g	X
14	Left Distal Femur	Linear Accelerometer	g	Y
15	Left Distal Femur	Linear Accelerometer	g	Z
16	Left Distal Femur	Angular Rate Sensor	deg/sec	X
17	Left Distal Femur	Angular Rate Sensor	deg/sec	Y
18	Left Distal Femur	Angular Rate Sensor	deg/sec	Z
19	Sternum (Manubrium)	Linear Accelerometer	g	X
20	Sternum (Manubrium)	Linear Accelerometer	g	Y
21	Sternum (Manubrium)	Linear Accelerometer	g	Z
22	Sternum (Manubrium)	Angular Rate Sensor	deg/sec	X
23	Sternum (Manubrium)	Angular Rate Sensor	deg/sec	Y
24	Sternum (Manubrium)	Angular Rate Sensor	deg/sec	Z
25	Head	Linear Accelerometer	g	X
26	Head	Linear Accelerometer	g	Y
27	Head	Linear Accelerometer	g	Z
28	Head	Angular Rate Sensor	deg/sec	X
29	Head	Angular Rate Sensor	deg/sec	Y
30	Head	Angular Rate Sensor	deg/sec	Z
31	Right Distal Tibia	Linear Accelerometer	g	X
32	Right Distal Tibia	Linear Accelerometer	g	Y
33	Right Distal Tibia	Linear Accelerometer	g	Z
34	Right Distal Tibia	Angular Rate Sensor	deg/sec	X
35	Right Distal Tibia	Angular Rate Sensor	deg/sec	Y

Channel	Location	Sensor Type	Units	Axis
36	Right Distal Tibia	Angular Rate Sensor	deg/sec	Z
37	Right Distal Femur	Linear Accelerometer	g	X
38	Right Distal Femur	Linear Accelerometer	g	Y
39	Right Distal Femur	Linear Accelerometer	g	Z
40	Right Distal Femur	Angular Rate Sensor	deg/sec	X
41	Right Distal Femur	Angular Rate Sensor	deg/sec	Y
42	Right Distal Femur	Angular Rate Sensor	deg/sec	Z
43	T12 Vertebra	Linear Accelerometer	g	X
44	T12 Vertebra	Linear Accelerometer	g	Y
45	T12 Vertebra	Linear Accelerometer	g	Z
46	T12 Vertebra	Angular Rate Sensor	deg/sec	X
47	T12 Vertebra	Angular Rate Sensor	deg/sec	Y
48	T12 Vertebra	Angular Rate Sensor	deg/sec	Z
49	T8 Vertebra	Linear Accelerometer	g	X
50	T8 Vertebra	Linear Accelerometer	g	Y
51	T8 Vertebra	Linear Accelerometer	g	Z
52	T8 Vertebra	Angular Rate Sensor	deg/sec	X
53	T8 Vertebra	Angular Rate Sensor	deg/sec	Y
54	T8 Vertebra	Angular Rate Sensor	deg/sec	Z
55	T5 Vertebra	Linear Accelerometer	g	X
56	T5 Vertebra	Linear Accelerometer	g	Y
57	T5 Vertebra	Linear Accelerometer	g	Z
58	T5 Vertebra	Angular Rate Sensor	deg/sec	X
59	T5 Vertebra	Angular Rate Sensor	deg/sec	Y
60	T5 Vertebra	Angular Rate Sensor	deg/sec	Z
61	T1 Vertebra	Linear Accelerometer	g	X
62	T1 Vertebra	Linear Accelerometer	g	Y
63	T1 Vertebra	Linear Accelerometer	g	Z
64	T1 Vertebra	Angular Rate Sensor	deg/sec	X
65	T1 Vertebra	Angular Rate Sensor	deg/sec	Y
66	T1 Vertebra	Angular Rate Sensor	deg/sec	Z
67	Right Calcaneus	Linear Accelerometer	g	Z
68	Left Calcaneus	Linear Accelerometer	g	Z
69	Seat 1	Linear Accelerometer	g	Z
70	Seat 2	Linear Accelerometer	g	Z
71	Seat Accelerometer LOFFI	Linear Accelerometer	g	Z
72	Footplate 1	Linear Accelerometer	g	Z
73	Footplate 2	Linear Accelerometer	g	Z

Channel	Location	Sensor Type	Units	Axis
74	Footplate Accelerometer LOFFI	Linear Accelerometer	g	Z
75	Left Foot Heel	Foot Contact Switch	mv	
76	Left Foot Ball	Foot Contact Switch	mv	
77	Right Foot Heel	Foot Contact Switch	mv	
78	Right Foot Ball	Foot Contact Switch	mv	
79	R Shoulder Harness	Load Cell	N	
80	L Shoulder Harness	Load Cell	N	
81	R Lap Harness	Load Cell	N	
82	L Lap Harness	Load Cell	N	
83	Right Proximal Tibia	Strain Gauge	microstrain	
84	Right Distal Tibia	Strain Gauge	microstrain	
85	Right Calcaneus	Strain Gauge	microstrain	
86	Left Proximal Tibia	Strain Gauge	microstrain	
87	Left Distal Tibia	Strain Gauge	microstrain	
88	Left Calcaneus	Strain Gauge	microstrain	
89	Right Ant Sup Iliac Spine	Strain Gauge	microstrain	
90	Right Distal Femur	Strain Gauge	microstrain	
91	Left Ant Sup Iliac Spine	Strain Gauge	microstrain	
92	Left Distal Femur	Strain Gauge	microstrain	
93	Left Pubic Ramus	Strain Gauge	microstrain	
94	Right Pubic Ramus Strain	Strain/Fracture Detection	microstrain	
95	Floor Plate Pot	Potentiometer	V	
96	Foot Plate 7264G	Acceleration	g	Z
97	Seat 7264C	Acceleration	g	Z
98	Fixture Velocity	Fixture Velocity	m/s	Z

Note: All the 98 channels were sampled at the rate of 500,000 samples per second with a 100 kHz anti-aliasing, multiple low pass Butterworth filter.

7.2 DATA PROCESSING MATRIX

Stage	Process	Data
Raw	Download • DAS Output data (.TSV format) • Video data (.AVI format)	• 6DX-transducer (Acceleration & Angular velocity) • Video • Strain • Structure acceleration
Converted	• Engineering unit assigned (mass- kg, length-meter, rotation- degree, strain- µstrain, time- second) • Offset removal • Polarity check • Trimming	• 6DX-transducer (Acceleration & Angular velocity) • Video • Strain • Structure acceleration
Processed	• Filter applied ➢ 1650 Hz- Angular rate data ➢ 3000 Hz- Acceleration & strain data • Video Analysis	• 6DX-transducer (Acceleration & Angular velocity) • Video • Strain • Structure acceleration
Calculated	• Co-ordinate Transformation ➢ 6DX_Acceleration- Rotated and Translated ➢ 6DX_Angular Rate – Translated • Relative Motion - Head/Torso (T1) & Head/Sacrum • Spine Axial Compliance • Foot Motion about the ankle	• 6DX-transducer (Acceleration & Angular velocity data) • Spine compliance – Head/T1, T/T5, T5/T8, T12/S2 • Video (Boot and Tibia target marker displacement data)
Scaled	• Normalization ➢ Mass-Based Technique – 6DX_ Acceleration data ➢ Length-Based Technique – 6DX_ Shoulder and Knee motion data	• 6DX-transducer (Acceleration data) • Video (Shoulder and Knee target marker displacement data)

APPENDIX C

8.1 WSU-003 SCALE FACTOR

Mass –Kg Length - m	Region	Reference Value	WSU Value	λ	Acceleration [λa]	Length [λl]	Time [λt]
Mass-Based Normalization (Acceleration data)	Head	4.39	3.78	1.16	0.95		1.05
	T1 Spine	84.2	67.5	1.25	0.92		1.07
	T5_Spine	84.2	67.5	1.25	0.92		1.07
	T8_Spine	84.2	67.5	1.25	0.92		1.07
	T12_Spine	84.2	67.5	1.25	0.92		1.07
	Sacrum	84.2	67.5	1.25	0.92		1.07
	Femur Left	10.18	5.57	2.00	0.79		1.25
	Femur Right	10.18	5.1	1.83	0.81		1.22
	Tibia Left	4.74	3.07	1.54	0.86		1.15
	Tibia Right	4.74	3.2	1.48	0.87		1.14
	Foot Left	4.74	3.07	1.54	0.86		0.86
	Foot Right	4.74	3.2	1.48	0.87		0.87
Length-Based Normalization (Knee and Shoulder motion data)	Tibia Left	0.424	0.459	0.93		0.93	0.93
	Tibia Right	0.424	0.456	0.92		0.92	0.92
	Stature Height	1.755	1.770	0.99		0.99	0.99

8.2 WSU-004 SCALE FACTOR

Mass –Kg Length - m	Region	Reference Value	WSU Value	λ	Acceleration [λa]	Length [λl]	Time [λt]
Mass-Based Normalization (Acceleration data)	Head	4.39	4.39	1.03	0.99		1.00
	T1 Spine	84.2	77.01	1.09	0.97		1.03
	T5_Spine	84.2	77.01	1.09	0.97		1.03
	T8_Spine	84.2	77.01	1.09	0.97		1.03
	T12_Spine	84.2	77.01	1.09	0.97		1.03
	Sacrum	84.2	77.01	1.09	0.97		1.03
	Femur Left	10.18	6	1.67	0.84		1.18
	Femur Right	10.18	6.06	1.69	0.84		1.18
	Tibia Left	4.74	3.48	1.28	0.92		1.08
	Tibia Right	4.74	3.3	1.35	0.90		1.10
	Foot Left	4.74	3.48	1.28	0.92		1.08
	Foot Right	4.74	3.3	1.35	0.90		1.10
Length-Based Normalization (Knee and Shoulder motion data)	Tibia Left	0.424	0.456	0.93		0.93	0.93
	Tibia Right	0.424	0.459	0.92		0.92	0.92
	Stature Height	1.755	1.772	0.99		0.99	0.99

APPENDIX D

9.1 ORIENTATION OF MOUNT RELATIVE TO THE BONE

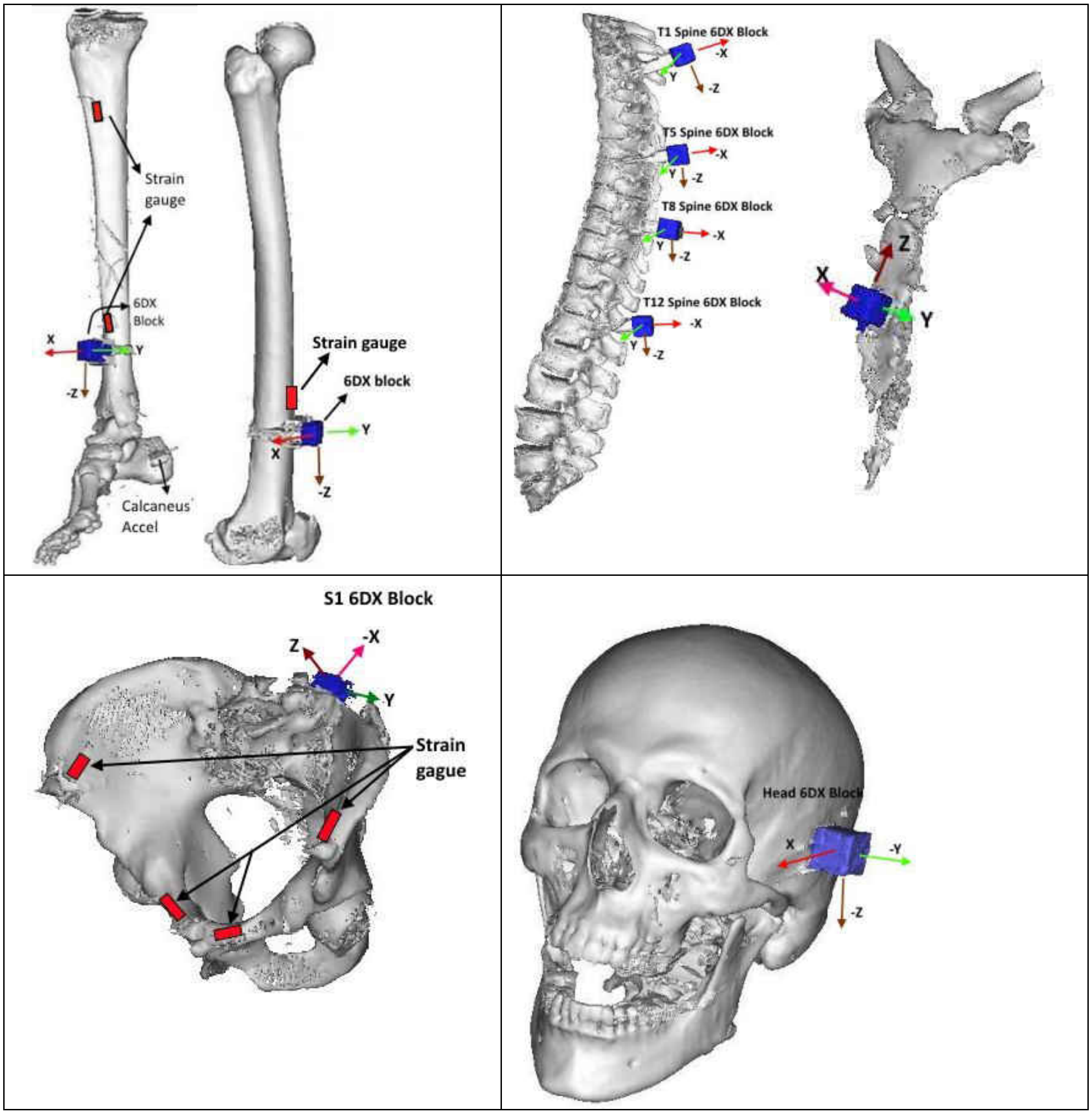

Figure: 6DX block orientation with respect to the anatomical region for OSU6908 Specimen.

APPENDIX E

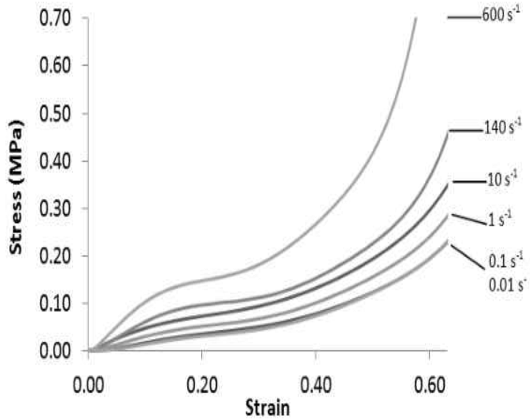

Figure: Stress-strain curve for the heel pad foam (Zhu et al., 2015).

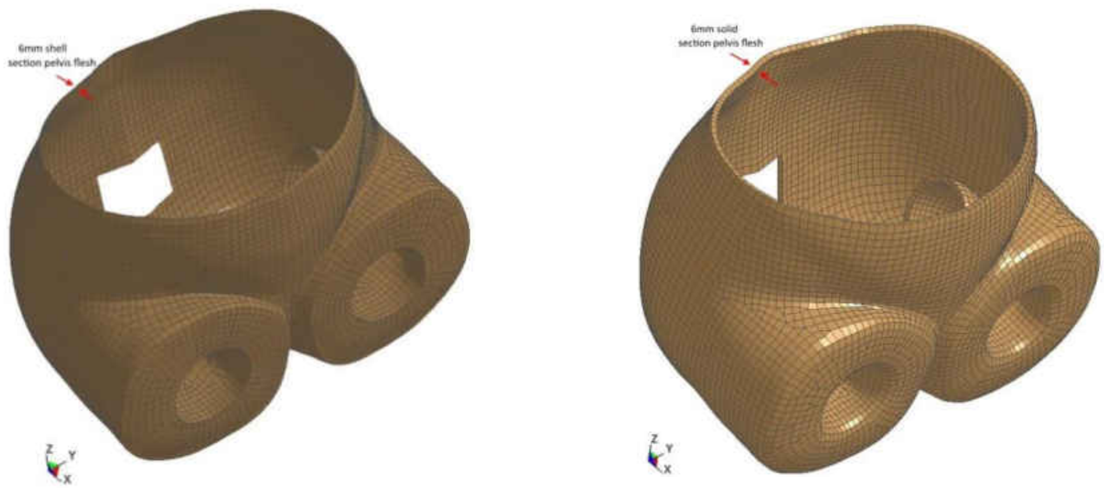

Figure: Pictorial comparisons between the LSTC and modified pelvis models (same thickness).

ABSTRACT

Methodology for Performing Whole Body PMHS Underbody Blast Impact Testing, and the Corresponding Response of the Hybrid III Dummy and the Finite Element Dummy Model to similar Loading Conditions

By

Karthik Somasundaram

Oct 2016

Advisor: Dr. John Cavanaugh

Major: Biomedical Engineering

Degree: Master of Science

In recent wars, the use of improvised explosive devices and landmines has dramatically increased as a tactical measure to counter armored vehicles. These weapons not only deform and damage the vehicle structure but also produce serious vertical deceleration injuries to mounted occupants. The reported injury patterns largely differ from those in an automotive crash and are often more severe than those in other vertical loading scenarios such as pilot seat ejection, helicopter crash, parachute landing and fall from height. High kinetic energy predominately along the principal vertical (Z-axis) over a short duration makes the underbody blast (UBB) loading conditions unique compared to other vertical and blunt impacts. With the lack of biomechanical response corridors (BRCs), the non-biofidelic nature of the automotive dummies to Z-axis loading and the lack of a finite element dummy model designed for vertical loading make it difficult to evaluate occupant response and develop mitigation strategies for UBB impact conditions.

An introduction to the development of the BRCs this study provides a detailed methodology to perform whole body cadaver testing under a laboratory setup. Two whole body PMHS UBB

impact tests were conducted using a sled system. An overview of pre-impact parameters such as bone mineral density, instrumentation technique, and vertical impulse generation is presented. Post-test CT scans, response data, and possible injury mechanisms were investigated.

In addition, to PMHS testing, the responses of the Hybrid III dummy to short-duration large magnitude vertical acceleration in a laboratory setup were analyzed. Two unique test conditions were investigated using a horizontal sled system to simulate the UBB loading conditions. The biomechanical response in terms of the pelvis acceleration, chest acceleration, lumbar spine force, head accelerations and neck forces were measured during the tests.

Subsequently, a series of finite element analyses (FEA) were performed to simulate the physical tests. The material parameters of various components as well as the mesh size were updated based on the high strain rate loading conditions obtained from Zhu et.al (2015) study. The correlation between the Hybrid III test and numerical model was evaluated using the CORA version 3.6.1. The Cora score for WSU FE model was determined to be 0.878 and 0.790 for loading conditions 1 and 2, respectively, in which 1.0 indicated a perfect correlation between the experiment and simulation response. The original LSTC model simulated under the current loading condition became numerically unstable after 12 ms. With repetitive vertical impacts, the Hybrid III dummy pelvis showed a significant increase in the peak acceleration accompanied by rupture of the pelvis foam and flesh. The revised WSU Hybrid III model indicated high stress concentrations at the same location where the pelvis foam and flesh in the actual ATD showed rupture. The stress contour under the ischial tuberosities in the finite element model provides a possible explanation for the material failure in the actual Hybrid III tests.

REFERENCES

Alvarez, J., 2011. Epidemiology of blast injuries in current operations. A Survey of Blast Injury across the Full Landscape of Military Science.

Bailey, A.M., Christopher, J.J., Brozoski, F., Salzar, R.S., 2015. Post mortem human surrogate injury response of the pelvis and lower extremities to simulated underbody blast. Annals of biomedical engineering 43, 1907-1917.

Bailey, A.M., Christopher, J.J., Henderson, K., Brozoski, F., Salzar, R.S., 2013. Comparison of Hybrid-III and PMHS Response to Simulated Underbody Blast Loading Conditions.

Bailey, J.R., Stinner, D.J., Blackbourne, L.H., Hsu, J.R., Mazurek, M.T., 2011. Combat-related pelvis fractures in nonsurvivors. Journal of Trauma-Injury, Infection, and Critical Care 71, S58-S61.

Bir, C., Barbir, A., Dosquet, F., Wilhelm, M., van der Horst, M., Wolfe, G., 2008. Validation of lower limb surrogates as injury assessment tools in floor impacts due to anti-vehicular land mines. Military medicine 173, 1180-1184.

Bird, R., 2001. Protection of vehicles against landmines. Journal of Battlefield Technology 4, 14-17.

Bogduk, N., 2005. Clinical anatomy of the lumbar spine and sacrum. Elsevier Health Sciences.

Bosch, K., Harris, K., Melotik, J., Clark, D., Scherer, R., 2014. Blast Mitigation Seat Analysis: Drop Tower Data Review. DTIC Document.

Chung, K.J., Suh, S.W., Desai, S., Song, H.R., 2008. Ideal entry point for the thoracic pedicle screw during the free hand technique. International orthopaedics 32, 657-662.

Cody, J.P., Kang, D.G., Lehman Jr, R.A., 2012. Combat-related lumbopelvic dissociation treated with percutaneous sacroiliac screw placement. The Spine Journal 12, 858-859.

Comstock, S., Pannell, D., Talbot, M., Compton, L., Withers, N., Tien, H.C., 2011. Spinal injuries after improvised explosive device incidents: implications for Tactical Combat Casualty Care. The Journal of trauma 71, S413-417.

Cummings, S.R., Bates, D., Black, D.M., 2002. Clinical use of bone densitometry: scientific review. JAMA : the journal of the American Medical Association 288, 1889-1897.

DePalma, R.G., Burris, D.G., Champion, H.R., Hodgson, M.J., 2005. Blast injuries. New England Journal of Medicine 352, 1335-1342.

Eppinger, R.H., Marcus, J.H., Morgan, R.M., 1984. Development of dummy and injury index for NHTSA's thoracic side impact protection research program. SAE Technical Paper.

Gehre, C., Gades, H., Wernicke, P., 2009. Objective rating of signals using test and simulation responses. In 21st International Technical Conference on the Enhanced Safety of Vehicles Conference (ESV), Stuttgart, Germany, June.

Gray, H., Goss, C.M., Alvarado, D.M., 1973. Anatomy of the human body. Lea & Febiger Philadelphia.

Harrison, D.D., Harrison, S.O., Croft, A.C., Harrison, D.E., Troyanovich, S.J., 1999. Sitting biomechanics part I: review of the literature. Journal of manipulative and physiological therapeutics 22, 594-609.

Heymsfield, S.B., FULENWIDER, T., Nordlinger, B., Barlow, R., Sones, P., Kutner, M., 1979. Accurate measurement of liver, kidney, and spleen volume and mass by computerized axial tomography. Annals of internal medicine 90, 185-187.

Huelke, D.F., 1986. Anatomy of the lower extremity-an overview. SAE Technical Paper.

J Ruppa, M.R., 2013. PMHS Positioning Procedure, Bio-Instrumentation. University of Michigan Transportation Research Institue, pp. 1-23.

Jackson, K.E., Fasanella, E.L., Boitnott, R., McEntire, J., Lewis, A., 2004. Occupant Responses in a Full-Scale Crash Test of the Sikorsky ACAP Helicopter. Journal of the American Helicopter Society 49, 127-139.

Kang, D.G., Cody, J.P., Lehman Jr, R.A., 2012a. Combat-related lumbopelvic dissociation treated with L4 to ilium posterior fusion. The Spine Journal 12, 860-861.

Kang, D.G., Dworak, T.C., Lehman Jr, R.A., 2012b. Combat-related L5 burst fracture treated with L4–S1 posterior spinal fusion. The Spine Journal 12, 862-863.

Kang, D.G., Lehman Jr, R.A., Carragee, E.J., 2012c. Wartime spine injuries: understanding the improvised explosive device and biophysics of blast trauma. The Spine Journal 12, 849-857.

Kargus, R., Li, T., Frydman, A., Nesta, J., 2008. Methodology for establishing the mine/IED resistance capacity of vehicle seats for crew protection. DTIC Document.

Keegan, J., Omaha, N., 1953. To posture and seating.

Ken-An Lou, D.B., Kiran Irde, Zachary Blackburn, 2013. Simulation of Various LSTC Dummy Models to Correlate Drop Test Results, 13th International LS-DYNA User Conference. Livermore Software Technology Corporation, Detroit, p. 12.

Kerrigan, J.R., Crandall, J.R., Deng, B., 2008. A comparative analysis of the pedestrian injury risk predicted by mechanical impactors and post mortem human surrogates. Stapp car crash journal 52, 527.

Kim, Y.J., Lenke, L.G., Bridwell, K.H., Cho, Y.S., Riew, K.D., 2004. Free hand pedicle screw placement in the thoracic spine: is it safe? Spine 29, 333-342.

Kraft, R.H., Lynch, M.L., Vogel III, E.W., 2012. Computational Failure Modeling of Lower Extremities. DTIC Document.

Manseau, J., Keown, M., 2005. Evaluation of the complex lower leg (CLL) for its use in anti-vehicular mine testing applications. In International IRCOBI Conference on the Biomechanics of Impacts, Prague, Czech Republic.

Martin, P.G., Hall, G.W., Crandall, J.R., Pilkey, W.D., 1998. Measuring the acceleration of a rigid body. Shock and Vibration 5, 211-224.

Mattei, T.A., Meneses, M.S., Milano, J.B., Ramina, R., 2009. Free-hand" technique for thoracolumbar pedicle screw instrumentation: critical appraisal of current" state-of-art. Neurology India 57, 715.

McConville, J.T., Clauser, C.E., Churchill, T.D., Cuzzi, J., Kaleps, I., 1980. Anthropometric relationships of body and body segment moments of inertia. DTIC Document.

Mckay, B.J., 2010. Development of lower extremity injury criteria and biomechanical surrogate to evaluate military vehicle occupant injury during an explosive blast event.

Melton, L.J., 3rd, Thamer, M., Ray, N.F., Chan, J.K., Chesnut, C.H., 3rd, Einhorn, T.A., Johnston, C.C., Raisz, L.G., Silverman, S.L., Siris, E.S., 1997. Fractures attributable to osteoporosis: report from the National Osteoporosis Foundation. Journal of bone and mineral research : the official journal of the American Society for Bone and Mineral Research 12, 16-23.

Miller, K., Morelli, L., 1993. Ejection Tower Evaluation of the Rate-Dependant Foam Cushions for the NACES Seat. DTIC Document.

Moore, K.L., Dalley, A.F., Agur, A.M., 2006. Clinically oriented anatomy. Lippincott Williams & Wilkins.

Netter, F.H., 2010. Atlas of human anatomy. Elsevier Health Sciences.

NIH, 2012. Bone Mass Measurement, Natioanl Institute of Arthritis and Musculoskeletal and Skin Diseases. National Institues of Health, Bethesda, MD, USA.

Nordin, M., Frankel, V.H., 2001. Basic biomechanics of the musculoskeletal system. Lippincott Williams & Wilkins.

Owens, B.D., Kragh Jr, J.F., Macaitis, J., Svoboda, S.J., Wenke, J.C., 2007. Characterization of extremity wounds in operation Iraqi freedom and operation enduring freedom. Journal of orthopaedic trauma 21, 254-257.

Paquette, S., Gordon, C., Bradtmiller, B., 2009. Anthropometric survey (ANSUR) II pilot study: methods and summary statistics. DTIC Document.

Pintar, F., Bolte, J., Salzr, R., Ott, K., Kleinberger, M., Merkle, A., 2013. Instrumentation Installation Techniques.

Possley, D.R., Blair, J.A., Freedman, B.A., Schoenfeld, A.J., Lehman, R.A., Hsu, J.R., 2012. The effect of vehicle protection on spine injuries in military conflict. The Spine Journal 12, 843-848.

Radonic, V., Giunio, L., Biocic, M., Tripkovic, A., Luksic, B., Primorac, D., 2004. Injuries from antitank mines in Southern Croatia. Military medicine 168, 320-324.

Ragel, B.T., Allred, C.D., Brevard, S., Davis, R.T., Frank, E.H., 2009. Fractures of the thoracolumbar spine sustained by soldiers in vehicles attacked by improvised explosive devices. Spine 34, 2400-2405.

Ramasamy, A., Hill, A.-M., Hepper, A., Bull, A., Clasper, J., 2009. Blast mines: physics, injury mechanisms and vehicle protection. Journal of the Royal Army Medical Corps 155, 258-264.

Ramasamy, A., Masouros, S.D., Newell, N., Hill, A.M., Proud, W.G., Brown, K.A., Bull, A.M., Clasper, J.C., 2011. In-vehicle extremity injuries from improvised explosive devices: current and future foci. Philosophical Transactions of the Royal Society B: Biological Sciences 366, 160-170.

Rudd, R., Kerrigan, J., Crandall, J., Arregui, C., 2006. Kinematic Analysis of Head/Neck Motion in Pedestrian-Vehicle Collisions Using 6-Degree-of-Freedom Instrumentation Cubes. SAE Technical Paper.

Sanner, M.F., 1999. Python: a programming language for software integration and development. J Mol Graph Model 17, 57-61.

Schardin, H., 1950. The physical principles of the effects of a detonation. German Aviation Medicine, World War II 2, 1207-1224.

Schneck, M.W.C., 1998. The Origins of Military Mines: Part I. Engineer 58, 50.

Schoberth, H., Hegemann, G., 1962. Sitzhaltung, Sitzschaden, Sitzmöbel. Springer.

Schoenfeld, A.J., Goodman, G.P., Belmont Jr, P.J., 2012a. Characterization of combat-related spinal injuries sustained by a US Army Brigade Combat Team during Operation Iraqi Freedom. The Spine Journal 12, 771-776.

Schoenfeld, A.J., Lehman Jr, R.A., Hsu, J.R., 2012b. Evaluation and management of combat-related spinal injuries: a review based on recent experiences. The Spine Journal 12, 817-823.

Schueler, F., Mattern, R., Zeidler, F., Scheunert, D., 1995. Injuries of the lower legs-foot, ankle joint, tibia; mechanisms, tolerance limits, injury-criteria evaluation of a recent biomechanic experiment series (impact tests with a pneumatic-biomechanic impactor). In Proceedings Of The 1995 International Ircobi Conference On The Biomechanics Of Impact, September 13-15, 1995, Brunnen, Switzerland.

Segal, D.R., Segal, M.W., 2004. America's military population. Population Reference Bureau Washington, DC.

Spink, R.J., 2014. A Simple Method for Processing Measurements of Vehicle Response to Underbody Blast During Live Fire Test and Evaluation. DTIC Document.

Stuhmiller, J.H., Phillips, Y., Richmond, D., 1991. The physics and mechanisms of primary blast injury. Conventional warfare: ballistic, blast, and burn injuries. Washington, DC: Office of the Surgeon General of the US Army 241270.

Taber, K.H., Warden, D.L., Hurley, R.A., 2006. Blast-related traumatic brain injury: what is known? The Journal of neuropsychiatry and clinical neurosciences.

Tile, M., Helfet, D., Kellam, J., 2003. Fractures of the pelvis and acetabulum. Lippincott Williams & Wilkins.

TR-HFM-090, N.A.T.O., 2007. Test methodology for protection of vehicle occupants against anti-vehicular landmine effects, Final Report of the Human Factors and Medicine Task Group 090 (HFM-090).

Van der Horst, M., Simms, C., van Maasdam, R., Leerdam, P., 2005. Occupant lower leg injury assessment in landmine detonations under a vehicle. In IUTAM Symposium on Impact Biomechanics: From Fundamental Insights to Applications.

van der Horst, M.J., Leerdam, P.-J.C., 2002. Experimental and numerical analysis of occupant safety in blast mine loading under vehicles. In Proceedings of the International Research Council on the Biomechanics of Injury conference.

Van Rossum, G., 2007 Python Programming Language. In USENIX Annual Technical Conference.

Wang, J., Bird, R., Swinton, B., Krstic, A., 2001. Protection of lower limbs against floor impact in army vehicles experiencing landmine explosion. J Battlefield Tech 4, 11-15.

Warden, D., 2006. Military TBI during the Iraq and Afghanistan wars. The Journal of head trauma rehabilitation 21, 398-402.

Warden, D.L., French, L.M., Shupenko, L., Fargus, J., Riedy, G., Erickson, M.E., Jaffee, M.S., Moore, D.F., 2009. Case report of a soldier with primary blast brain injury. NeuroImage 47, T152-T153.

Wilson, C., 2006. Improvised explosive devices (IEDs) in Iraq and Afghanistan: effects and countermeasures.

Xydakis, M.S., Fravell, M.D., Nasser, K.E., Casler, J.D., 2005. Analysis of battlefield head and neck injuries in Iraq and Afghanistan. Otolaryngology-Head and Neck Surgery 133, 497-504.

Yoganandan, N., Moore, J., Arun, M.W., Pintar, F.A., 2014. Dynamic responses of intact post mortem human surrogates from inferior-to-superior loading at the pelvis. Stapp car crash journal 58, 123.

Yoganandan, N., Stemper, B.D., Baisden, J.L., Pintar, F.A., Paskoff, G.R., Shender, B.S., 2013. Effects of acceleration level on lumbar spine injuries in military populations. The Spine Journal.

Zeiller, S., Lee, J., Lim, M., Vaccaro, A., 2005. Posterior thoracic segmental pedicle screw instrumentation: evolving methods of safe and effective placement. Neurology India 53, 458.

Zhu, F., Dong, L., Jin, X., Jiang, B., Kalra, A., Shen, M., Yang, K.H., 2015. Testing and Modeling the Responses of Hybrid III Crash-Dummy Lower Extremity under High-speed Vertical Loading. Stapp car crash journal 59, 521-536.

Zouris, J.M., Walker, G.J., Dye, J., Galarneau, M., 2006. Wounding patterns for US Marines and sailors during Operation Iraqi Freedom, major combat phase. Military medicine 171, 246-252.

AUTOBIOGRAPHY

NAME	POSITION TITLE
Karthik Somasundaram	Graduate Research Assistant, Department of Biomedical Engineering, Wayne State University.

EDUCATION			
INSTITUTION	DEGREE	YEAR	MAJOR
Wayne State University, Detroit, U.S.A	Ph.D.	2015-Present	Biomedical Engineering
Wayne State University, Detroit, U.S.A	M.Sc.	2012- 2015	Biomedical Engineering
Anna University, Chennai, India	B.E.	2007-2011	Biomedical Engineering

Position and Employment

2013- Present — Graduate Research Assistant, Sport and Ballistic Laboratory, Wayne State University, Detroit, MI.

2012-2013 — Student Assistance, Spine Laboratory of Dr. Cavanaugh, Wayne State University, Detroit, MI.

2011-2012 — Program Analysist, Cognizant Technology Solution, Chennai, India.

Research Interests

Blast impact, Injury Biomechanics, Finite Element Analysis

Publications

1. Kalra, Anil, **Karthik Somasundaram**, Ming Shen, Vishal Gupta, Clifford C. Chou, and Feng Zhu. Effect of Boot Compliance in Numerical Model of Hybrid III in Vertical Loading. No. 2016-01-1525. SAE Technical Paper, 2016.
2. **Somasundaram Karthik**, Anil Kalra, Sherman Don, Begeman Paul, Cavanaugh John. M., Yang King H. An Experimental and Numerical Study of the Hybrid III Dummy's Response to Simulated Underbody Blast Impacts, under review.
3. **Somasundaram Karthik**. Methodology for Performing Whole Body PMHS Underbody Blast Impact Testing, and the Corresponding Response of the Hybrid III Dummy and the Finite Element Dummy Model under similar Loading Condition, Master Thesis, expected date of defense July, 2016, Wayne State University, Detroit, USA.